Formulation development for oxygen sensitive EPR spin probes

Dissertation

zur Erlangung des
Doktorgrades der Naturwissenschaften (Dr. rer. nat.)

der

Naturwissenschaftlichen Fakultät I — Biowissenschaften —

der Martin-Luther-Universität
Halle-Wittenberg

vorgelegt von

Frau Apothekerin Juliane Neidel geb. Frank
geboren am 23.01.1987 in Berlin

Gutachter:

1.   Prof. Dr. Karsten Mäder
2.   Prof. Dr. Peter Imming
3.   Prof. Bernard Gallez, PhD

Datum der öffentlichen Verteidigung: 30.05.2018

Dedicated to my family

Contents

Glossary

ΔB_{PP}	Peak-to-peak line width
AO	Atomic orbital
BSA	Bovine serum albumin
Cl-TAM-*t*BE	Tris(4-*tert*-butoxy-carbonyl-2,3,5,6-tetrachlorophenyl)methyl radical
Cl-TAM-EE	Tris(4-ethoxycarbonyl-2,3,5,6-tetrachlorophenyl)methyl radical
DLS	Dynamic light scattering
DMF	*N,N*-Dimethylformamide
DMSO	Dimethyl sulfoxide
DSC	Differential scanning calorimetry
dTAM	Tris[8-carboxy-2,2,6,6-(^{2}H3-tetramethyl)benzo[1,2-*d*:4,5-*d'*]bis([1,3]dithiole)-4-yl]methyl radical
dTAM-dEE	Tris[8-(^{2}H3-ethoxy)-2,2,6,6-(^{2}H3-tetramethyl)benzo[1,2-*d*:4,5-*d'*]bis(-[1,3]dithiole)-4-yl]methyl radical
dTAM-EE	Tris[8-ethoxy-2,2,6,6-(^{2}H3-tetramethyl)benzo[1,2-*d*:4,5-*d'*]bis([1,3]dithiole)-4-yl]methyl radical
EDTA	Ethylenediaminetetraacetic acid
EPR	Electron paramagnetic resonance
GM	Geometrical mean
GPC	Gel permeation chromatography
GSD	Geometrical standard deviation
HEPES	4-(2-Hydroxyethyl)-1-piperazine-ethanesulfonic acid
hfs	Hyperfine splitting
HIF	Hypoxia-inducible factor
HRMS	High resolution mass spectrometry
IPM	Isopropyl myristate
IR	Infrared
LDH	Lactate dehydrogenase
LiNc	Lithium-naphthalocyanine
LiNc-BuO	Lithium-5,9,14,18,23,27,32,36-octa-*n*-butoxy-2,3-naphthalocyanine
LiPc	Lithium-phthalocyanine

m/z	Mass-to-charge ratio
MCs	Microcapsules
MCT	Medium-chain triglycerides
MO	Molecular orbital
MPs	Microparticles
MR	Magnetic resonance
n.m.	Not measured
NADH	β-Nicotinamide adenine dinucleotide, reduced disodium salt hydrate
Nc-BuO	5,9,14,18,23,27,32,36-Octa-n-butoxy-2,3-naphthalocyanine
NCs	Nanocapsules
NMR	Nuclear magnetic resonance
NPs	Nanoparticles
pCO_2	Partial pressure of carbon dioxide
pO_2	Partial pressure of oxygen
PB	Phosphate buffer
PBS	Phosphate-buffered saline
PDMS	Polydimethylsiloxane
Ph.Eur.	European Pharmacopoeia
PLA	Poly(L-lactic acid)
ppm	Parts per million
PTFE	Polytetrafluoroethylene
PVA	Poly(vinyl alcohol)
PVAc	Poly(vinyl acetate)
PVP	Polyvinylpyrrolidone
ROS	Reactive oxygen species
rpm	Revolutions per minute
RPMI	Roswell Park Memorial Institute
sO_2	Oxygen saturation
SD	Standard deviation
SDS	Sodium dodecyl sulfate
SNR	Signal-to-noise ratio
T_1	Spin-lattice relaxation time
T_2	Spin-spin relaxation time
T_g	Glass transition temperature
TAM	Tris[8-carboxy-2,2,6,6-tetramethylbenzo[1,2-d:4,5-d']bis([1,3]dithiole)--4-yl]methyl radical
TAM-tBE	Tris[8-$tert$-butoxycarbonyl-2,2,6,6-tetramethylbenzo[1,2-d:4,5-d']bis-

	([1,3]dithiole)-4-yl]methyl radical
TAM-EE	Tris[8-ethoxycarbonyl-2,2,6,6-tetramethylbenzo[1,2-d:4,5-d']bis([1,3]-dithiole)-4-yl]methyl radical
TB	4-Hydroxy-2,2,6,6-tetramethylpiperidin-1-oxyl (TEMPOL) benzoate
Tetrachloro-TAM	Tetrachlorotriarylmethyl
Tetrathia-TAM	Tetrathiatriarylmethyl
THF	Tetrahydrofuran
TMS	Tetramethylsilane
TRIS	Tris(hydroxymethyl)aminomethane
Trityl	Triarylmethyl
UV/Vis/NIR	Ultraviolet–visible–near infrared
XRD	X-ray diffraction

1 Introduction

Around 2.3 billion years ago, when cyanobacteria had successfully established themselves, one of the most essential requirements of aerobic life forms started to accumulate in earth's atmosphere: Oxygen [1, 2]. In a process well known as oxygenic photosynthesis, these microbes were capable of using energy from sun light to produce organic compounds from water and carbon dioxide; Oxygen molecules were released as a by-product [3, 4]. Today, earth's unique atmosphere with the presence of approximately 21 % (v/v) breathable oxygen molecules [5] allows not only for the existence of basic microorganisms but also of sophisticated species, for instance, humans.

Oxygen is important for cellular respiration in aerobic organisms. More precisely, during oxidative phosphorylation at the inner mitochondrial membrane, oxygen is the most electronegative and, therefore, final acceptor of electrons in the electron transport chain [6]. Consequently, it combines with hydrogen ions to form water, while adenosine diphosphate (ADP) is phosphorylated to adenosine triphosphate (ATP), which serves as an ubiquitous and immediate energy source for metabolic processes [6]. Thus, along with the six basic nutrients, *i.e.*, water, carbohydrates, lipids, proteins, vitamins, and minerals [7], oxygen is essential for aerobic species to obtain usable energy. Interestingly, oxygen is not always regarded as a nutrient, although it needs a constant supply. The human body can only survive minutes without oxygen, but days or weeks without water or food, respectively.

1.1 Oxygen and its role in the human body

Oxygen is absorbed by the blood stream in the lungs, where it combines rapidly with (deoxy-) hemoglobin in red blood cells to form oxyhemoglobin. Only limited amounts of oxygen can be dissolved in blood. Thus, oxyhemoglobin carries the main fraction of oxygen to the tissue capillaries, where it is released and deoxyhemoglobin is formed back. Oxygen then diffuses through capillary walls, interstitial fluid, and cell membranes into the cells. Besides oxidative phosphorylation, oxygen is involved in a large number of biosynthetic pathways and metabolic reactions [8]. Therefore, oxygen homeostasis is essential.

The pathophysiological state with subnormal tissue oxygenation is called hypoxia [9] and arises where more oxygen is consumed than supplied. Upon exposure to severe hypoxia,

the energy demand of a cell cannot be met. Consequently, protein and nucleic acid synthesis are inhibited and later ionic pumps cease their work, leading to cell depolarization, and, finally, cell death [10]. To avoid this, hypoxia is immediately noticed by several chemoreceptors, which subsequently regulate the cardiovascular and respiratory system to optimize oxygen delivery [10]. Additionally, all nucleated cells respond acutely by activation of pre-existing proteins and adapt to chronic hypoxia through the regulation of gene transcription, mediated by hypoxia-inducible factor 1 (HIF-1) [10, 11]. Typical adaption mechanisms to hypoxia include the reversion from aerobic respiration to anaerobic glycolysis, enhancement of oxygen carrying capacity of the blood, as well as angiogenesis and vascular remodeling to improve oxygen delivery [10, 11]. Hypoxia is involved in many pathological conditions, *e.g.*, cardiovascular diseases (including chronic ischaemic heart disease, acute myocardial infarction, and stroke) as well as cancer, which were among the most frequent causes of death in 2015 in Germany [12].

In oncology, the oxygenation of a tumor dramatically affects its curability, and hypoxia is linked with a bad prognosis [9]. Independent of their size, stage, or grade, most solid tumors are more or less hypoxic [9]. In tumors, this is mostly caused by an increased metabolic demand due to the rapid growth as well as reduced perfusion and nutrient delivery because of abnormal vascularization and disturbed microcirculation [13, 14]. Hypoxic tumor regions are often heterogeneously distributed within the tumor [15]. While normal cells respond to hypoxia with cell cycle arrest, apoptosis, or necrosis, tumor cells develop escape mechanisms [14]. Thereby, a selection pressure is induced, forcing cells to adapt to hypoxia. As a consequence, the malignancy of a tumor is increased in terms of its proliferation, cell dedifferentiation, cell survival, angiogenesis, energy metabolism, and metastatic potential. Moreover, the effectiveness of surgery as well as the response to ionizing radiation and chemotherapeutic agents has been found to be reduced in hypoxic tumors [13–16]. Hypoxia in the tumor tissue becomes critical at a partial pressure of oxygen (pO_2) below $10\,\text{mmHg}$, albeit it is difficult to set a generally applicable limit [15]. Nevertheless, tumor tissue oxygenation is an important prognostic indicator. The quantification of oxygen levels not only during tumor growth but also during treatment can be helpful to understand mechanisms underlying hypoxia and to individualize tumor therapy: The tissue oxygenation can be manipulated, or timing and dose of cancer treatments can be optimized to improve their efficiency [17].

Brain and heart are two organs with high energy demand, making them particularly vulnerable to hypoxia [18, 19]. If the oxygen supply is insufficient, *e.g.*, during respiratory hypoxia or declined blood flow (ischemia), brain/cardiac functions are impaired or, even worse, viability cannot be sustained [18, 19]. Hypoxia or ischemia can induce vascular remodeling, resulting in a blood flow through collateral vessels to avoid (further) damage

[11]. However, also subsequent reperfusion can cause injury, which is minimized by a treatment called ischemic preconditioning when possible [11]. Knowledge of tissue oxygenation is crucial to gain a better understanding of ischemia and reperfusion processes, and to study mechanisms of adaption to chronic hypoxia. Moreover, the effect of physiological parameters, the breathing gas, anesthetics, or drugs on brain/myocardial oxygenation can be investigated in order to enhance the effectiveness of treatments [20].

Oximetry is further employed to monitor the status of peripheral vascular disease, which is characterized by poor circulation in the legs [21]. Assessing the disease progression can help to choose and adjust the therapy. Poor circulation, often observed in diabetics, is further connected with an impaired wound healing [22]. Oxygen is involved in several levels of the wound healing process: Epithelialization, bacterial defence, angiogenesis, and collagen synthesis [23]. Thus, the knowledge of oxygen delivery and metabolism in different zones of chronic wounds can help to select efficient therapeutics.

Oxygen is not only vital, but also noxious. The generation of reactive oxygen species (ROS), which happens unintendedly as by-products of metabolism or intendedly by enzymes, can cause cellular damage [8]. ROS include the superoxide radical anion ($O_2^{-\bullet}$), hydrogen peroxide (H_2O_2), the hydroxyl radical ($OH^{\bullet}$), and singlet oxygen ($^1O_2$) [19]. Paradoxically, ROS can be useful for certain physiological processes [8]. But when the antioxidant defense mechanisms of aerobic species fail to counteract their toxicity, oxidative stress is caused [8]. Thus, ROS are involved in the pathogenesis of various diseases like atherosclerosis, ischemia-reperfusion injury, cancer, inflammation, and aging. To study oxidative processes, the gradient between the extracellular and intracellular oxygen levels are of interest [24]. Furthermore, oxygen often plays a regulatory role, affecting metabolic processes and cell signaling [24].

1.2 Oximetric techniques

To investigate the role of oxygen in certain (patho-) physiological processes, a reliable quantification of oxygen levels in tissues is crucial. Albeit various oximetric techniques have been developed, *in vivo* oximetry is challenging. Selected important methods, comprehensively reviewed in [9, 14, 17, 25–27], are shortly summarized in table 1.1. Of course, all techniques have certain strengths, which are not mentioned due to limited space. Considerable shortcomings mostly include the incapability of providing accurate or absolute values of tissue pO_2, long scanning times, the missing opportunity of conducting repeated measurements at a defined site, as well as concerns regarding toxicity and invasiveness [28]. This work deals with the less common method electron paramagnetic resonance (EPR), also referred to as electron spin resonance (ESR) spectroscopy.

Table 1.1: Selected oximetric techniques, their principle and major limitations.

Method	Principle	Major disadvantages
Electrochemistry (polarographic Clark electrode, *e.g.*, Eppendorf histograph) – the *gold standard*	Current from Ag/AgCl anode (oxidation of silver to silver ions) to platinum cathode (reduction of oxygen and reaction to water) proportional to pO_2	Invasiveness, consumption of oxygen, poor signal-to-noise ratio (SNR) at low oxygen contents
Fluorescence quenching (fibre-optic probes, *e.g.*, OxyLite and PreSens)	Life time of fluorescence, emitted by fluorescence dyes upon excitation, inversely related to pO_2	Invasiveness, no repetition at the same site
Phosphorescence quenching	Life time of phosphorescence, emitted by an injected phosphorescence dye, inversely proportional to oxygen concentration in the vasculature	No tissue pO_2, contrast agent needed, limited measurement depth
Near infrared spectroscopy (NIRS)/pulse oximetry	Different light absorption by (de-) and oxyhemoglobin in the NIR region enables determination of hemoglobin content and its oxygen saturation	No tissue pO_2
Immunohistochemistry		
Bioreductive 2-nitroimidazoles (*e.g.*, pimonidazole)	Selective reduction, activation, and reaction with thiol groups to form stable adducts in viable hypoxic cells	Qualitative information only (impact of, *i.a.*, perfusion, amount of reductases), biopsy needed
Endogenous markers	Overexpression in hypoxic cells	No tissue pO_2, biopsy needed
Positron emission tomography (PET)	Selective accumulation of radiolabeled (*e.g.*, ^{18}F) biomarkers in hypoxic cells	Radioactive contrast agents needed, short half-life times
Photoacoustic methods		
General	Measurement of optical absorption by detection of emitted acoustic field	
Tomography	Different light absorption by (de-) and oxyhemoglobin	No tissue pO_2
Life time imaging	Life time of excited state of a dye inversely related to pO_2	Contrast agents needed

Table 1.1: Selected oximetric techniques, their principle and major limitations.

Method	Principle	Major disadvantages
(Nuclear) magnetic resonance [(N)MR] techniques		
BOLD (blood oxygen level-dependent)	Detection of changes in hemoglobin saturation as paramagnetic deoxyhemoglobin reduces the spin-spin relaxation time (T_2) of water protons in blood and surrounding tissues	No tissue pO_2, impact of, *i.a.*, perfusion
TOLD (tissue oxygen level-dependent)	Decrease in spin-lattice relaxation time (T_1) of water protons in tissues related to the pO_2	Rather qualitative, influence of other parameters
^{19}F or ^{1}H relaxometry	Decrease in T_1 of perfluorocarbons/hexamethyldisiloxane related to the pO_2	Contrast agents needed
Dynamic contrast-enhanced (DCE) MR imaging	Paramagnetic contrast agent enhances contrast (decreases T_1), thus, providing information on perfusion and vasculature	Contrast agents needed, no tissue pO_2
Overhauser-enhanced MR imaging (OMRI)	Hyperpolarization of water protons by saturation of the electron spin of a paramagnetic contrast agent via dynamic nuclear polarization (DNP) provides information about vasculature and pO_2	Contrast agents needed

1.3 EPR oximetry

EPR is a powerful oximetric technique. The impact of oxygen on EPR spectra of organic radicals has first been observed in 1960 independently by Deguchi and Hausser [29]. Among the first applications of EPR oximetry were the measurement of oxygen consumption rates in cell suspensions by Backer *et al.* in 1977, and the investigation of oxygen transport within and across lipid bilayer membranes [30]. Later, Hyde and Subczynski explored the quantifiability of the oxygen induced effect on the spectrum of spin probes, and reported the first *in vivo* EPR oximetry measurement in 1986 [26, 30]. Thenceforward, the preclinical application of EPR oximetry in all fields mentioned before has been very successful, making it an indispensable tool for basic research in small animals [17, 20, 30–32]. The strengths of EPR oximetry are summarized from [20, 24, 33] below.

- EPR measurements are noninvasive, avoiding injury and trauma, which could perturb the oxygen measurements. Albeit, just like contrast agents for other techniques, so-called spin probes (stable paramagnetic molecules/radicals) have to be inserted or injected into tissues prior to the measurements. The placement is minimally invasive since very thin needles can be used. The usage of spin probes is necessary since biological samples normally do not contain measurable amounts of stable radicals.

- The latter fact makes EPR measurements fairly specific. There is no considerable interference from other sources.

- Once the spin probes are introduced, the measurements can be conducted continuously or repeatedly, sometimes up to several months or years.

- Upon calibration, absolute oxygen contents can be determined.

- The sensitivity is high: Very small differences in the oxygen content can be resolved.

- EPR oximetry measurements are highly accurate, which has been verified by comparison with other methods.

- The oxygen response is very fast and changes can be observed in real time.

- No oxygen is consumed during the measurements.

- Depending on the choice of spin probe, *in vivo* EPR measurements can be conducted in the vascular system or directly in the tissue of interest.

- Spin probes have been developed, which are metabolically inert, nontoxic, and stable, and can be placed in a specific site of a tissue, thus, allowing for localized measurements in long term studies.

- Using soluble radicals, spatial oxygen distribution maps can be obtained (imaging).

Unfortunately, the measurement depth is fairly limited, impeding a widespread usage in large animals and humans and, hence, transfer to clinical studies. Albeit, the major technological challenges have been met: A clinic EPR spectrometer with a pole separation of $0.5\,\mathrm{m}$ has been developed, which enables comfortable positioning of a patient [33]. Alternatively, miniature probeheads for transcutaneous measurements have been developed [34]. Thus, first clinical studies in humans subjects have been performed successfully at the Dartmouth-Hitchcock Medical Center (Lebanon, USA) [35, 36]. Especially peripheral tumors, peripheral vascular disease, and wound healing, where a high penetration depth is not mandatory, are significant clinical applications for EPR oximetry [21]. However, it is unlikely that EPR spectroscopy will ever become as widely utilized as, *e.g.*, NMR techniques [21]. But depending on the research issue, it is a valuable method to be applied alternatively or complementary to other oximetric methods.

1.3.1 Basics of EPR spectroscopy

The physical theory behind EPR spectroscopy and the mathematical description of the resonance phenomena are sophisticated and can be explained more comprehensively by quantum mechanics. Fortunately, useful information encoded in the EPR spectrum can easily be extracted. The basics of EPR described here shall give the reader an application-oriented understanding to help interpreting EPR spectra. A deeper insight into the underlying concepts is presented in other references, *e.g.*, [37–40].

Zeeman observed the energetic splitting of spectral lines in a magnetic field (Zeeman effect) in 1896, for which he was awarded the Nobel prize later [41]. In 1922, Stern and Gerlach spatially separated silver atoms into two components when an atomic beam was subjected to an inhomogeneous magnetic field [42]. The observation was in contrast to the classical expectation and explained by quantum theory [43]. Three years later, Goudsmit and Uhlenbeck first proposed that electrons possess an intrinsic angular momentum [44, 45]. This spin angular momentum was assigned two possible values, spin up and spin down [44, 45]. Eventually, in 1944, Zavoiskii performed the first EPR experiment [46].

EPR measures the absorption of electromagnetic radiation by paramagnetic species located in an external magnetic field. Due to its charge, spin and orbital rotation, each unpaired electron exhibits a magnetic momentum. In an external magnetic field, the electron has two allowed orientations (parallel or anti-parallel), resulting in two energy levels as depicted in figure 1.1. The ratio of electrons in the lower energy level to electrons in the higher one N_l/N_h is given by Boltzmann's distribution.

$$N_l/N_h = e^{\Delta E/(k \cdot T)} \tag{1.1}$$

Here, k is Boltzmann's constant ($k = 1.38 \times 10^{-23}$ J/K), and T is the absolute temperature. Electrons from the lower energy level can be excited to the higher state until
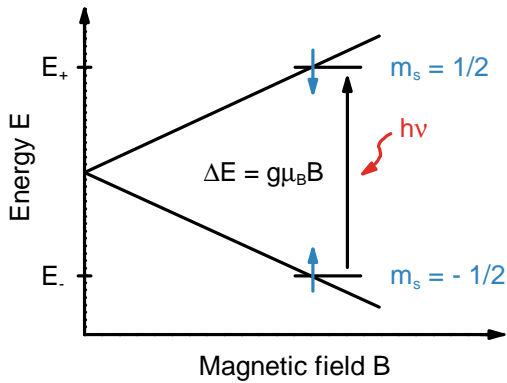
Figure 1.1: Zeeman splitting: The energy levels $E_\pm$ split depending on the magnetic spin quantum number $m_s = \pm 1/2$ and the magnetic field strength B into $E_\pm = \pm 1/2 \cdot g \cdot \mu_B \cdot B$, where g is the g-factor ($g \approx 2.0023$ for a free electron) and μ_B is the Bohr magneton ($\mu_B = 9.274 \times 10^{-24}$ J/T).

both levels are equally populated (saturation). They absorb electromagnetic radiation of frequency ν if the energy per photon $E = h \cdot \nu$, where Planck's constant is $h = 6.626 \times 10^{-34}$ J s, matches the energy difference between the two Zeemann levels, *i.e.*, the resonance condition

$$E = h \cdot \nu = g \cdot \mu_B \cdot B_0 \tag{1.2}$$

is fulfilled. Usually the frequency is fixed and the magnetic field strength is changed (swept) to B_0, where the resonance condition is satisfied. This is called continuous wave (cw) EPR. Frequencies typically employed for oximetry are $9\,\mathrm{GHz}$ to $10\,\mathrm{GHz}$ (X-band) and $1\,\mathrm{GHz}$ to $1.5\,\mathrm{GHz}$ (L-band), which lies in the microwave range. For $g = 2$, the corresponding resonance fields are approximately $322\,\mathrm{mT}$ to $357\,\mathrm{mT}$ and $36\,\mathrm{mT}$ to $54\,\mathrm{mT}$, respectively. Sensitivity increases with magnetic field strength and frequency of the electromagnetic radiation. Due to the stronger splitting, more electrons are in the lower state and can be excited, according to Boltzmann's distribution. To further improve sensitivity, the magnetic field is not only steadily swept, but superimposed by an oscillating magnetic field of low amplitude ($1\,\mathrm{\mu T}$ to $1\,\mathrm{mT}$) at a frequency of usually $100\,\mathrm{kHz}$ (magnetic field modulation). While noise appears randomly, a phase-sensitive detector only detects the signal which is oscillating at the same frequency, resulting in a typical first derivative spectrum (figure 1.2).
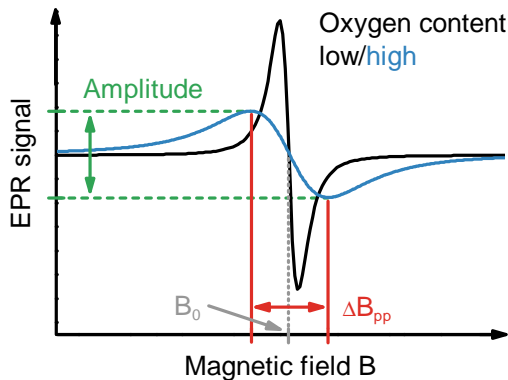
Figure 1.2: Typical EPR spectra: First derivative of the absorption is plotted against the magnetic field strength B. The lines are characterized by their amplitude, B_0 field, and the line width, *e.g.*, peak-to-peak line width (ΔB_{PP}). Double integration provides the intensity of the signal.

Besides the external magnetic field, other electron or nuclear spins in spatial proximity might influence the electron, affecting the g-factor. Moreover, coupling with surrounding nuclei results in further splitting of the energy states, the hyperfine splitting (hfs). n equivalent nuclei, each with a nuclear spin I will give $2 \cdot n \cdot I + 1$ equally spaced energy lines: deuterium (^{2}H) and ^{14}N ($I = 1$) cause splitting into three lines, and protons (^{1}H), ^{13}C, and ^{15}N ($I = 1/2$) into two lines. These interactions might be anisotropic. Their strength is reflected in the distance between the lines (coupling constant).

To return to thermal equilibrium, there are two main relaxation mechanisms. Spin-lattice (longitudinal) relaxation involves energy transfer to the surrounding environment by thermal lattice vibrations and is described by the relaxation time T_1. Spin-spin (transverse) relaxation is caused by energy transfer between electron spins, characterized by T_2. In general, $T_1 \geq T_2$.

1.3.2 Basic principle of EPR oximetry

EPR oximetry utilizes the fact that oxygen, albeit having an even number of electrons, shows paramagnetic behavior. This is explained by molecular orbital (MO) theory (figure 1.3). Hence, the triplet state (total electron spin $s = 1$) is the ground state of oxygen [5].
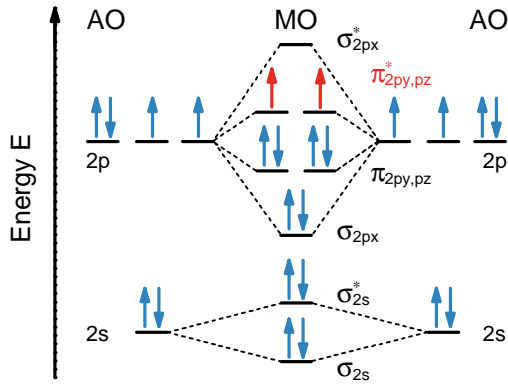
Figure 1.3: MO energy diagram for oxygen. Atomic orbitals (AOs) combine to bonding (σ, π) MOs of lower energy and antibonding (σ^*, π^*) MOs of higher energy, delocalizing the electrons over the entire molecule. As required by Hund's rules, orbitals of equal energy are filled singly with electrons of parallel spin before they are paired. Thus, two unpaired electrons exist in the π^*_{2py} and π^*_{2pz} MOs [47].

Due to its extremely fast relaxation, oxygen cannot be observed directly by EPR spectroscopy (at least not in solution at ambient conditions) [17], but its presence can be detected. Upon collision with oxygen sensitive spin probes, the EPR line widths of these radicals are broadened (figure 1.2), mainly via Heisenberg spin exchange [48]: When two paramagnetic species approach each other, such that the orbitals of the two spins overlap, the electrons are indistinguishable and can be exchanged [49]. This is also observed at high concentrations of the spin probe itself, which has been observed by Hutchison *et al.* in 1952, or at elevated temperatures as reported by Pake and Tuttle in 1959, and explained by a spin exchange model [20]. Spin exchange accelerates relaxation, *i.e.*, it can cause both T_1 and T_2 to shorten [20]. As dictated by Heisenberg's uncertainty principle,

$$\Delta E \cdot \Delta t \geq \frac{h}{4 \cdot \pi}, \tag{1.3}$$

the energy of a quantum state cannot precisely be determined [50]. The energy uncertainty ΔE of an excited state with a life time Δt results in a broadened absorption line, whereby mainly the effect of T_2 is observed [51]. In addition, electron-electron or electron-nuclear dipole-dipole interactions might affect the relaxation times [48]: The presence of

randomly oriented dipoles in the environment of the spin probe can shift its absorption line and broaden it [37]. In solution, where oxygen and spin probe molecules are freely diffusing, the line broadening is directly proportional to the experimental observable bimolecular collision rate ω_{obs}, which is defined by the modified Smoluchowski equation

$$\omega_{\mathrm{obs}} = 4 \cdot \pi \cdot R \cdot p \cdot (D_{\mathrm{O}_2} + D_{\mathrm{SP}}) \cdot c_{\mathrm{O}_2}, \tag{1.4}$$

where R is the interaction distance, p is the probability that an observable event is recorded when a collision takes place, D_{O_2} and D_{SP} are the diffusion coefficients of oxygen and the spin probe, respectively, and c_{O_2} is the concentration of dissolved oxygen [52]. It was assumed that $p \approx 1$ and $R = 0.45\,\mathrm{nm}$ for nitroxide radicals and oxygen in common solvents [52]. The fact that $p \approx 1$ makes EPR oximetry quantitative, and therefore, lots of effort has been devoted to support this assumption [29]. D_{SP} is usually considered negligible in comparison to D_{O_2} [52]. Consequently, the effect of oxygen on the spectral line width is mainly influenced by the product $D_{\mathrm{O}_2} \cdot c_{\mathrm{O}_2}$ in a solvent, a fact which has been pointed out by Povich in 1975 [30]. Albeit, oxygen diffuses through solvents with high macroscopic viscosity about as easily as through water [52], making c_{O_2} the dominant variable. c_{O_2} in liquids is dictated by its solubility, which is the maximum amount of solute dissolved in a solvent in a saturated solution. According to Henry's law, the solubility of oxygen is in turn directly proportional to the pO_2 in the gas above the solvent:

$$\mathrm{pO}_2 = k_{\mathrm{H}} \cdot c_{\mathrm{O}_2}, \tag{1.5}$$

where k_{H} is Henry's law constant, which depends on the temperature, the solvent, and the solute [53]. The higher the pO_2, the higher c_{O_2} and ω_{obs}, and, thus, the broader the EPR line width. This linear relationship allows for quantitative oximetry measurements.

While the mechanism of oxygen induced line broadening is well understood for soluble EPR spin probes, it is rather complex for so-called particulate (insoluble) radicals, such as napthalocyanine and phthalocyanine radicals. A two-state spin model has been proposed [54, 55]. The unpaired electron is not only delocalized over the conjugated macrocycle [56]. Stacking on each other like a column [55–57] with very short interplanar distances, *i.e.*, 0.3 nm to 0.5 nm [57–59] further enhances delocalization since π orbitals can overlap intermolecularly [54]. Hence, the magnetic environment encountered by these so-called moving spins is effectively averaged, and the lines are very narrow [60]. This effect is called exchange narrowing [61]. Crystal defects, however, disturb the mobility and lead to so-called fixed spins with short relaxation times and broad EPR lines [55]. The interchange between the two spin states is too fast to be observable with EPR, such that only one

EPR line is detected [54, 62]. The ratio of fixed spins to mobile spins determines the apparent line width [54, 55]. Wide channels of 0.5 nm to 0.9 nm between the columns of macrocycles allow oxygen with a size of 0.28 nm·0.39 nm to diffuse [58]. Upon collision, line broadening is caused similarly via Heisenberg spin exchange as well as dipolar interactions. Additionally, oxygen, just like other crystal defects, might perturb the mobility of the spins resulting in more fixed spins, contributing to the line broadening [55]. In other words, since metallo(na)pthalocyanines are semiconductors, oxygen acts like a dopant [54, 56]. All in all, particulate radicals reflect the pO_2 in their material pores rather than the c_{O_2} in their surrounding medium. The line broadening is often much higher as compared to soluble probes. Perhaps, the collisions with oxygen are more effective because of cumulative effects and longer interaction times of oxygen-spin probe collisions [20].

1.3.3 Limitations

As also known for other oximetry techniques, EPR spectroscopy exhibits limitations. Exogenous stable radicals are needed, thus, tissue-spin probe interactions are possible. Further, changes in the EPR line widths might not solely caused by oxygen, but also by other paramagnetic molecules (*e.g.*, nitric oxide, nitrogen dioxide [58], the spin probe itself), solvent viscosity, and temperature. Hence, calibration is required to obtain absolute values of pO_2/c_{O_2}. A second issue arises with the signal intensity. To improve the SNR, metrological parameters like microwave power and modulation amplitude can be varied, taking into account signal saturation and/or line distortions, especially when the relaxation times are long. Increased measurement duration or multiple records and signal averaging are time-consuming and unsuitable for dynamic measurements, but sometimes necessary to achieve sufficient SNRs. A major drawback is the non-resonant absorption of microwave radiation in aqueous samples (dielectric loss), which limits the penetration depth. At X-band frequencies, microwave radiation penetrates aqueous samples only up to approximately 1 mm. Using low frequency EPR (L-band or less), the non-resonant absorption is decreased and undesired heating is minimized. However, the measurement depth (up to about 1 cm) is still insufficient for deeper lying regions in larger subjects, and the sensitivity is compromised. Another challenge during *in vivo* EPR experiments is the movement of animals, which can lead to deflections as high as the signal itself. Therefore, animals have to be restrained or anesthetized. Alternatively, implantable resonators can be applied, albeit invasive: A small loop is implanted at the site of interest and a larger loop is inductively coupled to the spectrometer [63]. Using this technique, oximetry was performed up to a depth of 8 cm and measurements in moving organs, *e.g.*, in the beating heart, were facilitated [63].

1.3.4 Spin probes

As already mentioned, there are two classes of oxygen-sensitive EPR spin probes: Soluble and particulate radicals. Soluble spin probes, *e.g.*, nitroxides and triarylmethyl (Trityl/TAM) radicals, are chemically well defined and can diffuse and distribute evenly within samples and tissues, allowing for EPR imaging [26]. They can chemically be altered to influence their distribution behavior [20, 64]. Deuterated trityl radicals and D-,15N-substituted nitroxides exhibit favorably narrow EPR lines [65, 66]. The EPR signal characteristics of soluble radicals might also be affected by their concentration or the properties of the solvent, such as viscosity and pH value [67–69].

The first trityl radical was prepared by Gomberg in 1900 [70]. To reduce hyperfine coupling with hydrogen nuclei and to achieve sharp single EPR lines, the phenyl rings were substituted with alkylthio moieties by Nycomed Innovation AB (Sweden, now GE Healthcare, UK) in the 1990s leading to the family of tetrathia-TAM radicals [71, 72]. Salts of these radicals showed good water solubility as well as stability in the presence of reducing reagents, such as ascorbate and glutathione [73]. Another family of trityl radicals used in this work, the tetrachloro-TAM radicals, was first introduced in 1967 [74]. Upon substitution of the six ortho positions with chlorine atoms, the central methyl carbon was sterically shielded, providing high chemical and thermal stability [75, 76]. Tetrachloro-TAM radicals show broader EPR lines due to coupling with the chlorine nuclei in close vicinity but are distinguished by better synthetic accessibility than tetrathia-TAM radicals. Trityl radicals have been employed not only in EPR oximetry [77–79] but also in many other applications, *e.g.*, specific detection of $O_2^{-\bullet}$ [80–83], pH measurements [84, 85], as well as analysis of redox status [86]. Trityl-based spin labels were used for distance measurements, *e.g.*, in nucleic acids [87]. Their long relaxation times made trityl radicals also attractive for pulsed EPR [88] and (pulsed) EPR imaging [89–91]. To achieve intracellular permeability, lipophilic triester derivatives were developed [79, 92].

Particulate materials have also attracted much attention. These radicals exhibit strong signals due to a high spin density [20, 26]. There is no concentration-dependent line broadening [93]. They do not distribute within samples/tissues and, hence, measure oxygen contents only at the implantation site. Thus, repeated and long term measurements are possible [20, 26]. A drawback is their deficiency in terms of the reproducibility of their preparation and properties [26]. The EPR properties of LiNc-BuO and other particulate spin probes are strongly affected by the characteristics and quality of the crystals, such as particle size and polymorphism [26, 94].

Important examples are carbon-based probes (coals and chars), such as India Ink, which was already approved for clinical applications [95], as well as lithium salts of phthalocya-

nine or naphthalocyanine derivates. In 1987, the most prominent and well-studied oxygen-sensitive derivative, lithium-phthalocyanine (LiPc), was synthesized as a semiconductor [56]. Further development led to oximetry probes with improved characteristics. The syntheses of lithium-naphthalocyanine (LiNc) [96], lithium-5,9,14,18,23,27,32,36-octa-*n*-butoxy-2,3-naphthalocyanine (LiNc-BuO) [97], and lithium-1,8,15,22-tetraphenoxyphthalocyanine (LiPc-α-OPh) [98] were reported recently. In this work, LiNc-BuO is subject to investigations. It has been used, *e.g.*, to monitor the oxygen consumption of endothelial cells in cell culture models [78, 99], for *in vivo* oximetry in muscle [97, 100–102], tumors [103–105], even xenograft tumors [106–108], or myocardium [109], and for EPR imaging in cancer spheroids [110]. Treatment of LiNc-BuO with a variety of biological oxidants and reductants, such as ROS, nitric oxide, glutathione, and ascorbate for 30 min did not have any effect the EPR stability (paramagnetism) or the oxygen sensitivity [97].

1.4 Formulations for spin probes

When EPR measurements are conducted in biological systems, the spin probes might lose their signal intensity and their oxygen responsiveness due to spin-probe tissue interactions [96, 111–113]. Soluble probes are rather sensitive to chemical reactions (*e.g.*, reduction or oxidation) [73, 80, 114, 115] and protein binding [79, 116–118]. Binding to proteins causes aggregation and is the main reason for toxicity of trityl radicals [119]. Implanted particulate materials are probably impacted by mechanical stress in certain tissues, altering the physicochemical properties of the crystals [113]. Furthermore, chemical changes at the surface might affect collisions of the oxygen sensitive centers with oxygen [112, 120]. Another issue can be a deposit of proteins forming a capsule, which acts as a physical barrier [111, 112].

Appropriate formulations are needed to prevent these interactions, to enhance the biocompatibility of the probes, and overcome toxicity concerns. On the other hand, the stability of the spin probes can be increased to enable repeated measurements. A pharmaceutic-technological approach is the incorporation into a suitable polymer, such as Poly(vinyl acetate) (PVAc). It is oxygen permeable, biocompatible, and – if at all – very slowly biodegraded [121], providing long term isolation of the material incorporated. PVAc has already successfully been used for film coatings of solid oral dosage forms [122], and for embedding LiPc crystals into polymer films [123]. Chemical alterations of the radicals [115] are no subject of this work.

To limit the degradation and toxicity of trityl radicals, they have been embedded into poloxamer 407 hydrogels [124] or covalently bond to dendrimers or poly(ethylene glycol) [73, 125, 126]. To achieve tissue selectivity, trityls have been conjugated [64]. However,

the oxygen sensitivity was often compromised. Soluble radicals can further be employed in lipophilic formulations to improve their oxygen sensitivity, which depends on the solvent and is rather low in water. Nitroxides and trityls have been incorporated into microspheres using bovine serum albumin (BSA) and hexamethyldisiloxane [127] or various other organic solvents [128]. Trityl radicals have been formulated as perfluorocarbon nanoemulsions [129, 130] or solutions [77], and polydimethylsiloxane (PDMS) chips [131]. However, these formulations showed limitations in either their biocompatibility (BSA), long term stability, or intravascular injectability.

The present work shows the incorporation of trityl radicals into oily-core nanocapsules (NCs) as a promising approach. Highly lipophilic encapsulated probes are expected to stay inside the NCs without being partitioned to the outer aqueous phase. Thereby, protein-binding can be prevented and the capsule shell might provide protection against oxidoreductants [73, 115, 128]. Moreover, a defined microenvironment inside the NC is created, which ensures specificity and unchanged sensitivity of the sensors to oxygen. MCT was chosen as a lipophilic solvent because it is considered to be biologically inert. It is established as an ingredient in medicinal products and is also administered parenterally, *e.g.*, in nutrition nanoemulsions [132]. However, it exhibits a relatively high viscosity of about $25\,\text{mPa}\,\text{s}$ to $33\,\text{mPa}\,\text{s}$ at $20\,°\text{C}$. As a consequence, the EPR lines are broadened. This may affect the resolution of the EPR spectra and complicate EPR studies. In addition, the SNR is generally lower in highly viscous media since the EPR amplitude is inversely proportional to the square of the line width [133]. As an alternative, the less viscous isopropyl myristate (IPM; $5\,\text{mPa}\,\text{s}$ to $6\,\text{mPa}\,\text{s}$ at $20\,°\text{C}$)was also investigated. It is nontoxic and commonly used, *e.g.*, in cosmetics or topical pharmaceutical formulations [134].

Suitable formulations for particulate radicals prevent reactions with tissues and enhance the physical stability of the sensors when incorporated into a polymer [112, 120, 123, 135–137]. In previous studies, particulate probes have been embedded in films of various polymers [120, 123], polytetrafluoroethylene (PTFE) (derivatives) films [136, 138] or cylindrical inserts [113], or PDMS inserts/chips [112, 137, 139, 140]. These devices are retrievable but need to be implanted by incision. This may lead to tissue injury, which could distort the oxygen measurements. However, for preclinical investigations of tissue oxygenation in small animals, easily injectable probes are needed, which do not necessarily have to be retrievable. Carbon materials have been microencapsulated into several polymers. However, problems occurred with aggregation, injectability, or stability of the oxygen response [141]. More promising results have been obtained with cellulose nitrate [112, 135]. Very recently, Bhallamudi *et al.* reported successful incorporation of LiNc-BuO into $300\,\text{nm}$ to $500\,\text{nm}$ PDMS-core/polycaprolactone (PCL)-shell nanofibers by simultaneous co-axial electrospinning [142]. While these nanosensors impress by very rapid response

and recovery times due to the high porosity and large surface area, they also have to be implanted surgically. Here, the particulate radical LiNc-BuO is formulated as polymeric nanoparticles (NPs) and microparticles (MPs). These formulations are easily injectable and cause less trauma to the injection site. Moreover, the distribution in the tissue of interest should be improved, giving better information on the average pO$_2$, especially in tissues with heterogeneous oxygenation.

1.5 Research objectives

The aim of this project is the noninvasive *in vivo* measurement of tissue oxygenation in suitable preclinical tumor models using EPR spectroscopy. In this regard, oxygen sensitive spin probes (stable radicals) need to be administered. Pioneering work has been done to find new appropriate materials. However, synthesis of these radicals is sophisticated and sometimes hard to reproduce. Variations in their physicochemical properties and environmental parameters might affect the oxygen sensing properties. Additionally, there are concerns regarding their biocompatibility and *in vivo* stability. To assess the suitability of certain spin probes as oxygen sensors, and to develop appropriate formulations for *in vivo* measurements, the following objectives have been set.

- Physicochemical analysis to affirm the identity and purity of the radicals

- Comprehensive characterization of the stability, sensitivity, linearity, accuracy, and reversibility of the oxygen response

- Verification of specificity within physiological conditions (no impact of other environmental parameters, *e.g.*, pH value, viscosity, temperature, polarity)

- Development of appropriate formulations with reproducible properties, which enhance the biocompatibility, preserve the oxygen responsiveness, facilitate the *in vivo* administration, avoid tissue injury, and enable repeated/long term measurements

- Physicochemical characterization of these formulations (*e.g.*, size, morphology), confirmation of stability, oxygen sensitivity, and biocompatibility

- *In vivo* application of suitable formulations, and comparison with reference methods to verify reliability and accuracy

This work presents experiments investigating the aforementioned issues by utilizing two distinct types of spin probes – soluble trityl radicals and particulate LiNc-BuO.

2 Experimental

2.1 Materials

2.1.1 EPR spin probes

2.1.1.1 Trityl radicals

Various tetrathia- and tetrachloro-TAM radicals with hydrophilic (TAM, dTAM) as well as lipophilic properties (TAM-EE, TAM-*t*BE, dTAM-EE, dTAM-dEE, Cl-TAM-EE, Cl-TAM-*t*BE) had been synthesized, purified, and analytically characterized by cooperation partners (research group of Prof. Dr. Peter Imming, Martin-Luther-Universität Halle-Wittenberg, Halle (Saale), Germany). Synthetic and analytical details were published cooperatively [143] and further discussed in the Doctoral thesis of Marwa Aly El-metwaly Mohamed Elewa [144]. The chemical formulas are shown in figure 2.1.

dTAM: $R^1 = CD_3$, $R^2 = COOH$

TAM: $R^1 = CH_3$, $R^2 = COOH$

TAM-EE: $R^1 = CH_3$, $R^2 = COOCH_2CH_3$

TAM-*t*BE: $R^1 = CH_3$, $R^2 = COOC(CH_3)_3$

dTAM-EE: $R^1 = CD_3$, $R^2 = COOCH_2CH_3$

dTAM-dEE: $R^1 = CD_3$, $R^2 = COOCD_2CD_3$

Cl-TAM-EE: $R = COOCH_2CH_3$

Cl-TAM-*t*BE: $R = COOC(CH_3)_3$
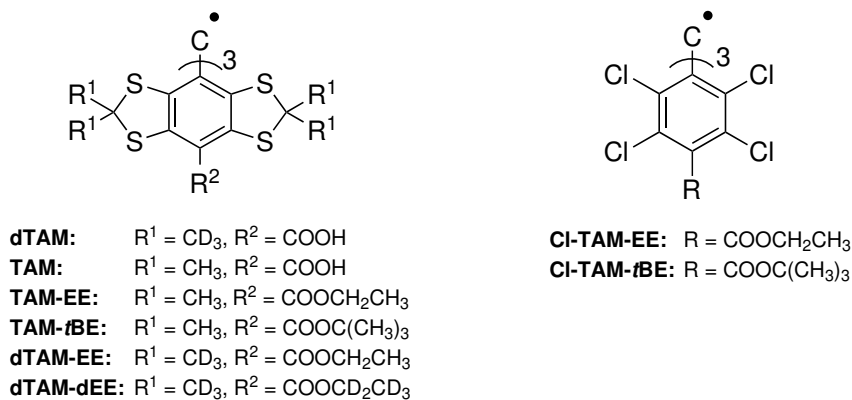
Figure 2.1: Chemical formulas of tetrathia-TAM and tetrachloro-TAM radicals.

2.1.1.2 LiNc-BuO and Nc-BuO

LiNc-BuO (figure 2.2) was purchased as microcrystalline powder from Panslavia Chemicals LLC (Milwaukee, USA; now HPPE LLC, Columbus, USA). Synthesis used 5,9,14,18,23,-27,32,36-octa-*n*-butoxy-2,3-naphthalocyanine (Nc-BuO) as educt and followed the repor-

ted instructions [94, 97]. Two different batches have been prepared, which are referred to as batch 1 (LOT No. OZ40/51211) and batch 2 (LOT No. RB1-16/41611). The educt Nc-BuO was obtained by the same supplier (LOT No. OZ62/72611).
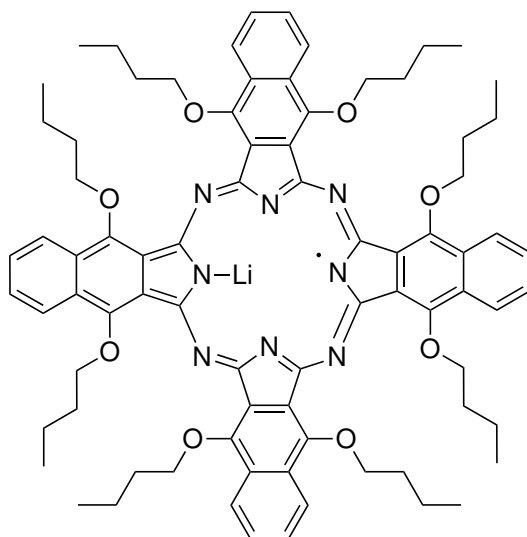
Figure 2.2: Chemical formula of LiNc-BuO.

2.1.2 Miscellaneous

2.1.2.1 PVAc

PVAc was isolated from Kollicoat® SR 30 D, which was kindly provided by BASF SE (Ludwigshafen, Germany). Referring to the Manufacturer's quality certificate, the dispersion contained about 27 % (m/V) PVAc with a mean relative molecular mass of about 450 000 according to the European Pharmacopoeia (Ph.Eur.) [145], 2 % (m/V) polyvinyl-pyrrolidone (PVP), and 0.3 % (m/V) sodium dodecyl sulfate (SDS). The dispersion was cast onto planar PTFE coated plates. The dried films were washed in water for five days to remove the water-soluble excipients, again dried, and ground.

Proton (^{1}H) NMR spectroscopy

The identity and purity, *i.e.*, the absence of any water-soluble excipients, were verified by NMR spectroscopy. Samples were dissolved ($c = 10\,\text{mg/ml}$) in deuterated dimethyl sulfoxide (DMSO) (Sigma-Aldrich Chemie, Steinheim, Germany) containing 0.1 % (v/v) tetramethylsilane (TMS) as an internal standard for calibration of chemical shifts. ^{1}H NMR spectra were recorded on a 400 MHz VNMRS (Agilent Technologies, Santa Clara,

USA) with VNMRJ 3.2 software and processed using MestReNova software. As reference materials, pure PVAc beads (molecular weight approximately $360\,000\,\mathrm{g/mol}$, Vinnapas® UW 10 FS, Wacker, Germany), PVP K 25 (Serva Feinbiochemica, Heidelberg, Germany), SDS (Merck, Darmstadt, Germany), and poly(vinyl alcohol) (PVA, Gohsenol® EG-05 PW, Nippon Gohsei, Osaka, Japan) were used.
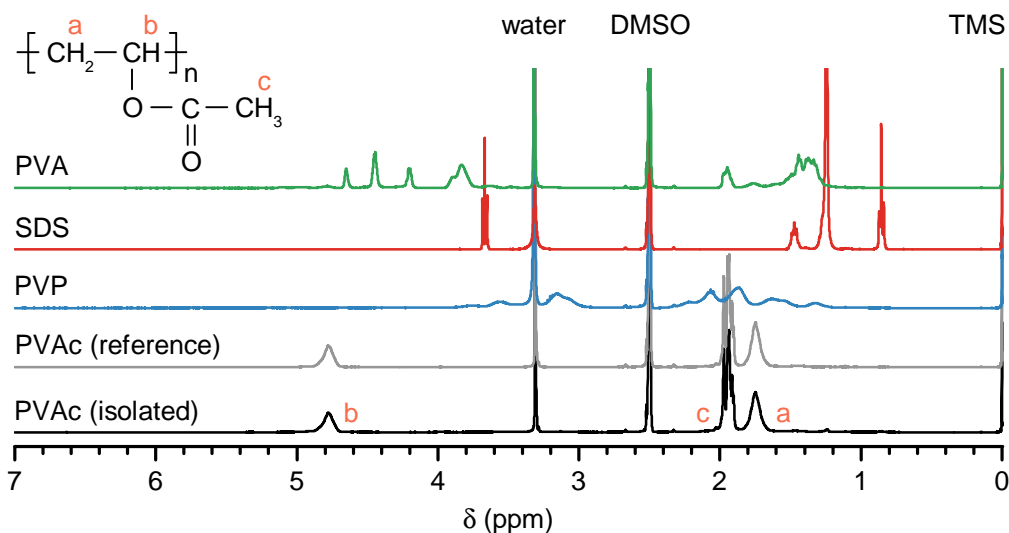
Figure 2.3: ^{1}H NMR spectra of isolated PVAc as well as PVA, SDS, PVP, and PVAc references as measured in deuterated DMSO. Chemical shifts δ are reported in parts per million (ppm) relative to the peak position of TMS. Note that the DMSO peak was assigned to protons in residual partly undeuterated DMSO, the water peak was due to absorption of moisture during sample preparation. The peaks were assigned to the corresponding protons as follows: (a) β protons in methylene group, (b) α protons in methine group, and (c) protons in acetyl group (see chemical formula of PVAc). Only the pertinent range is shown here - the whole spectrum of PVAc can be found in the appendix (figure A.1).

2.1.2.2 Stabilizers

Poloxamer 188 and 338 (Lutrol® F 68 and 108) were purchased from BASF SE, polysorbate 80 from Caesar and Loretz GmbH (Hilden, Germany), Span® 80 (sorbitan monooleate) from Croda (Barcelona, Spain), and PVA (Emprove® 8-88) from Merck.

2.1.2.3 Solvents and oils

Water was used in doubly distilled quality. Other solvents are listed in table 2.1.

Table 2.1: Solvents and oils as well as their suppliers.

Solvent	Supplier
Acetone	Carl Roth or VWR international, Fontenay-sous-Bois, France
Acetonitrile	Grüssing
Dichloromethane	Carl Roth
N,*N*-Dimethylformamide (DMF)	Carl Roth
DMSO	Carl Roth
Ethanol	Merck
Ethyl acetate	VWR international, Leuven, Belgium
Glycerol 86 % to 88 %	Kmf Laborchemie, Lohmar, Germany
Glycerol 99.5 %	VWR international, Fontenay-sous-Bois, France
n-Hexane	Grüssing
Isopropanol	Grüssing
Isopropyl myristate (IPM)	Hansen and Rosenthal, Hamburg, Germany
Medium-chain triglycerides (MCT)	Hansen and Rosenthal
Paraffin, liquid	Hansen and Rosenthal
1-Propanol	Merck
Tetrahydrofuran (THF)	VWR International, Leuven, Belgium

2.1.2.4 Buffer solutions and media

Buffer salts and their compositions are given in tables 2.2 and 2.3, respectively.

Table 2.2: Ingredients of buffer solutions and media as well as their suppliers.

Substance or medium	Supplier
β-Nicotinamide adenine dinucleotide, reduced disodium salt hydrate (NADH)	Sigma-Aldrich Chemie
$CaCl_2$	Merck
Ethylenediaminetetraacetic acid (EDTA)	Merck
Fetal calf serum	Merck
4-(2-Hydroxyethyl)-1-piperazine-ethanesulfonic acid (HEPES)	Sigma-Aldrich Chemie
Glucose	Sigma-Aldrich Chemie
KCl	Merck or Grüssing, Filsum, Germany
KH_2PO_4	Grüssing
L-glutamine	Serva Electrophoresis, Heidelberg, Germany
LiCl	Carl Roth, Karlsruhe, Germany

Table 2.2: Ingredients of buffer solutions and media as well as their suppliers.

Substance or medium	Supplier
$MgCl_2$	Merck
NaCl	Carl Roth or Grüssing
$NaHCO_3$	Merck
Na_2HPO_4	Grüssing
Na_2HPO_4 x 2 H_2O	Merck
NaH_2PO_4 x 2 H_2O	Merck
NaN_3	Merck Schuchardt, Hohenbrunn Germany
NaOH	Carl Roth
Roswell Park Memorial Institute (RPMI)-1640 medium	Merck
Sodium pyruvate	Sigma-Aldrich Chemie
Tris(hydroxymethyl)aminomethane (TRIS)-HCl	Carl Roth
Triton® X-100	Sigma-Aldrich Chemie

Table 2.3: Composition and properties of various buffer systems.

Name	Abbre-viation	Buffer salts	Ionic strength (mmol/l)	Osmolarity (mosmol/l)	pH va-lue
Phosphate-buffered saline pH 7.4	PBS 7.4	Na_2HPO_4, KH_2PO_4, NaCl	189	327	7.4
Phosphate buffer 0.02 M, pH 7.4	PB 7.4	Na_2HPO_4, KH_2PO_4	49	55	7.4
Phosphate-buffered saline pH 6.2	PBS 6.2	Na_2HPO_4, KH_2PO_4, NaCl	180	349	6.2
Phosphate buffer 0.04 M pH 6.2	PB 6.2	Na_2HPO_4, KH_2PO_4	52	86	6.2

2.1.2.5 Animals and cells

All *in vivo* studies had been approved by the animal ethics committee of Saxony-Anhalt, Germany (reference numbers: 42502-2-1236 MLU and 42502-2-1098 MLU). Animal care and experiments complied with European and German regulations and guidelines [146]. Hairless immunocompetent SKH1-*Hr*hr mice, Copenhagen rats, as well as Wistar rats were

generally obtained from the Zentrum für medizinische Grundlagenforschung of the Martin Luther University Halle-Wittenberg. Exceptionally, some Wistar rats were purchased from Charles River Laboratories (Wilmington, USA). Animals were housed in the animal care facility of the Martin Luther University Halle-Wittenberg under controlled conditions (12 h day/night cycle, 24 °C) and allowed access to food and water *ad libitum.* The subline AT-1 of the rat R-3327 Dunning prostate tumor (AT1) and the rat mammary tumor cell line Walker-256 (W256) were obtained from CLS (Eppelheim, Germany).

2.1.2.6 Narcotics

For implantation of tumors and/or MPs, animals were anesthetized inhalatively with an isoflurane (Forene®, Abbott, Wiesbaden, Germany)/oxygen mixture. For EPR measurements, anesthetics were administered intraperitoneally, in particular, a mixture of ketamine hydrochloride (Ketavet®, Pfizer, Berlin, Germany) and xylazine hydrochloride (Rompun®, Bayer HealthCare, Leverkusen, Germany) was used for mice and sodium pentobarbital (Narcoren®, Merial, Hallbergmoos, Germany) for rats, respectively.

2.1.2.7 Antibodies, substrates, and others

All other materials are given in table 2.4.

Table 2.4: Antibodies, substrates, and others as well as their suppliers.

Substance	Supplier
Bicinchoninic acid assay	Thermo Fisher Scientific, Waltham, USA
Caspase 3 substrate IV	Merck
CD163 antibodies	AbD Serotec, Kidlington, UK
Fluorescence mounting medium	Dako Deutschland, Hamburg, Germany
Mouse CD31 antibodies	Merck
Pimonidazole-HCl and affinity purified rabbit anti-pimonidazole antibody (Hypoxyprobe™-1 Omni Kit)	Hypoxyprobe, Burlington, USA
Secondary fluorescein isothiocyanate coupled antibody	Rockland Immunochemicals, Limerick, USA

2.2 Physicochemical characterization of the spin probes

2.2.1 Trityl radicals

2.2.1.1 EPR spectroscopy and oxygen response

Radical dTAM was dissolved ($c = 50\,\mu$M) in the four different buffer systems listed in table 2.3. Additionally, dTAM was dissolved ($c = 50\,\mu$M) in mixtures of PBS 7.4 and absolute glycerol, the glycerol content of the mixtures ranging from ($0\,\%$ to $90\,\%$ glycerol in water, m/m). TAM was dissolved ($c = 50\,\mu$M) in PBS 7.4. Lipophilic radicals were dissolved ($c = 1\,$mM) in MCT as well as IPM. All solutions were measured at defined oxygen contents by EPR spectroscopy at L-band (section 2.4.1).

2.2.2 LiNc-BuO

2.2.2.1 EPR spectroscopy and oxygen response

Dry LiNc-BuO crystals were measured under defined oxygen contents by EPR spectroscopy at L-band (section 2.4.1).

2.2.2.2 Microscopy

LiNc-BuO crystals were observed with a transmitted-light microscope (Axiolab, Carl Zeiss Microscopy, Jena, Germany) to obtain information about their size and morphology. Images were taken by a mounted Olympus UC30 digital camera operated by Olympus Stream Motion 1.7 software (Olympus, Tokio, Japan).

2.2.2.3 Solubility

Increasing volumina of various solvents, ranging from $1\,\mu$l to $10\,$ml, were added to accurately weighted aliquots ($1\,$mg) of LiNc-BuO crystals. After at least $24\,$h of incubation under ambient conditions, the samples were inspected visually. LiNc-BuO was considered being dissolved if crystals were no longer detectable after incubation. The solubility was evaluated according to Ph.Eur. [147] depending on the volume of solvent, which was added until the crystals had been dissolved. Solutions/dispersions in ($1\,$ml) were measured at L-band (section 2.4.1) on the day of preparation.

2.2.2.4 Stability

Aliquots of LiNc-BuO crystals ($1\,$mg) were stored under various conditions (table 2.5) and measured at L-band (section 2.4.1) up to 3 months after preparation.

Table 2.5: Storage conditions for stability testing of LiNc-BuO.

Abbreviation	Medium	Temperature (°C)	Relative humidity (%)
dry, 5 °C	dry	5 ± 3	–
dry, 20 °C, 40 %	dry	20 ± 5	40 ± 5
dry, 20 °C, 75 %	dry	20 ± 5	75 ± 5
water, 5 °C	water	5 ± 3	–
water, 20 °C	water	20 ± 5	–
PBS 6.2, 20 °C	PBS 6.2	20 ± 5	–
PBS 7.4, 20 °C	PBS 7.4	20 ± 5	–

2.2.2.5 X-ray diffraction (XRD)

Powder XRD patterns were acquired from Nc-BuO and LiNc-BuO on a flat sample holder applying a D8 Advance powder diffractometer (Bruker, Billerica, USA) in Bragg-Brentano geometry (θ/θ) using Cu K$_\alpha$ radiation ($\lambda = 0.154$ nm) and a one-dimensional silicon strip detector (LYNXEYE$^{\text{TM}}$). Diffractograms were obtained in an angular range of $2\theta = 5°$ to $50°$ with a step size of $0.01°$ and a steptime of 1 s per step. For comparison with literature data, the PowderCell software (Federal Institute for Materials Research and Testing, Berlin, Germany) was used. The powder XRD pattern of the tetragonal polymorph was simulated in PowderCell from a reported crystal information file [94], the one of the triclinic form was digitized as accurately as possible from a published powder diffractogram [58] using the Engauge Digitizer 4.1 software (Mark Mitchell, free software).

2.2.2.6 High resolution mass spectrometry (HRMS)

High resolution mass spectra were recorded on an orbitrap XL mass spectrometer (Thermo Fisher Scientific) with a resolving power of $100\,000$ at m/z 400. Samples were dissolved in THF and introduced to the MS by static nano-electrospray ionization. For comparison, calculation of the monoisotopic mass, where atomic masses of each atom are based on the most abundant isotope for the element, was performed using the ChemBioDraw Ultra 12.0 software (PerkinElmer Informatics, Waltham, USA).

2.2.2.7 Ultraviolet–visible–near infrared (UV/Vis/NIR) spectroscopy

Solutions of Nc-BuO ($c = 5$ µg/ml) and LiNc-BuO ($c = 20$ µg/ml) in THF were measured in cuvettes using a Lambda 900 UV/Vis/NIR spectrometer (PerkinElmer instruments, Norwalk, USA). THF was used as blank. Spectra were obtained in a wavelength range of

300 nm to 1200 nm with a data interval of 2 nm and a velocity of 230.77 nm/min (UV/Vis region) and 250 nm/min (NIR region), respectively.

2.2.2.8 Infrared (IR) spectroscopy

IR spectra of Nc-BuO and LiNc-BuO were obtained by a Fourier-transform IR spectrometer IFS 28 (Bruker Optik, Ettlingen, Germany) equipped with a ZnSe attenuated total reflection (ATR) crystal with an angle of incidence of 45°. Measurements were conducted in a wavelength range of $680 \, \text{cm}^{-1}$ to $4000 \, \text{cm}^{-1}$.

2.2.2.9 Differential scanning calorimetry (DSC)

The thermal behaviour of LiNc-BuO was investigated by DSC (DSC 200, Netzsch, Selb, Germany). Dry crystals (2 mg to 5 mg) were measured in sample aluminium pans against an empty pan according to the following scheme: First, the samples were heated from 25 °C to 300 °C at 1 K/min, subsequently, the samples were cooled from 300 °C to 25 °C at −5 K/min, and finally, the samples were heated again using the same parameters.

2.3 Formulation preparation

2.3.1 Nanoencapsulation of trityl radicals

NCs were prepared by interfacial polymer deposition following solvent displacement, a method which is also known as nanoprecipitation and was first described and patented by Fessi *et al.* [148]. Isolated PVAc was dissolved in acetone (0.2 %, m/m). An oily solution of dTAM-dEE ($c = 1 \, \text{mM}$) was added to form the organic phase. The organic phase was then injected slowly into an aqueous solution (1:2, v/v) containing either poloxamer 188 or polysorbate 80 under vigorous magnetic stirring at 1000 rpm (revolutions per minute) (approximately 34 g at r_{max}). After stirring for at least 10 min, acetone and part of the water were removed by evaporation under reduced pressure at a maximum temperature of 30 °C. The final NCs contained 0.4 % (m/m) PVAc and either 2.8 % (v/m) MCT and 1 % (m/m) poloxamer 188 or 2.4 % (v/m) IPM and 0.8 % (m/m) polysorbate 80 and were stored at 2 °C to 8 °C for further use.

2.3.2 Nanoformulation of LiNc-BuO

2.3.2.1 Solvent displacement

Similar to NCs, NPs were prepared by nanoprecipitation. For coated NPs, LiNc-BuO (0.05 %, m/m) and isolated PVAc (0.25 %, m/m) were dissolved in THF to form the

organic phase. To obtain uncoated nanocrystals, LiNc-BuO was dissolved in THF (0.05 %
to 0.5 %, m/m) and PVAc was omitted. The organic phase was injected slowly into an
aqueous solution containing poloxamer 188 (0.5 %, m/m) under vigorous magnetic stirring
at 1000 rpm (approximately 34 g at r_{max}). For uncoated NPs the ratio was 1:2.5 to 1:25
(v/v) and for coated NPs 1:2 (v/v), respectively. PVA and polysorbate 80 (0.1 %, m/m)
were tested as alternative stabilizers. After stirring for 5 min, THF and part of the water
were removed by evaporation under reduced pressure at a maximum temperature of 30 °C
to obtain following final concentrations: Uncoated NPs, 0.025 % to 0.125 % (m/m) LiNc-
BuO, coated NPs, 0.125 % (m/m) LiNc-BuO and 0.5 % (m/m) PVAc, as well as 2.5 %
(m/m) poloxamer 188. NPs were stored at 2 °C to 8 °C for further use.

2.3.2.2 Microfluidics

Based on the nanoprecipitation method described above, the process parameters were
adapted to develop a microfluidic preparation method. To obtain the organic phase,
LiNc-BuO was dissolved in THF (0.02 % to 0.2 %, m/m) and filtered (PTFE, pore size
0.45 µm). The aqueous phase was poloxamer 188 (0.5 %, m/m) in water, pre-filtered (pore
size 0.22 µm). Each solution was placed separately in a Mitos p-pump basic connected to
a compressor. Mixing took place in a micromixer chip with twelve mixing stages, which
was linked via 4-way linear connectors and fluorinated ethylene propylene (FEP) tubing
with an inner diameter of 250 µm. Solutions were filtered priorly using stationary ferrules
with integrated filter (pore size 2 µm). Flow rates were controlled by Mitos flow rate
sensors. Prior to NP preparation, a flow rate calibration with THF had been carried out.
The microfluidic system was operated by Mitos flow control center 2.3.7 software. All the
components used in the microfluidic system were purchased from Dolomite (The Dolomite
Centre, Royston, UK). Precipitated NPs were collected in a beaker containing about 5 ml
aqueous phase and kept under continuous magnetic stirring.

2.3.2.3 Nanomilling

A wet grinding feasibility study was performed with aliquots of 15 mg LiNc-BuO. As dis-
persion media, polysorbate 80 in water (4 %), poloxamer 108 in water (0.5 %), and a mix-
ture of polysorbate 80 (4 %) and ethanol (10 %) in water were used. Samples were milled
using a Pulverisette 7 classic line planetary ball mill (Fritsch, Idar-Oberstein, Germany)
equipped with 12 ml zirconium oxide grinding bowls. Zirconium oxide beads (SiLibeads®,
ZY-P 0.2 mm to 0.3 mm, Sigmund Lindner, Warmensteinach, Germany) were used for
grinding. An aliquot of 75 mg slurry (20 % LiNc-BuO in dispersion medium) was milled
with 5 g beads for 30 min at 800 rpm rotational speed. Grinding was performed in 60 cycles

of 30 s milling/30 s pause to allow the samples to cool down. Alternatively, the samples were milled for 180 min at 200 rpm performed in 360 cycles of 30 s milling/30 s pause.

2.3.3 Preparation of LiNc-BuO loaded MPs

MPs were prepared using an oil-in-oil (o/o) emulsion solvent evaporation method, which was adapted from Hyon and Ikada [149] (figure 3.23). Acetonitrile was added to PVAc and LiNc-BuO crystals. The mixture was stirred using both magnetic stirring and vortexing until PVAc was dissolved completely (10 % to 25 %, m/m) and LiNc-BuO was dispersed homogeneously (spin probe-to-polymer ratio 1:20 to 1:5, m/m). The suspension was dropped into liquid paraffin containing 2 % (m/m) Span$^®$ 80 at a ratio of 1:10 (m/m) under magnetic stirring at 1000 rpm (approximately 43 g at r_{max}). The agitation was continued for about 20 h till the evaporation of acetonitrile was completed. *n*-Hexane was added at a ratio of 1:1 (m/m), and MPs were hardened for 1 h at 400 rpm (approximately 7 g at r_{max}). MPs were harvested by filtration and washed with *n*-hexane until the filtrate was colorless. Finally, MPs were vacuum dried and stored at 2 °C to 8 °C for further use.

2.4 General characterization methods

2.4.1 EPR spectroscopy

2.4.1.1 Instrumentation

L-band

If not stated otherwise, EPR measurements were performed in glass vials using an L-band EPR spectrometer at 1.3 GHz (Magnettech, Berlin, Germany) equipped with a re-entrant resonator. In general, measurements were conducted under ambient conditions without temperature control. The modulation frequency was 100 kHz and the microwave power was set to <1 mW for trityl radicals and <10 mW for LiNc-BuO, respectively. The sweep was chosen in dependence of the signal line width, mostly in the range of 0.5 mT to 2.0 mT. The scan time was adjusted according to both the sweep and the signal intensity in order to obtain sufficient signal-to-noise ratios. Usually, a scan velocity of 10 µT/s to 25 µT/s was sufficient. However, if a very high resolution was needed, *e.g.*, due to hyperfine splitting, or when the signal amplitude was low, *e.g.*, when modulation side bands were measured or during some *in vivo* measurements under high inspiratory oxygen content, the scan velocity had to be decreased till 0.25 µT/s in some cases. The modulation amplitude was carefully chosen, such that line distortions were avoided all the time. In general, it was set to less than one fifth of the line width [49].

X-band

Measurements were performed in capillaries with aliquots of 50 µl each employing a bench-top X-band EPR spectrometer at 9.30 GHz to 9.55 GHz (Miniscope MS 200, Magnettech, Berlin, Germany). For typical measurement parameters, see paragraph L-band.

2.4.1.2 Analysis of EPR spectra

The MagicPlot software (Magicplot Systems, St. Petersburg, Russia) was mainly used for analysis of the spectra, in particular for simulation. Multiplot software (Magnettech) was sometimes used for comparison. In case of baseline drifts, the baseline correction of the Analysis (L-band spectra) or Easybatch (X-band spectra) software (both provided by Magnettech) were used prior to simulation. The measurement files (.cu1 and .cu3) were converted into ASCII tables using a custom graphical user interface in MATLAB R2011b (MathWorks, Natick, USA).

EPR line width

In general, a first-derivative Lorentzian function was fitted to the data to accurately determine the apparent Lorentzian ΔB_{PP} [51]. Line widths $<7.8 \, \mu T$ were assessed by measuring phase shifted. Thereby, the two modulation side bands, having the same line width as the main line, were gathered without the main line. In this case, two Lorentzian functions with a distance of $\pm 3.6 \, \mu T$ from the main line were fitted to the data to extract the line width information. If a superposition of multiple species was gained *in vivo*, the weighted mean of the line widths was calculated. The maximum relative fit error was 2.5 %.

EPR signal intensity

A first-derivative Lorentzian function was fitted to the recorded data and the intensity was calculated as the second integral of the fit function.

2.4.2 Measurements at defined oxygen contents

Samples were flushed with either pure nitrogen or defined mixtures of oxygen and nitrogen at a flow rate of approximately 2 l/min. An anesthesia gas mixer with flow meter tubes (Dräger, Lübeck, Germany) provided defined gas mixtures. The exact oxygen content (in %) in the gas above the solution/solid was confirmed by a needle-type optical oxygen microsensor with temperature control (Type PSt1, PreSens - Precision Sensing, Regensburg, Germany) directly before and after the EPR measurements. For better comparability with literature data, the pO_2 is given in mmHg. It was calculated assuming ambient conditions, *i.e.*, $1 \, \% \, O_2 \,\hat{=}\, 7.42 \, mmHg \, pO_2$.

Oily-core NCs or solutions of trityl radicals were flushed using septum glass vials and cannulae directly before the EPR measurements and measured at L-band at 20 °C. Dry LiNc-BuO loaded MPs or uncoated LiNc-BuO crystals (≈ 2 mg) were filled into PTFE tubes and flushed during EPR measurements using a custom-built sample holder. Measurements were performed at L-band equipped with a surface coil. Not only the oxygen content, but also the temperature inside the sample holder was confirmed directly before and after the EPR measurements by use of a temperature sensor (PreSens - Precision Sensing) coupled to the oxygen microsensor device. The temperature was kept at (37.0 ± 1.0) °C. To investigate the *ex vivo* oxygen response of MPs, MP containing tumor tissues were homogenized, filled into septum glass vials, flushed with either air or nitrogen using cannulae, and measured at L-band at 20 °C.

2.4.2.1 Oxygen calibration

Oxygen sensitivities were determined by plotting the EPR line widths as a function of the oxygen content and calculating the slope of the linear regression fit using the OriginPro 9.0.0 software (OriginLab, Northampton, USA).

2.4.3 Determination of oxygen solubilities

Gas chromatography was used to determine oxygen contents in MCT and IPM. Oils were equilibrated in air at 22 °C. After vacuum extraction, the gas mixtures were passed through a molecular sieve 0.5 nm packed column using argon as carrier gas in a gas chromatograph with flame ionization, methanizer, and thermal conductivity detectors (TOP TOGA GC system with gas extractor, ECH Elektrochemie, Halle, Germany). The area under the curve was determined, and oxygen concentrations were calculated by comparing with calibrations obtained from external standard gas mixtures.

2.5 Physicochemical characterization of nanoformulations

2.5.1 Particle size and morphology

2.5.1.1 Dynamic light scattering (DLS)

Particle sizes of NPs or NCs were measured by DLS, also referred to as photon correlation spectroscopy (PCS), using the Zetasizer Nano ZS (ZEN3600, Malvern Instruments, Worcestershire, UK). Each sample was diluted with filtered (pore size 0.22 µm) water. Each sample of oily-core NCs was diluted 1:25 (v/v). LiNc-BuO containing NPs were measured with a dilution of 1:50 (v/v). Samples were equilibrated at 25 °C and measured

with 15 runs for 10 s each in the middle of the cuvette. The backscattering mode with an angle of 173° was used to reduce the effect of dust or multiple scattering. Measurements were conducted three to five times to ensure the data did not show any drifts. The viscosity was assumed to be 0.89 mPa s (at 25 °C). Built-in algorithms of the Zetasizer software 6.30 (Malvern Instruments) were used to calculate the size from the correlation function, *i.e.*, the mean hydrodynamic diameter (z-average) as well as the polydispersity index (PdI) were obtained by simple cumulant analysis, and intensity size distributions by more complex fitting algorithms.

2.5.1.2 Nanoparticle tracking analysis (NTA)

NTA particle size measurements were perfomed using a NanoSight NS300 (Malvern Instruments) with NTA software 2.3 build 0013 (Malvern Instruments). Each sample was diluted with filtered (pore size 0.22 µm) water. Oily-core NCs and LiNc-BuO containing NPs were diluted approximately 1:10000 (v/v). The measured concentrations were 7×10^8 particles/ml (MCT NCs) and 10×10^8 particles/ml (IPM NCs), respectively. The measured concentrations were 10×10^8 particles/ml (coated NPs) and 8×10^8 particles/ml (uncoated NPs), respectively. Samples were measured at room temperature for 1 min.

2.5.1.3 Transmission electron microscopy (TEM)

Freeze-fracture- as well as cryo-TEM were used to investigate the size and morphology of NPs and NCs. The obtained electron microscopic images were analyzed using the measureIT software (Olympus Soft Imaging Solutions, Münster, Germany). NCs were measured at a concentration of $4 \, \mathrm{mg_{(PVAc)}/ml}$. NPs were investigated without dilution at a concentration of $c = 1.25 \, \mathrm{mg_{(LiNc-BuO)}/ml}$.

Freeze-fracture-TEM

To obtain images of freeze–fractured replica, the samples were freeze fixed 1 day after preparation using a propane jet-freeze device (JFD 030, BAL-TEC, Balzers, Lichtenstein). Thereafter, the samples were freeze–fractured at −150 °C without etching with a freeze–fracture/freeze etching system BAF 060 (BAL-TEC, Balzers, Liechtenstein). The surfaces were shadowed with platinum to produce good topographic contrast (2 nm layer, shadowing angle 45°) and subsequently with carbon to stabilize the ultrathin metal film (20 nm layer, shadowing angle 90°). The replica were floated in NaCl (4 %) for 30 min, rinsed in distilled water (10 min), washed in 30 % acetone for 30 min, and rinsed again in distilled water (10 min). Thereafter, the replica were mounted on copper grids, coated with Formvar film, and observed with a transmission electron microscope (LIBRA 120

PLUS, Carl Zeiss Microscopy, Jena, Germany) operating at 120 kV. Pictures were taken with a BM-2k-120 Dual-Speed on axis SSCCD-camera (TRS, Moorenweis, Germany).

Cryo-TEM

Vitrified specimens for cryo-TEM were prepared by a blotting procedure performed in a chamber with controlled temperature and humidity using an EM GP grid plunger (LEICA, Wetzlar, Germany). One drop of the sample solution was placed onto an EM grid coated with a holey carbon film (C-flatTM, Protochips, Raleigh, USA). Excess solution was then removed with a filter paper, leaving a thin film of the solution spanning the holes of the carbon film on the EM grid. Vitrification of the thin film was achieved by rapid plunging of the grid into liquid ethane held just above its freezing point. The vitrified specimens were kept below 180 K during storage, transfers, as well as investigation. The microscope was equipped with a cryotransfer system (626, Gatan, Pleasanton, USA).

2.5.2 Measurements of zeta potential (ZP) and pH value

The ZP of the NC dispersions was determined by laser Doppler electrophoresis using the Zetasizer Nano ZS. Samples were prepared as described in section 2.5.1.1 and measured in quintuplicate using the monomodal mode with 12 runs each and with a delay of 20 s between the runs. The viscosity was assumed to be 0.89 mPa s (at 25 °C). The Zetasizer software 6.30 was used for analysis applying Henry's equation in the Hückel model. The pH value was measured at room temperature by a glass electrode (Knick Portamess 911(X) pH combined with a pH sensor SE 103, Berlin, Germany).

2.5.3 Ascorbic acid reduction assay

The protective properties of the NC shell against reduction of the incorporated trityl radical were investigated with an ascorbic acid reduction assay based on the one described by Rübe et al. [150]. NC dispersions containing a solution of dTAM-dEE in MCT ($c = 1$ mM) were concentrated to one-half of the initial volume by evaporation under reduced pressure at a maximum temperature of 30 °C. One part of the dispersions was mixed (1:1, V/V) with PBS 7.4 and the other one with a 2.5 mM solution of ascorbic acid in PBS 7.4. In the latter case, EPR spectra were recorded for 4 h at X-band. The EPR intensity of the spectrum measured in buffer only was defined as the 100 % value; all others were calculated relatively.

For comparison, a solution of 4-hydroxy-2,2,6,6-tetramethylpiperidin-1-oxyl benzoate (TEMPOL benzoate, TB) in PBS 7.4 ($c = 1$ mM) as well as NCs containing TB dissolved in MCT ($c = 1$ mM) were prepared. TB containing samples were measured using the

same method, excepting the following measurement settings: microwave power, $<10\,\text{mW}$; sweep, $4.7\,\text{mT}$. Here, a first-derivative Gaussian function was fitted to the low-field peak and integrated twice to obtain the signal intensity.

2.6 Physicochemical characterization of MPs

2.6.1 Particle size and morphology

2.6.1.1 Static light scattering (SLS)

The size of the MPs was determined by SLS, also known as laser diffraction, using a Mastersizer 2000 S with a Hydro 2000 S automatic dispersion unit (Malvern Instruments). An aliquot of each batch of MPs was dispersed in water $(10\,\text{mg}_{(\text{PVAc})}/\text{ml})$ by vortexing and the use of an ultrasonic bath. The samples were measured for $20\,\text{s}$ with $20\,000$ measurement snaps under ambient conditions with purified water as diluent.

Measurements were conducted five times with a delay of $120\,\text{s}$ to ensure the data did not show any drifts. However, despite careful sample preparation prior to the measurements, sometimes there was a drift towards smaller particle sizes from run to run, which may be ascribed to an ongoing desagglomeration of the MPs. Sedimentation was very unlikely since the measurement unit was vigorously stirred all the time. Hence, the last run seemed to reflect rather realistic values. The maximum relative error due to drifts was $2\,\%$.

The data were analyzed by use of the Application software 5.6 provided by Malvern Instruments. Unfortunately, the optical properties of the MPs were unknown. Therefore, in pre-tests, results of the Fraunhofer approximation were compared to those calculated by Mie theory using optical parameters, which could only be estimated. Among others, the properties of chrome oxide green (CrO_3, refractive index 2.52, absorption 0.1, as implemented in the software) were tested as LiNc-BuO is a green colored substance, too. Since the maximum relative deviation was only $2\,\%$, which was negligible for the present application of the MPs, the Fraunhofer approximation was considered as sufficient and further used for data evaluation.

2.6.1.2 Light and fluorescence microscopy

The MPs were observed using a transmitted-light microscope (Axiolab) with mounted camera (Olympus UC30 digital camera) operated by Olympus Stream Motion 1.7 software (Olympus) to obtain information about their shape and the distribution of the spin probe crystals in the polymer. Fluorescence microscopic images were taken with a Leica DM4000B transmitted-light microscope (Leica Microsystems, Wetzlar, Germany) equip-

ped with a metal-halide lamp (PhotoFluor® II NIR, 89 North, Burlington, USA) and a Nuance® EX multispectral imaging system and a mounted camera with CCD chip (ICX285, Sony, Tokio, Japan). The system was operated and images were processed by Nuance® version 3.0.2 software (PerkinElmer, Waltham, USA). The blue filter set (excitation filter: 450 nm to 490 nm, emission filter: 515 nm cut-on, longpass) was used.

2.6.2 Crystal load and encapsulation efficiency

The final concentration of LiNc-BuO inside the MPs (crystal load) and the encapsulation efficiency were determined by means of UV/Vis and EPR spectroscopy. The encapsulation efficiency was calculated as the ratio of the actual and theoretical spin probe contents.

2.6.2.1 Quantification by UV/Vis spectroscopy

Aliquots of each MP batch were dissolved in THF (theoretical LiNc-BuO concentration of 25 µg/ml). UV/Vis spectra were recorded in 1 cm quartz cuvettes using a Spekol 1200 UV/Vis spectrometer (Analytik Jena, Jena, Germany). THF was used as blank. For calibration, uncoated LiNc-BuO crystals were dissolved in THF in a concentration range of 5 µg/ml to 40 µg/ml and analyzed by UV/Vis spectroscopy using the same settings ($n = 4$). To calculate the actual spin probe content, the absorbance of each sample at 449 nm was compared to the calibration curve (see appendix, figure A.2).

2.6.2.2 Quantification by EPR spectroscopy

An accurately weighted amount of dry MPs, which theoretically contained 1 mg LiNc-BuO, was measured at L-band. The samples were carefully positioned in the center of the re-entrant resonator. However, to avoid deviations from inaccurate positioning, measurements were performed again after repositioning ($n = 4$). EPR signal intensities were compared to a calibration curve obtained from dry uncoated LiNc-BuO crystals in the range of 0.25 mg to 2 mg following the same procedure (see appendix, figure A.2).

2.6.3 Storage stability

Aliquots of MPs (6 mg) were stored under various conditions, which are listed in table 2.5 (section 2.2.2.4). The samples were measured by EPR spectroscopy at L-band on the day of preparation as well as up to 3 months later.

2.6.4 Pilot study on sterilization

MPs with and without incorporated LiNc-BuO as well as pure PVAc powder (each in triplicate) were separately filled into glass vials and exposed to electron beam (β^-) radiation in a linear electron accelerator (MB10-30MP, Mevex Corp., Stittsville, Canada) at 10 MeV. Irradiation was performed in air under ambient conditions up to a total dose of 25 kGy. Sterility of the irradiated samples was verified by use of *Bacillus pumilus*. It is referred to the Doctoral thesis of Christin Zlomke (Prof. Dr. Karsten Mäder, Halle, Germany) for further details. Before and after sterilization, the MPs were analyzed by EPR spectroscopy, SLS, DSC, and the molar mass of PVAc was determined.

2.6.4.1 Gel permeation chromatography (GPC)

The molar mass (M_w) of PVAc was gathered by GPC. Solutions of MPs or PVAc powder in DMF (1 mg/ml, each in triplicate) were pre-filtered using PTFE filters (pore size 0.45 µm). 100 µl were analyzed in a Viscotek GPCmax VE 2001 equipped with a Viscotek VE 3580 refractive index detector (Malvern Instruments) using a GRAM analytical column (300 mm · 8 mm, porosity 100 nm, particle size 10 µm, PSS Polymer Standards Service, Mainz, Germany). Samples were eluted in DMF with 10 mM lithium bromide at a flow rate of 1 ml/min and 60 °C. OmniSEC software (Malvern Instruments) was used to process the data. Calibration was performed using poly(methacrylic acid methyl ester) (PMMA) molecular weight standards.

2.6.4.2 DSC

The thermal behaviour of pure PVAc powder and MPs was investigated by DSC (DSC 200, Netzsch). Dry powder/MPs (2 mg to 5 mg) were measured in sample aluminium pans against an empty pan according to the following scheme: First, the samples were heated from 10 °C to 80 °C at 10 K/min, subsequently, the samples were cooled from 80 °C to 0 °C at −10 K/min, and finally, the samples were again heated using the same parameters.

2.7 *In vitro* evaluation and *in vivo* application of MPs

The experiments described in this section were conducted in close collaboration with Daniel Gündel (Prof. Dr. Oliver Thews, Martin-Luther-Universität Halle-Wittenberg, Halle (Saale), Germany) and published cooperatively [151].

2.7.1 Cell culture

The subline AT1 was grown in RPMI-1640 medium supplemented with 10% fetal calf serum at $37\,°C$ under a humidified 5% CO_2 atmosphere and subcultivated twice per week. W256 cells were grown as a suspension in RPMI-1640 medium supplemented with $20\,mM$ HEPES, $20\,mM$ $NaHCO_3$, $10\,mM$ L-glutamine, and 10% fetal calf serum.

2.7.2 Cytotoxicity assays

2.7.2.1 Caspase 3 assay

To assess the induction of apoptosis (cell death with intact cell membrane) by the MPs, the relative caspase 3 activity normalized to untreated control cells was determined. Cells were seeded in 24 well plates (1×10^6 cells per well), and exposed either to MPs or uncoated LiNc-BuO crystals, dispersed in RPMI-1640 medium, for $4\,h$ and $8\,h$ at $37\,°C$. In accordance to the manufacturer's instructions, cells were incubated with $200\,µl$ lysis buffer for $20\,min$ on ice, harvested, and centrifuged at $16\,000\,g$ for $10\,min$ at $4\,°C$. Lysis buffer contained $10\,mM$ TRIS-HCl, $100\,mM$ NaCl, $1\,mM$ EDTA, and 0.01% (v/v) Triton® X-100. $60\,µl$ of the supernatant were incubated with $40\,µM$ caspase 3 substrate IV, and the fluorescence kinetic of the cleaved product, 7-amino-4-trifluoromethylcoumarin, was recorded for $30\,min$ at $400\,nm$ excitation and $505\,nm$ emission wavelength using a multiwell fluorescence reader (Infinite, Tecan Group, Männedorf, Switzerland). Cleaved 7-amino-4-trifluoromethylcoumarin was quantified by a calibration curve using known concentrations. All measurements were normalized with respect to a BSA standard curve using a bicinchoninic acid assay.

2.7.2.2 Lactate dehydrogenase (LDH) assay

Necrosis formation (cell death with disruption of the cell membrane integrity) was quantified by assessment of LDH release from cells by determination of the activity of LDH in the incubation medium and cell lysate normalized to untreated control cells. Again, cells were seeded in 24 well plates (1×10^6 cells per well), and exposed either to MPs or uncoated LiNc-BuO crystals, dispersed in RPMI-1640 medium, for $4\,h$ and $8\,h$ at $37\,°C$. Reaction buffer contained $0.19\,M$ NADH and $0.84\,M$ sodium pyruvate in HEPES-Ringer solution adjusted to pH 7.4. HEPES-Ringer solution contained $24\,mM$ $NaHCO_3$, $0.8\,mM$ Na_2HPO_4 x $2\,H_2O$, $0.2\,mM$ NaH_2PO_4 x $2\,H_2O$, $86.5\,mM$ NaCl, $5.4\,mM$ KCl, $1.2\,mM$ $CaCl_2$, $0.8\,mM$ $MgCl_2$, $20\,mM$ HEPES, and $11\,mM$ glucose. The substrate cleavage kinetic was measured at $334\,nm$ (every $20\,s$ for $40\,min$ at $37\,°C$) in the multiwell fluorescence reader.

2.7.3 *In vivo* experiments

2.7.3.1 *In vivo* stability

To investigate the stability of the oxygen response *in vivo*, MPs were implanted into four female and four male SKH1-Hr^{hr} mice and the tissue oxygenation was assessed EPR spectroscopically under normoxic conditions (20.9 % O_2) as well as after 10 min of inspiratory hyperoxia (carbogen, 95 % O_2 and 5 %CO_2, delivered through a nose cone) over up to six months. Therefore, about 10 mg/200 µl MPs were implanted subcutanously into the right flank as well as 10 mg/20 µl intramuscularly into left thigh muscle. For EPR measurements, the animals were anesthetized intraperitoneally by injection of a ketamnine/xylazine mixture and placed in supine position on a heated operating pad.

2.7.3.2 *In vivo* assessment of tissue oxygenation

Animal care and tumor implantation
Solid W256 and AT1 tumors were heterotopically induced by injection of cell suspension (4×10^7 cells/0.4 ml 0.9 % NaCl) with or without about 10 mg MPs subcutaneously into the dorsum of the hind foot. W256 cells were implanted in male Wistar rats, AT1 cells in male Copenhagen rats. Tumors grew as flat, spherical segments and replaced the subcutis and corium completely. Tumor volumes were determined by measuring the length (l), wide (w) and height (h) with a caliper and using an ellipsoid approximation with the formula: $V = l \cdot w \cdot h \cdot \pi \div 6$. Tumors were investigated when they reached a volume of 0.8 ml to 1.8 ml after tumor cell inoculation.

Oxygen measurements
When tumors were grown to the targeted volume, the animals were subjected to either EPR spectroscopy or invasive fluoro-optical measurements (Oxylite). Animals were anesthetized intraperitoneally with pentobarbital and placed in supine position on a heated operating pad. They breathed spontaneously room air, hypoxic and hyperoxic gases through a nose cone in four subsequent periods according to following scheme: 10 min normoxia (air, 20.9 % O_2), 10 min hypoxia (8 % O_2 in N_2), 20 min hyperoxia (100 % O_2) and again 20 min normoxia. For comparison of the results of both oximetry techniques, each period was divided into either three or five shorter time intervals in which all obtained values of pO_2 of each tumor were averaged.

EPR oximetry
In vivo EPR oximetry measurements were conducted using an L-band EPR spectrometer equipped with a surface coil (section 2.4.1). The surface coil was placed directly on the

skin above the tumor without any pressure allowing unhindered blood flow. Subsequent measurements were performed at the same position to allow relative comparisons.

Fluoro-optical measurements

Invasive oxygen measurements were performed with catheterized (A. carotis and V. jugularis) animals. Intratumoral pO_2 was measured with a fluoro-optical catheter, which was placed in the center of the tumor and continuously monitored with a Tissue Oxygenation Monitor (Oxylite 2000, Oxford Optronics, Oxford, UK). In parallel, the relative erythrocyte flow through the tissue was assessed by laser Doppler-flowmetry. Therefore, two probes where placed in each tumor and coupled to a Microvascular Perfusion Monitor (Oxyflo 4000, Oxford Optronics, Oxford, UK). Oximetry and laser Doppler flowmetry devices were coupled to PowerLab devices. Data was monitored and recorded with LabChart7 software (ADInstruments Pty, Bella Vista, Australia). Intravasal arterial blood pressure was monitored by a pressure dome coupled to a bridged amplifier. Arterial pO_2 was measured with an ABL5 blood gas analyzer (Radiometer, Willich, Germany) from arterial blood samples.

2.7.4 *Ex vivo* investigations

After the tumors had been surgically removed, the tissue was shock frozen in liquid nitrogen, and stored at $-80\,°C$ until further processing. Cryosectioned slices were transferred to a microscopic slide and immediately heat shock inactivated on a hot plate ($54\,°C$ for $5\,min$). Slides were stored at $-20\,°C$ until further processing.

2.7.4.1 Immunohistochemical analysis

CD163 positive cells and vascular density

Tumor sections were fixed in ice cold acetone for $10\,min$, and then incubated either with mouse CD163 antibodies or with mouse CD31 antibodies to determine the vascular density. After primary antibody incubation at $4\,°C$ in a humidated chamber and three washing steps with PBS, tumor sections were incubated with a secondary fluorescein isothiocyanate coupled antibody for $2\,h$ at room temperature, followed by three washing steps. Slices were conserved utilizing fluorescence mounting medium.

Pimonidazole

Pimonidazole peptide adduct generation in hypoxic regions ($<10\,mmHg$) was analyzed similarly with a Hypoxyprobe^{TM}-1 Omni Kit following user's guide. For that, animals were purged with either $8\,\%$ or $100\,\%$ oxygen for $90\,min$ in a chamber and (during EPR measurements) through a nose cone, respectively. After $30\,min$, pimonidazole was injected

(60 mg/kg bodyweight, intraperitoneal), thus, it was allowed to distribute for 60 min. EPR measurements were conducted under ongoing purging just before the animals were sacrificed and the tumors were resected and deep frozen.

Fluorescence microscopy
Images of cryosectioned slices were taken at 4 x magnification with a Biozero BZ-9000 (Keyence Deutschland, Neu-Isenburg, Germany) at an extinction of 470 nm/40 nm and an emission at 535 nm/50 nm. Single images were merged for analyzing the overall tumor area by use of the ImageJ software (U.S. National Institutes of Health (NIH), Bethesda, USA). Background fluorescence was corrected by subtraction of fluorescence generated by tumor sections, which had only been incubated with secondary antibody.

2.7.4.2 MP distribution

After cryosectioning, 28 brightfield images (8 x magnification) were taken, all with same adjustments utilizing a Keyence Biozero microscope and merged by provided microscope software. MP distribution analysis was done by ImageJ software with a custom particle counting macro analyzing 40 to 163 $1\,\mu m^2$ areas of $20\,\mu m$ tumor sections, leading to $0.02\,\mu m^3$ volume per analyzed area.

2.8 Statistical analysis

Unless stated otherwise, statistical differences between two groups of unpaired data were assessed by two-tailed Student's t test with a significance level of $\alpha = 0.05$ in Excel (Microsoft, Redmond, USA). Usually, data are presented as median and range if $n = 3$, and as mean $\pm$ standard deviation (SD) if n > 3, respectively.

2.9 Software

This work was written in LaTeX (TeXnicCenter and MiKTeX). Literature was managed in Mendeley (Mendeley Ltd., London, UK), citations were added via BibTeX. Graphs were generated in OriginPro 9.0.0. Chemical formulas were drawn in ChemBioDraw Ultra 12.0. Graphics and images were created and/or edited in CorelDRAW X8 (Corel, Ottawa, Kanada) or Adobe Photoshop Elements 2.0 (Adobe Systems, San Jose, USA).

3 Results and discussion

Basically, EPR oximetry is feasible with soluble spin probes as well as particulate radicals. Both approaches have been explored in this work. The available spin probes had to be investigated regarding their properties and applicability as oxygen sensing materials. For the most promising spin probes, suitable formulations ought to be developed, characterized, and utilized *in vitro* and *in vivo*. This chapter is divided into two parts: The first part deals with soluble trityl radicals, the second with the particulate material LiNc-BuO.

Part I: Trityl radicals

The following part was elaborated in cooperation with Prof. Dr. Peter Imming and his group and is based on the article "Synthesis, characterization, and nanoencapsulation of tetrathiatriarylmethyl and tetrachlorotriarylmethyl (trityl) radical derivatives – A study to advance their applicability as in vivo EPR oxygen sensors" by Frank et al. [143]. Further experiments with trityl radicals can be found in the second mutual publication "Synthesis and EPR-spectroscopic characterization of the perchlorotriarylmethyl tricarboxylic acid radical (PTMTC) and its ^{13}C labelled analogue (13C-PTMTC)" by Elewa et al. [152].

Trityl radicals belong to the class of soluble EPR spin probes. Their spectral line width is directly proportional to c_{O_2} in the solvent, rendering them suitable for EPR oximetry [20, 81, 116]. According to Henry's law, this concentration is in turn directly proportional to the pO_2 in the gas above the solution. Thus, after calibration, not only c_{O_2}, but also indirectly the pO_2 can be determined. The following sections concern the EPR spectroscopical analysis and oxygen calibration of several hydrophilic and lipophilic trityl radicals in order to evaluate their applicability as oxygen sensitive spin probes. Another topic is the nanoencapsulation, which was expected to be a promising formulation strategy for lipophilic soluble probes.

3.1 EPR spectroscopic characterization

There is one major concern when soluble radicals are used for EPR oximetric measurements: Other environmental parameters, for instance, the viscosity and pH value of the solvent might affect the EPR signal as well. So far, there is only little knowledge about the specificity for oxygen. Accordingly, this issue is addressed in this section. Hydrophilic trityl radicals were examined in aqueous media and lipophilic probes in oily solution.

Note that, according to Yong *et al.*, the relaxation times of trityl radicals can be so long that accurate measurements of the line width might be aggravated by magnet inhomogeneities and spectrometer instabilities [68]. The microwave power has to be low to avoid saturation. Further, the traditional 100 kHz magnetic field modulation might lead to undesired line broadening [68]. To overcome this problem with line widths <7.8 µT, the oscillating field can be modulated at 10 kHz only, or, if not implemented, the spectrum can be measured 90° phase shifted. Thereby, the two modulation side bands with a distance of 7.2 µT, having the same line width as the main line, are gathered.

3.1.1 Hydrophilic trityl radicals

Since hydrophilic trityl radicals are soluble in aqueous biological samples, such as blood or other tissues, they can be employed directly and do not necessarily have to be formulated. Representatively, the hydrophilic radical dTAM was studied under several conditions to mimic environments in biological samples or *in vivo*.

3.1.1.1 Influence of ionic strength, osmolarity, and pH value

To investigate the impact of ionic strength and pH value on the apparent EPR line widths, solutions of dTAM in PB 6.2 and PB 7.4 as well as PBS 6.2 and 7.4 were examined under aerated ($\approx 20.9\,\%$ O_2 or a pO_2 of 155 mmHg in the gas above the solution) and deoxygenated ($\approx 0\,\%$ O_2 or a pO_2 of 0 mmHg in the gas above the solution) conditions. PBS buffers have ionic strengths and osmolarities which are similar to physiological values, whereas PB buffers have lower ionic strengths/osmolarities (table 2.3). The pH values were chosen referring to the pertinent range mainly occurring in human tissues, namely, 7.0–7.4 in normal tissues and 6.2–7.4 in tumors [153].

Aerated solutions of dTAM in the different buffer systems showed similar line widths ($\Delta B_{PP} = 13.7\,\mu T$) as well as similar EPR line width narrowing ($\Delta B_{PP} = 3.1\,\mu T$) after deoxygenation of the samples (figure 3.1). As mentioned above, PBS buffers have a higher ionic strength than PB buffers. The oxygen solubility of aqueous solutions decreases with increasing salt content [154]. Consequently, in aerated solutions, the c_{O_2} should be lower
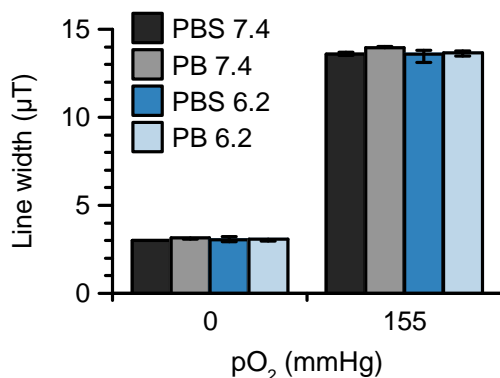
Figure 3.1: Apparent EPR line widths of dTAM ($c = 50\,\mu M$) in PBS 6.2 and 7.4 as well as PB 6.2 and 7.4 under anoxic and aerated conditions ($n = 3$).

in PBS buffers than in PB buffers. But obviously, the effect is too small to be reflected in a significant change of the EPR line width. The pK_a of the undeuterated derivative TAM was determined to be approximately 4 [69]. Due to the low solubility of the protonated form, TAM was found to precipitate at pH values lower than approximately 4, which limits its application in acidic media [69]. However, in the pH range studied, both radicals, dTAM and TAM, should mainly exist in their ionized form, without any impact on their EPR properties. Concluding, within the investigated physiologically relevant limits of ionic strength/osmolarity and pH value, there was a negligible effect of these parameters on the apparent EPR line width of dTAM.

3.1.1.2 Impact of viscosity

To study the effect of viscosity on the apparent EPR line width of hydrophilic trityl radicals, dTAM was dissolved in glycerol-water mixtures (0 % to 90 % glycerol in water, m/m). In absolute glycerol, dTAM was practically insoluble according to Ph.Eur. [147].

Under aerobic conditions, between 0 % and 60 % (m/m) glycerol content, a decrease in the EPR line width was detected, which was followed by a sharp increase (figure 3.2a). To explain these results, two aspects have to be considered. First, at low glycerol contents, the viscosity of glycerol-water mixtures is only slightly increasing with glycerol content, whereas above 50 % (m/m) of glycerol, there is a sharp rise [155]. Additionally, the oxygen solubility changes: With increasing percentage of glycerol, oxygen solubility and, hence, c_{O_2} are decreased [156]. Both effects determine the EPR line width: Up to 50 % (m/m) of glycerol, it was mainly affected by the decreasing oxygen content, overruling the effect of viscosity. Above 50 % (m/m), conditions change as almost no oxygen is dissolved anymore, but viscosity is increasing drastically. When the measurements were conducted under anoxic conditions, the line width changed as predicted from the viscosity of the solutions (figure 3.2a). Up to 50 % (m/m) of glycerol, the EPR line width was slightly
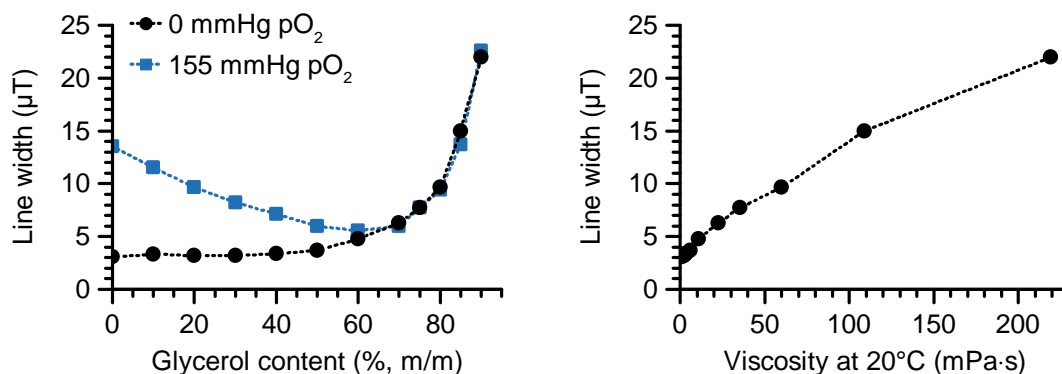
(a) Change in the line width on different glycerol-water mixtures under anoxic and aerated conditions.

(b) Viscosity dependence of the line width in deoxygenated solutions.

Figure 3.2: Impact of viscosity of different glycerol-water mixtures on the apparent EPR line width of dTAM ($c = 50\,\mu M$).

increasing. A sharp increase followed which was similar to aerated solutions and, therefore, attributed to the strong increase of viscosity.

In a low viscosity medium, trityl radicals rotate rapidly, which averages any anisotropy in a spectrum and leads to narrow lines, whereas in high viscous environment, the rotational motion is slowed and anisotropy can only incompletely be averaged [60]. Yong *et al.* already stated that the line width of dTAM and TAM exhibited a modest dependence on viscosity. In water, T_1 and T_2 were similar indicating that the trityl was close to the fast tumbling limit. They showed that T_1 is slightly increasing with viscosity, which might be due to a small contribution from trityl–trityl collisions in water, which decreases as the solution viscosity increases. However, T_2 was significantly smaller than T_1, thereby causing broader EPR lines. For dTAM, they found a viscosity dependence of $0.09\,\mu T/(mPa\,s)$ on the apparent line width at 250 MHz [68]. The results at hand were comparable to these findings. However, the relationship between the viscosity and the apparent line width was not completely linear (figure 3.2b).

Compared to the effect of oxygen (section 3.2), the impact of viscosity on the EPR line width in glycerol-water mixtures up to 50 % (m/m) of glycerol was negligible. These results are important with regard to biomedical applications as blood has a dynamic viscosity of $3\,mPa\,s$ to $4\,mPa\,s$ at $37\,°C$ [157], which is only reached at 40 % (m/m) of glycerol in water at $20\,°C$ [155]. Thus, provided that there is no specific interaction with biological structures, viscosity by itself should have hardly any effect on the EPR line width when using the radicals dissolved in plasma or blood.

3.1.2 Lipophilic trityl radicals

The triesters of the trityl radicals investigated in this work proved to be very lipophilic. When these radicals were distributed between octanol and water or MCT and PBS 7.4 for 2 h at 37 °C, the EPR signal resided in the lipophilic solvent (octanol or MCT) exclusively. Hence, these trityl radicals were further analyzed in oily solution, in particular, in MCT and IPM, under aerated as well as anoxic conditions.

The estimated EPR line widths are listed in table 3.1. As predicted from the higher viscosity, the EPR lines under anoxic conditions were broader in MCT. In air, however, the lines were broader in IPM. This is attributed to the higher oxygen solubility and correspondingly higher oxygen content, overruling the effect of viscosity (section 3.2). Since the hfs pattern under anoxic conditions was much better resolved in the less viscous IPM, only the EPR spectra in IPM are shown in figure 3.3.

Table 3.1: EPR line widths of different lipophilic trityl triesters dissolved in MCT and IPM ($c = 1\,\mathrm{mM}$) in aerated as well as anoxic conditions (n.m. = not measured).

Radical	MCT		IPM	
	EPR line width (µT) at		EPR line width (µT) at	
	0 mmHg pO_2	155 mmHg pO_2	0 mmHg pO_2	155 mmHg pO_2
TAM-EE	15 (7 hfs lines)	57	10 (7 hfs lines)	94
TAM-tBE	n.m.	n.m.	9	88
dTAM-EE	10 (7 hfs lines)	53	7 (7 hfs lines)	91
dTAM-dEE	15	44	12	83
Cl-TAM-EE	51	82	23	98
Cl-TAM-tBE	53	90	23	98

Under anaerobic conditions, the signal of the triethyl ester of the deuterated trityl (dTAM-EE) displayed superhyperfine coupling with the six equivalent protons of the three methylene groups of the ethyl ester moieties resulting in seven equidistant lines with relative intensities of 1:6:15:20:15:6:1, following Pascal's triangle, and a coupling constant of $a = 11.3\,\mathrm{µT}$. The same ester but with protonated instead of deuterated methyl groups in the ketal moiety (TAM-EE) resonated with slightly broader EPR line widths compared to dTAM-EE. The additional superhyperfine coupling with the protons of the methyl groups affected the signal pattern in deoxygenated solutions. In MCT, only the envelope of the coupling pattern was visible. Deuterium with a nuclear spin of 1, of course, also couples
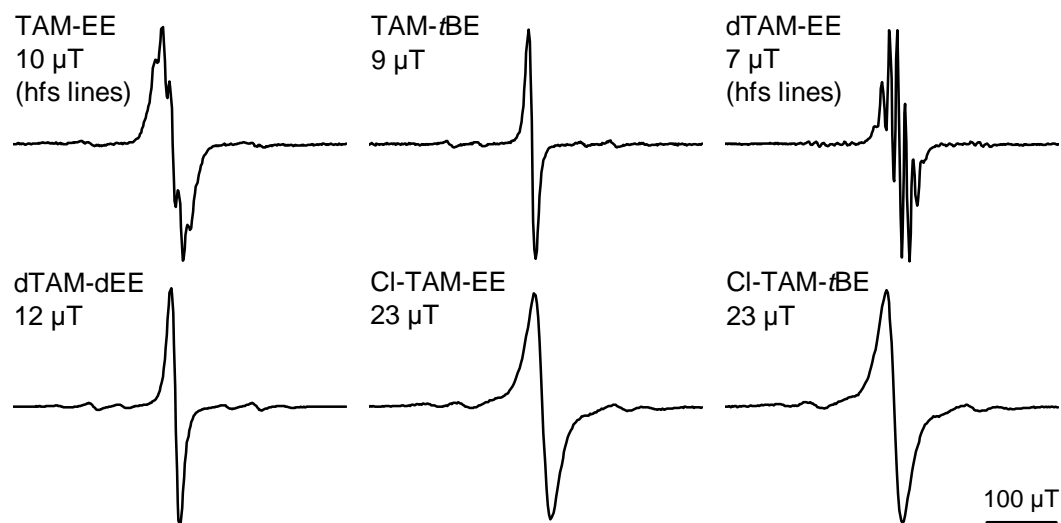
Figure 3.3: EPR spectra of different lipophilic trityl triesters and their apparent line widths under anoxic conditions in IPM ($c = 1\,\text{mM}$). The small side bands caused by hyperfine couplings with ^{13}C were not used in this analysis.

with the electron, but the coupling constant is much smaller compared to the coupling constant of hydrogen [158].

The tri-*tert*-butyl ester of the nondeuterated trityl (TAM-*t*BE) displayed the narrowest single EPR line of all lipophilic esters investigated. As expected, due to the small unresolved hfs with the protons of the *tert*-butyl and methyl ketal moieties, the line width in anoxic IPM was slightly broader when compared to the hfs lines of dTAM-EE. Fully deuterated ethyl ester and methyl ketal groups (dTAM-dEE) also led to an exceptionally narrow single line. Compared to TAM-*t*BE and dTAM-EE, the line was slightly broader in anoxic solutions caused by the unresolved coupling with deuterium nuclei. However, because radical dTAM-dEE had a better synthetic accessibility than TAM-*t*BE, it was chosen for the following oxygen calibration measurements and encapsulation investigations.

Due to the chlorine splitting, tetrachloro-TAM triesters generally had broader EPR lines than tetrathia-TAM derivatives. The tri-*tert*-butyl ester (Cl-TAM-*t*BE) displayed the same line width as the triethyl ester (Cl-TAM-EE) in IPM, while in MCT, the line widths were slightly broader. The extremely narrow anoxic line width of these radicals in IPM is remarkable. Only in deoxygenated DMSO (viscosity $2\,\text{mPa}\,\text{s}$ at $20\,^{\circ}\text{C}$), a line width $<30\,\mu\text{T}$ (approximately $28\,\mu\text{T}$) was reported for tetrachloro-TAM radicals in the literature [81]. When dissolved in deoxygenated hexafluorobenzene, the line width of Cl-TAM-EE was approximately $38\,\mu\text{T}$, although the viscosity is only $1.2\,\text{mPa}\,\text{s}$ at $20\,^{\circ}\text{C}$.

3.2 Oxygen calibration

Besides specificity, linearity and sensitivity are important aspects in order to evaluate the suitability of trityl radicals as oxygen sensors. It should be noted that, despite soluble radicals respond on the c_{O_2}, values are given in relation to the pO_2 in the gas above the solution for better comparability. As mentioned before, both quantities are linearly related to each other. For atmospheric pressure and *in vivo* applications, only the data between approximately 0 mmHg and 155 mmHg pO_2 are of interest and, hence, investigated here. In this range, the relationship between the EPR line width and the oxygen concentration should be linear. The slope of the calibration curves determines the oxygen sensitivity and should be as high as possible. Splitting in spectra of some trityl radicals may lead to overlapping and redundant information, lower SNR, and multiline spectra can be complicated to deconvolute. Therefore, trityl radicals with only one line were regarded superior for oximetry. Thus, solutions of dTAM and TAM in PBS 7.4 as well as dTAM-dEE, Cl-TAM-EE, and Cl-TAM-*t*BE in MCT and IPM were measured EPR spectroscopically under various defined oxygen contents. Oxygen calibration curves are presented in figure 3.4 and the calculated oxygen sensitivities in table 3.2.

(a) Hydrophilic trityl radicals dissolved in PBS 7.4 ($c = 50\,\mu M$).

(b) Lipophilic triesters dissolved in MCT (black-grey, solid lines) and IPM (blue, dashed lines) ($c = 1\,mM$).
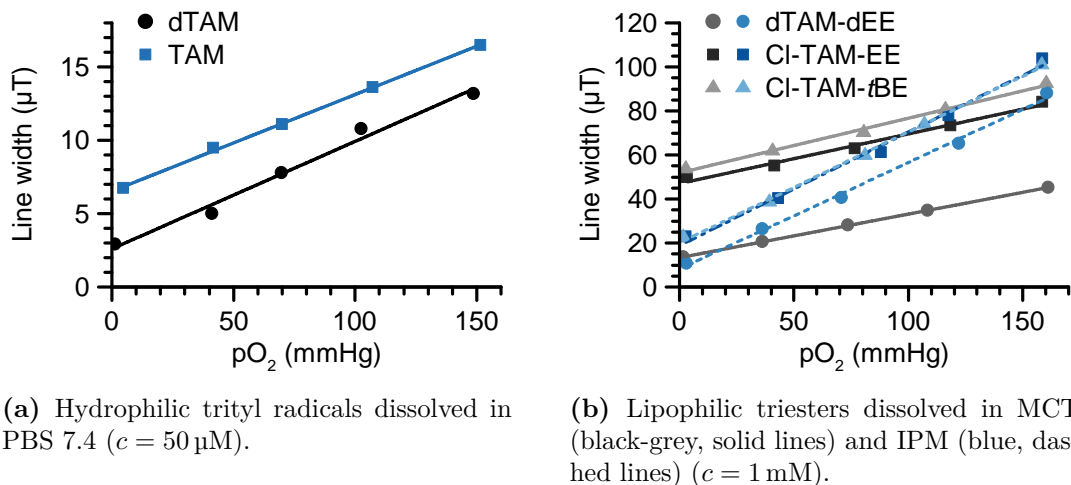
Figure 3.4: Oxygen calibration curves of different trityl radicals (mean, $n = 3$, lines: linear regressions). Corresponding oxygen sensitivities are reported in table 3.2.

Solutions of the hydrophilic radicals (dTAM and TAM) in PBS 7.4 showed a linear relationship between the EPR line width and the oxygen concentration. As expected, dTAM had a narrower line width ($\Delta B_{PP} = 13.6\,\mu T$ at 155 mmHg pO_2) than its undeuterated analogue TAM ($\Delta B_{PP} = 16.5\,\mu T$ at 155 mmHg pO_2), which was attributed to averaging

Table 3.2: Mean oxygen sensitivities of hydrophilic trityl radicals in PBS 7.4 ($c = 50\,\mu M$) and lipophilic compounds in MCT and IPM ($c = 1\,mM$) reported in µT/mmHg ($n = 3$).

Radical	PBS 7.4	MCT	IPM
dTAM	0.073	n.m.	n.m.
TAM	0.066	n.m.	n.m.
dTAM-dEE	n.m.	0.20	0.48
Cl-TAM-EE	n.m.	0.23	0.52
Cl-TAM-tBE	n.m.	0.25	0.51

of larger hyperfine anisotropy for the undeuterated derivative. However, the oxygen sensitivity was comparable ($\approx 0.07\,\mu T/mmHg$). Similar line broadenings had been reported in the literature: A sensitivity of $0.084\,\mu T/mmHg$ was found for TAM in buffer [69] and $36.9\,\mu T/mM$ oxygen for a related compound (deuterated hydroxy trityl radical) in water [116]. Under ambient conditions, this is equal to $0.067\,\mu T/mmHg$.

As mentioned before, the EPR lines of soluble spin probes are broadened by Heisenberg exchange between the probes and molecular oxygen in solution. According to the Smoluchowski equation, the higher c_{O_2}, the higher the bimolecular collision rate. Albeit, in water, the solubility of oxygen is low: The oxygen content in water is only approximately $0.6\,\%$ (v/v) at $22\,°C$ and $0.213\,bar\ pO_2$ [154, 159]. Hence, c_{O_2} increases only slightly with increasing pO_2. As a consequence, there is only small line broadening, a physicochemical fact affecting any oxygen determination by soluble EPR spin probes in water which is rarely stated. Oxygen solubility in oils is generally higher than in water at a given temperature and pressure [160], such that c_{O_2} rises noticeably with increasing pO_2. Accordingly, the slopes were steeper than in water. The oxygen sensitivities of the lipophilic radicals were about $0.2\,\mu T/mmHg$ in MCT and $0.5\,\mu T/mmHg$ in IPM. By gas chromatography, oxygen contents of $2.2\,\%$ (v/v) in MCT and $2.9\,\%$ (v/v) in IPM at $22\,°C$ and $0.213\,bar\ pO_2$ were determined, both markedly above the oxygen content of water. However, a closer look at the absolute values revealed that the different oxygen sensitivities determined by EPR could not solely be explained by different oxygen solubilities. Additionally, different polarity and viscosity of the oils might have contributed.

Remarkably, chemically different radicals, *e.g.*, dTAM-dEE and Cl-TAM-EE, had similar oxygen sensitivities when dissolved in the same solvent. Smaller deviations might be attributed to resolved or unresolved hfs. Thus, obviously, the oxygen sensitivity was rather more affected by the nature of the solvent than the properties of the radical. However, the y intercepts, *i.e.*, line widths under anoxic conditions, were quite different for different radicals as already discussed in section 3.1.2.

Of all investigated spin probes and solvents, a solution of radical dTAM-dEE in IPM was considered best for oxygen measurements: It had the steepest slope with the smallest y intercept. Hence, it combined both excellent oxygen sensitivity and a good SNR. An even higher oxygen sensitivity, as reported for perfluorocarbons [77, 129, 130], leads to lower SNRs (due to broader lines) in aerated solutions, and is therefore not necessarily in demand, only if a very high accuracy is needed for small changes in pO_2. The oxygen sensitivity in IPM is comparable with what had been reported for some particulate oxygen sensitive spin probes, such as LiPc ($0.61\,\mu T/mmHg$) [111] or LiNc-BuO ($0.45\,\mu T/mmHg$) [94], and, thus, very promising for future applications in the field of EPR oximetry as an alternative to particulate materials. Hence, it was used for incorporation into oily-core NCs (section 3.3).

3.3 Encapsulation of trityl radicals

In section 3.1.1, it was shown that to some extent the EPR properties of different water-soluble trityl radicals were independent of their environment, excepting the parameter of interest, *viz.*, oxygen. However, during *in vitro* or *in vivo* experiments, conditions can change unexpectedly. Therefore, it was assumed that formulations such as NCs might be a helpful approach. If dissolved in the oily core of NCs with an oxygen-permeable shell, lipophilic spin probes are located in a constant microenvironment, without being affected by changes of the outer milieu. Thereby, NCs can also be used in acidic conditions where hydrophilic trityl radicals would precipitate [69]. Moreover, the oxygen sensitivity is improved in comparison to hydrophilic trityl radicals, which are employed in aqueous solution (section 3.2). Besides, the biocompatibility can be improved. Therefore, oily solutions of the most promising lipophilic trityl triester, dTAM-dEE (section 3.2), were encapsulated into PVAc NCs to enhance its applicability as oxygen sensor. The following sections deal with the NC preparation and their characterization.

3.3.1 NC preparation

NCs with different concentrations (varying from $0.1\,\%$ to $2\,\%$) of PVAc (m/m) and MCT (v/w) in the organic phase were prepared. As a hydrophilic stabilizer, poloxamer 188 ($0.25\,\%$ (m/m) in the aqueous phase) was used, and acetone served as the organic solvent. In order to obtain the best SNR of the EPR spectra, the amount of oil inside the NCs needed to be high. On the other hand, the polymer shell surrounding the oily core should be as thin as possible since oxygen has to permeate through the shell. Therefore, NCs should have the lowest possible PVAc and highest possible oil contents. It was found that

a concentration of 0.2 % (m/m) PVAc and 1.4 % (v/w) MCT was optimal. In contrast to MCT, it was not possible to obtain stable NCs containing IPM using poloxamer 188. Therefore, other stabilizers were tested, and polysorbate 80 proved to be suitable. The best formulation contained 0.2 % (m/m) PVAc and 1.2 % IPM (v/w) in the organic phase and 0.2 % (m/m) polysorbate 80 in the aqueous phase.

3.3.2 Physicochemical characterization of the NCs

The size of the NCs was determined by two complementary light scattering techniques: DLS and NTA. Both methods relate Brownian motion of particles in dispersion to an equivalent hydrodynamic diameter. The movement velocity depends on their size. Brownian motion of the particles causes interference and, hence, time dependent fluctuations of light intensity scattered by the particles. These fluctuations are analyzed by DLS meaning that all particles are measured at the same time. In contrast, with NTA, the movement of the particles is tracked by use of a microscope and a high-speed camera on a particle-by-particle basis. Accordingly, DLS provides an intensity based particle size distribution, while NTA produces a number distribution. In polydisperse samples, DLS is biased towards larger particles as they scatter light more intensively than smaller particles. NTA can give more accurate distribution shapes. However, the results of NTA analysis are statistically less robust since data are collected from higher dilution and, thus, smaller portion of particles. If very large particles were present, they could reliably be detected by DLS. Both technologies were combined to benefit from their individual strengths.

Typical intensity weighted and number particle size distributions of MCT and IPM NCs are shown in figure 3.5. The mean hydrodynamic diameter obtained by DLS (z-average) typically was about 160 nm for IPM NCs and about 150 nm for MCT NCs. The size distributions were monomodal and monodisperse, indicated by a very low polydispersity index (PdI) <0.1. The samples were free of large aggregates. NTA confirmed that the size distributions were narrow. However, the mean diameters slightly differed. By NTA, the mean hydrodynamic diameters were 162 nm for IPM NCs and 166 nm for MCT NCs. These deviations might be attributed to minor batch-to-batch variations in the size.

The morphology and shell thickness of the NCs were investigated using cryo- and freeze-fracture-TEM. The capsules were spherical in shape; their size varied between approximately 50 nm to 150 nm [figure 3.6a]. The deviation from the DLS data might be explained by a particle selection, which usually occurs during sample preparation for cryo-TEM. Here, the DLS and NTA data are considered to represent particle size better. Further, the PVAc shell thickness was determined. Fractured NCs clearly showed a structure with core and shell [figure 3.6b]. The shell thickness was with approximately 8 nm very thin,

(a) Typical intensity weighted particle size distributions as obtained by DLS.

(b) Number size distributions as measured by NTA.
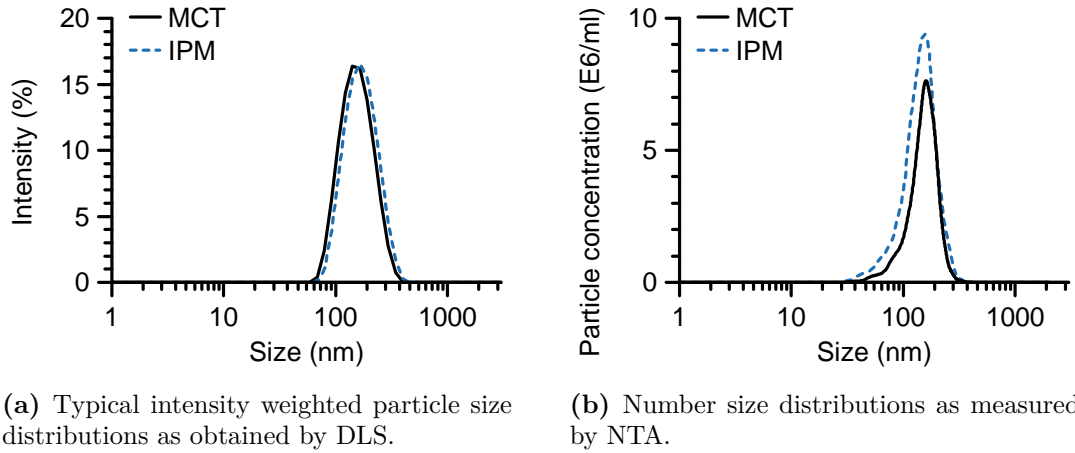
Figure 3.5: Hydrodynamic particle sizes of MCT and IPM NCs.
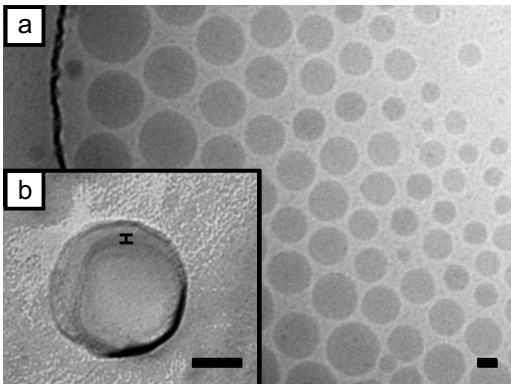
Figure 3.6: Morphology investigations of NCs by TEM. (a) Cryo-TEM image of MCT NCs, (b) TEM images of freeze-fractured replica of an IPM NC with an estimated shell thickness of about 8 nm (bar sizes: 50 nm).

which is in accordance to the literature, where a shell thickness of 10 nm had been found for poly(lactic-co-glycolic acid) (PLGA) NCs [161].

In order to examine the stability of the NCs, their size and ZP as well as the pH value of the dispersion were measured not only on the day of preparation but also up to three months of storage at 2 °C to 8 °C (figure 3.7). Whereas MCT NCs were stable over the whole measurement period, IPM NCs showed instabilities. The z-average as well as the PdI changed over time of storage. In particular, the increased PdI (from <0.1 to >0.2 after 30 days of storage) indicated aggregation. After 1 week of storage, creaming was observed for the IPM NCs but not for MCT NCs. The reason might be the lower density of IPM with about 850 kg/m^3 compared to MCT with a density of about 950 kg/m^3. The NCs were redispersible by gentle shaking. However, it is assumed that creaming is the reason why IPM NCs tended to aggregate more because of the spatial proximity of the particles. Hence, IPM was less suitable for the preparation of long-term stable NCs. These findings

(a) Size (z-average, diameter) and PdI of the NCs.

(b) ZP of the NCs and pH value of the dispersion.
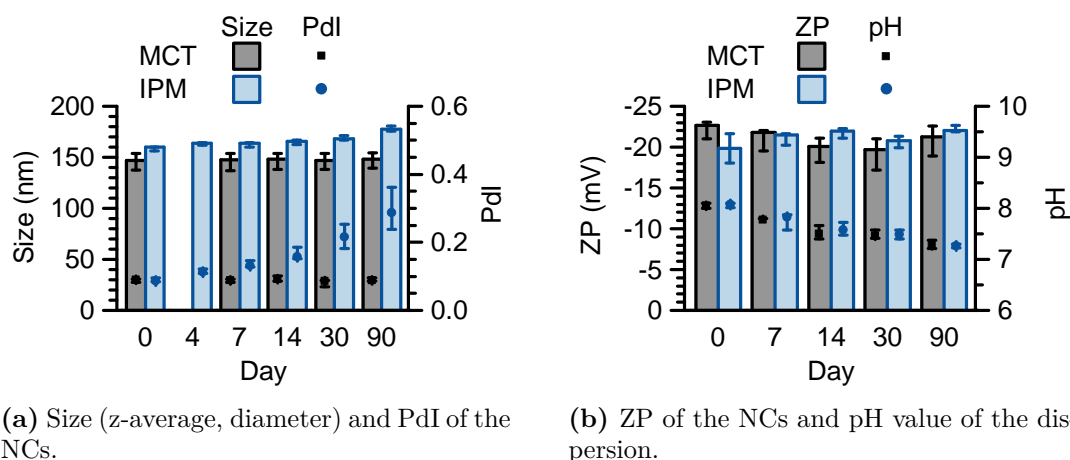
Figure 3.7: Change in characteristics of MCT and IPM NCs on duration of storage at 2 °C to 8 °C ($n = 3$).

are consistent with the literature [162]. The ZP, as measured in doubly distilled water by laser Doppler electrophoresis, was found to be $-19\,\text{mV}$ to $-23\,\text{mV}$, providing relatively good colloidal stability. However, it must be stated that due to the stabilizers used, the main stabilization mechanism probably was static repulsion. For both oils used, the ZP was stable over time of storage. The pH value of the dispersions was approximately 8 after preparation, and slightly decreased to approximately 7.3 after three months, which may have been due to a partial hydrolysis of PVAc and, therefore, release of acetic acid. However, the pH value was always in a physiologically well-tolerated range.

3.3.3 Oxygen response

The NCs had similar oxygen sensitivities as the unencapsulated solutions (figure 3.8a). Thus, the encapsulation of the spin probes did not alter their oxygen sensitive properties. Oxygen obviously diffuses through the polymer shell without any hindrance. The process was reversible (data not shown), meaning that no oxygen was accumulated inside the NCs. However, it must be stated that the signal intensity is not very satisfying (figure 3.8b), which is attributed to the overall small amount of oil encapsulated into the NCs.

3.3.4 Ascorbic acid reduction assay

Since the lipophilic triesters, such as dTAM-dEE, are uncharged, they may be less protected from reduction by negatively charged reductants since there is no electric repulsion [73, 114]. To investigate the stability of encapsulated radicals against reduction, an as-
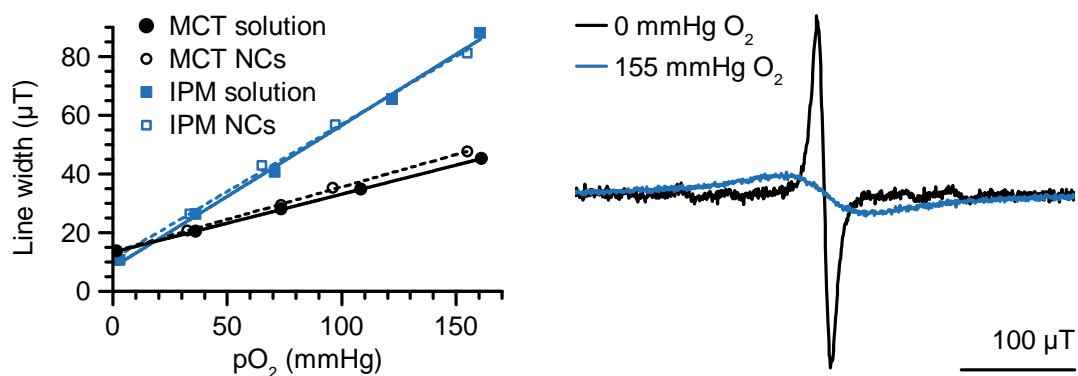
(a) Oxygen calibration curves. Mean oxygen sensitivities were $0.46\,\mu T/mmHg$ (IPM) and $0.22\,\mu T/mmHg$ (MCT) for the NCs compared to $0.48\,\mu T/mmHg$ (IPM) and $0.20\,\mu T/mmHg$ (MCT) for the unencapsulated solutions (mean, $n = 3$, lines: linear regressions).

(b) Corresponding EPR spectra of dTAM-dEE incorporated into IPM NCs under anoxic and aerated conditions.

Figure 3.8: Oxygen calibration of dTAM-dEE in oily solution ($c = 1\,mM$) both incorporated into NCs and unencapsulated.

corbic acid reduction assay was carried out. For that purpose, NCs containing solutions of either TB or dTAM-dEE in MCT were prepared. TB is a nitroxide with a log P of approximately 2 [163]. It was chosen for comparison because even though it is lipophilic enough for encapsulation, TB is still soluble in water. It is able to partly diffuse through the polymer shell and partition between the two phases. Once outside the NC, the paramagnetic nitroxide can be reduced by ascorbic acid into the diamagnetic hydroxylamine perceivable by a reduction of the signal intensity. As a positive control, a solution of TB in PBS 7.4 was used.

As expected, TB encapsulated in NCs was reduced by ascorbic acid (figure 3.9a). The EPR signal intensity diminished to about 11 % of the starting value within 240 min (figure 3.10). However, when compared to unencapsulated TB, the reduction rate was decreased considerably (half-life times: 40.2 min and 1.4 min). Comparable results had been found for PLGA NCs [150]. In contrast, dTAM-dEE seemed to stay shielded inside the NCs as it was not reduced by ascorbic acid after 240 min (figure 3.9b). These results proved that the capsule shell was capable of sterically shielding incorporated radical molecules from reductants. Moreover, it was shown that a high lipophilicity and correspondingly low water solubility was crucial for effective long term protection of encapsulated radicals.

(a) NCs containing TB. Note that the doublet in central position arises from ascorbic acid.

(b) NCs containing dTAM-dEE.
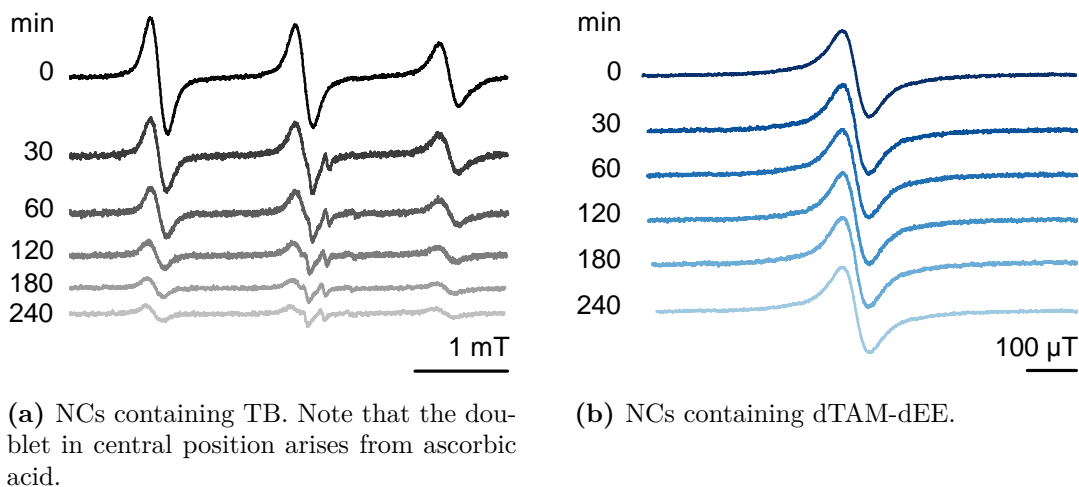
Figure 3.9: EPR spectra during (attempted) reduction of encapsulated spin probes ($c = 1\,\text{mM}$ in MCT) by ascorbic acid ($c = 1.25\,\text{mM}$) as measured at X-band.
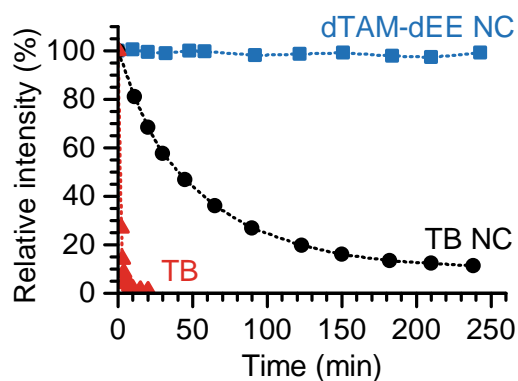
Figure 3.10: Change of the EPR signal intensity during (attempted) reduction of encapsulated spin probes ($c = 1\,\text{mM}$ in MCT) by ascorbic acid ($c = 1.25\,\text{mM}$). NCs with incorporated TB are compared to NCs with dTAM-dEE as well as unencapsulated TB.

3.4 Conclusion and outlook

The EPR line width of hydrophilic trityl radicals in aqueous solution broadened linearly and specifically with increasing oxygen content, rendering them suitable for oximetry in biological samples. These radicals were distinguished by their extremely narrow line widths. However, oxygen sensitivity of soluble radicals depends on the solubility of oxygen in the solvent, which is low in water. Hence, the accuracy and capability of detecting small changes in pO$_2$ were rather poor. Alternatively, lipophilic trityl triesters showed high and linear oxygen sensitivity in MCT and, particularly, in IPM. Encapsulation of the most promising candidate dTAM-dEE yielded oily-core NCs with favorable and reproducible properties. The NCs provided not only a constant microenvironment, but also protection against reduction. However, there were some limitations exacerbating *in vivo* applications.

First, the SNR was quite low. The oil content of the NCs was only 2.4 % (IPM, v/w) or 2.8 % (MCT, v/w). In other words, 1 mL NC suspension contained only 24 µL or 28 µL oil with a spin probe concentration of 1 mM. Thus, the radical concentration was actually only 0.024 mM/0.028 mM with respect to the whole formulation. A higher radical concentration would cause EPR line broadening by spin-spin exchange. Despite being commonly practiced (1 mM to 5 mM [128], 2.5 mM [124], 5 mM [127], 3 mM to 6.8 mM [130], 12 mM [77]), it is strongly advised against using higher radical concentrations. Increased oil contents would most probably lead to aggregation. The difficulty with a low SNR is aggravated by the fact that the main component of the formulation, water, absorbs microwave radiation. The dielectric loss will probably be even more pronounced upon dilution in biological samples. As a rule-of-thumb, SNRs have been found to be only one tenth *in vivo* compared to *in vitro* measurements in pilot experiments.

The second limitation is the presence of stabilizers due to their cytotoxicity. In pilot experiments, the cell viability of Jurkat T cells after 22 h of incubation with solutions of poloxamer 188 or polysorbate 80 in water ($c = 0.008\,\%$ to 1 %) was determined. The half maximal inhibitory concentration (IC50) of polysorbate 80 was found to be 0.14 %. In case of poloxamer 188, no effect on the cell viability could be proven. However, further investigations with relevant cell lines are required. On the other hand, a thorough screening is needed in order to find more suitable stabilizers.

Finally, when the NCs shall be administered *in vivo*, especially when they are injected intravenously, the formulation needs to be sterile. Sterilization procedures at elevated temperatures, such as wet or dry heat sterilization, cannot be employed. Not only do the high temperatures required for these methods exceed the glass transition temperature (T_g) of the polymer, they are unconducive to the entire formulation stability. A sterilization with chemicals like ethylene oxide is disadvantageous because of residual traces, which are difficult to be removed. Thus, there are only two commonly employed methods left: Radiation sterilization or aseptic processing and sterile filtration. In the latter case, one would have to deal with the fact that PVAc absorbs to common cellulose filters. Suitable filter materials have to be found. Apart from that, sterilization of the starting materials or sterile filtration of the solutions prior to NC preparation should be feasible. Apparently, radiation sterilization with electron beams or gamma radiation is the most applicable method since the temperature is only slightly elevated or can be controlled during the process and it is free of residues. However, crosslinking or chain scission of the polymer may occur and, as a consequence, change its molecular weight, and its physical as well as mechanical properties. Further, an influence on the EPR spin probes and their oxygen sensitivity cannot be precluded. Thus, radiation parameters, such as doses and temperature, have to be selected carefully to achieve sterility without affecting the formulation adversely. After

sterilization, both the properties of the polymer and the EPR behavior of the spin probes have to be examined comprehensively to ascertain an unchanged formulation quality.

The second and third limitation pose a manageable challenge for pharmaceutical technology. However, a poor SNR is inherent when NCs are employed. As stated above, the oil content in NCs is quite low. However, neither the oil amount encapsulated nor the spin probe concentration in the inner phase can be increased endlessly. As discussed earlier, the concentration of the stabilizers cannot be raised, either. Due to the very narrow line width of trityl radicals as well as their saturation behavior at higher microwave power, the SNR can neither be raised metrologically by increasing the microwave power settings or the modulation amplitude. One way to overcome this problem is probably the use of oily core microcapsules (MCs), where at least the oil content is increased. However, the application field might be restricted as, for instance, MPs normally cannot be injected intravenously. The second part of this chapter deals with another option, which is the use of particulate spin probes, whose line broadening at higher concentrations or microwave power is less marked.

Part II: LiNc-BuO

In contrast to soluble probes, the EPR line width of particulate radials, such as LiNc-BuO, responds to the pO_2 at the surface or in the microchannels of the crystals [20] with high and linear sensitivity [94, 97]. As the term *particulate* suggests, this kind of spin probes is employed as a solid without being dissolved. Thereby – in contrast to soluble probes – two facts are promised: The absence of line broadening at higher spin probe contents as well as independence of the surrounding microenvironment and, hence, the medium. However, to obtain reproducible results, it has to be ensured that the crystals are of unchanged quality. This is aggravated by the fact that LiNc-BuO appears in at least two polymorphs – a triclinic and a tetragonal modification. Thus, it is not only important to ensure purity and high crystallinity when LiNc-BuO is synthesized. Also during formulation preparation, it has to be ensured that the modification is retained. The following sections deal with the comprehensive characterization of LiNc-BuO as well as two formulation approaches: Nano- and microencapsulation.

3.5 Physicochemical characterization of the spin probe

LiNc-BuO was synthesized by a commercial supplier on request. To the author's knowledge, at this time, it had been the first attempt to synthesize LiNc-BuO outside Kuppusamy's laboratories. Synthesis was perfomed by experienced chemists and strictly followed the instructions, which had been published [94, 97]. Nevertheless, the synthesis was obviously sophisticated. Two promising batches could be prepared. However, according to the company, the yields were low and neither one fully complied the requirements, *i.e.*, the properties described in the literature. Unfortunately, various attempts to purify the material, *e.g.*, by recrystallization or column chromatography, failed. Therefore, it was necessary to characterize both batches comprehensively. Knowledge of the purity was crucial in order to estimate in how far impurities might have had an impact on the EPR measurements and to evaluate the applicability as an oxygen sensor.

3.5.1 Microscopy

Both LiNc-BuO batches appeared as dark-green, irregular but mostly isometrically shaped crystals of varying sizes, typically ranging from $1\,\mu m$ to $10\,\mu m$. The particles could hardly be desagglomerated. Some diamond-shaped crystals were found, which had been described for the tetragonal polymorph [94]. However, there were no needle-shaped crystals such as reported for the triclinic polymorph [58, 94].

3.5.2 Solubility

From the literature it was known that LiNc-BuO is soluble in common nonpolar solvents such as *n*-hexane, *n*-heptane, toluene, benzene, and also in the intermediate polar aprotic solvents dichloromethane and THF giving rise to a green-colored solution [58, 94, 97]. For a successful formulation development, further solvents had to be investigated. For instance, for NP preparation, LiNc-BuO needed to be dissolved and the solvent had to be miscible with water. For MP production, however, it was important that the spin probe was not dissolved at all. An overview over the solubility of both batches of LiNc-BuO in various selected solvents is given in table 3.3. As can be seen, LiNc-BuO was practically insoluble in polar protic solvents and in most polar aprotic solvents with the exception of dichloromethane and THF. Thus, THF was the only solvent suitable for nanoprecipitation of LiNc-BuO.

Table 3.3: Solubility of LiNc-BuO in various solvents according to Ph.Eur. and appearance of the solution and supernatant of the dispersion, respectively (− = practically insoluble, + = very slightly soluble, ++ = slightly soluble) [147].

Solvent	Batch 1		Batch 2	
	Solubility	Appearance	Solubility	Appearance
Acetone	−	slightly yellowish green	−	very slightly green
Acetonitrile	−	slightly brown	−	uncolored
Dichloromethane	++	dark green	++	dark green
DMF	−	greenish yellow	−	slightly green
DMSO	−	greenish yellow	−	uncolored
Ethanol	−	slightly brown	−	uncolored
Ethyl acetate	−	bluish green	−	bluish green
Glycerol 86 % to 88 %	−	uncolored	−	uncolored
n-Hexane	−	bluish green	+	bluish green
IPM	−	dark green	+	dark green
Isopropanol	−	slightly brown	−	uncolored
MCT	−	green	−	green
Paraffin, liquid	−	slightly green	−	slightly green
Paraffin, liquid + 2 % (m/m) Span® 80	−	yellowish green	−	slightly yellowish green
1-Propanol	−	slightly yellowish green	−	uncolored
THF	++	dark green	++	dark green
Water	−	uncolored	−	uncolored

For conventional microencapsulation of poorly water soluble drugs, usually an oil-in-water (o/w) emulsion solvent evaporation method is used, where dichloromethane or ethyl acetate serve as the organic phase [164, 165]. However, in dichloromethane, LiNc-BuO would be dissolved and might recrystallize in a different modification. Further, even though LiNc-BuO was practically insoluble in ethyl acetate, a bluish green colored supernatant was observed. That means, there was some kind of interaction with the solvent, which might risk recrystallization as well.

As an alternative, an o/o method was used in the work at hand, where an organic phase is emulsified in an immiscible oil. Liquid paraffin was suitable to be the outer phase because in contrast to liquid lipids, such as MCT or IPM, in paraffin, the supernatant was only slightly colored. At a closer look, the coloration seemed to stem from suspended LiNc-BuO particles rather than dissolved molecules. Thus, the interaction potential should have been low. On addition of Span® 80, the mixture was slightly yellowish, which was attributed to the presence of the surfactant, which is yellow itself. Acetonitrile is often used as the inner organic phase [164, 165]. Interestingly, when batch 1 was incubated with acetonitrile, the supernatant was slightly brown, whereas in case of batch 2, it remained uncolored. If the coloration was due to a decomposition or dissolution of LiNc-BuO, the supernatant of both batches would have been colored. This might have been a hint that batch 1 was impured by a substance with differing solubility properties. The assumption that batch 1 was impured was supported by the fact that in IPM and *n*-hexane, batch 2 was very slightly soluble, whereas in case of batch 1, a sediment remained.

3.5.3 EPR spectroscopy

3.5.3.1 Dry crystals

According to the literature, the EPR spectrum of LiNc-BuO shows a single line with 100 % Lorentzian line shape [94, 97]. For the triclinic polymorph, a line width of 155 µT had been reported [97], and 76 µT for the tetragonal one [94]. However, the EPR behavior of batches 1 and 2 was different (figure 3.11). Batch 1 exhibited a single line EPR spectrum of Lorentzian shape, but with a line width of 120 µT. The spectrum of batch 2, though, showed a superposition of two Lorentzian lines with line widths of 40 µT and 130 µT.

If the assumption of section 3.5.2 was true that batch 1 was impured, it might have been an EPR silent compound. On the other hand, the EPR measurements revealed that batch 2 was not totally pure, either. The presence of two EPR species with different line widths might have had several reasons. First, as mentioned above, the two different polymorphs of the substance had different line widths. Probably, batch 2 was impured by another polymorphic form. Second, it had been described that the EPR line width of

(a) LiNc-BuO, batch 1.

(b) LiNc-BuO, batch 2.
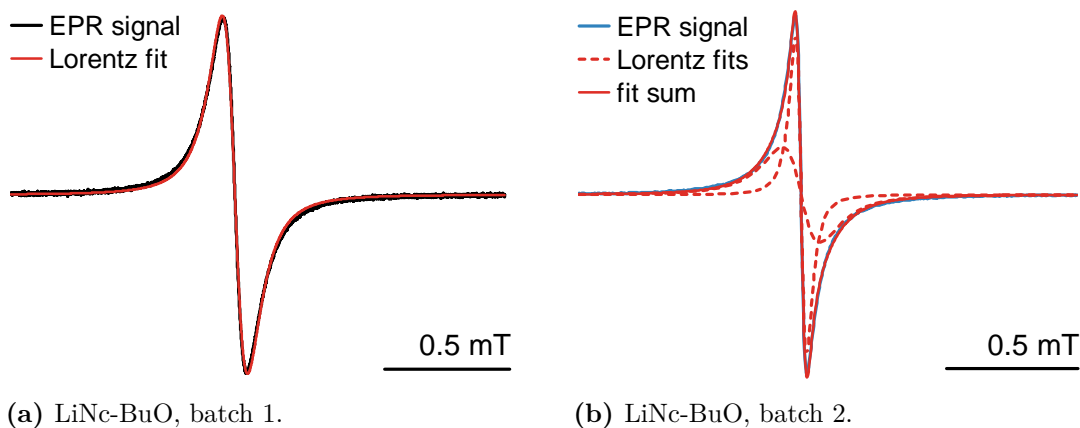
Figure 3.11: EPR spectra of dry LiNc-BuO and Lorentzian curve fitting.

LiNc-BuO was also dependent on the particle size of the crystals. Under aerobic conditions, Pandian *et al.* reported a line width of $<100\,\mu T$ for raw microcrystals, which was markedly narrower compared to the line width of nanocrystals of 100 nm to 500 nm size as obtained by sonication ($>100\,\mu T$) [94]. Similar trends have been reported for LiPc: The total EPR line shape was observed to be a composite of several components corresponding to different sizes present in the microcrystalline powder [55]. The oxygen flow into the channels can be severely influenced by the particle size as it is inversely proportional to the length of the channels [55]. The polydisperse sample they used exhibited a spectrum with three species of different line widths. Third, it had been stated that, possibly due to disordered growth, variations in particle size, EPR line width, and oxygen sensitivity could be observed from batch to batch of preparation or recrystallization of LiNc-BuO [94].

These facts in mind, it seemed to be unreasonable to compare the EPR line widths ascertained here with data from the literature or among different publications. For instance, Pandian *et al.* used sonicated crystals with $<2\,\mu m$ of the triclinic polymorph in 2003 [97], while in 2010, the raw material with a size of several micrometers had been employed [94]. Instead of comparing the absolute line widths, it might rather be reasonable to investigate the oxygen sensitive behavior of the material (section 3.5.4).

3.5.3.2 Solutions/dispersions

Particulate radicals respond to the pO_2 rather than c_{O_2} [24]. In contrast to soluble spin probes such as trityl radicals, their oxygen sensitivity should be independent of the solubility of oxygen in the respective solvent. At a given temperature and pressure, the pO_2 in the gas above a solvent should be exactly as high as in the microchannels of suspended

LiNc-BuO crystals, into which small molecules such as oxygen can diffuse. Pandian *et al.* investigated the EPR spectrum in aqueous dispersion media (water, PBS, cell culture media) only. They stated that the line width and line shape of the particulates were not affected. Upon dissolution there was no signal anymore, suggesting that the radical is not stable in the molecular form. Other solvents except those, in which the compound is freely soluble, had not been tested [97]. To further study the assumption made above, all solutions/dispersions of batch 1 from section 3.5.2 were measured by EPR spectroscopy. The line widths determined in various solvents are given in table 3.4. Examples of EPR spectra are shown in figure 3.12. The EPR measurements of batch 2 are not depicted here because the presence of two species aggravated a meaningful analysis of the data.

Table 3.4: EPR line widths of LiNc-BuO (batch 1) in various solvents on the day of preparation (* = superposition of two species). Oxygen solubilities at $20\,°C$ to $25\,°C$ and $0.213\,bar\,pO_2$ are taken from Montalti *et al.* [159] or in case of IPM and MCT determined by gas chromatography.

Solvent	EPR line width (µT)	Oxygen solubility (mmol/l)
Acetone	42	2.4
Acetonitrile	59	1.9
Dichloromethane	550	2.2
DMF	54	–
DMSO	69	0.46
Ethanol	59	2.1
Ethyl acetate	48	–
Glycerol 86 % to 88 %	51 + 8*	0.07
n-Hexane	74	3.1
Isopropanol	98 + 33*	2.2
IPM	112	1.29
MCT	112	0.98
Paraffin, liquid	110	–
Paraffin, liquid + 2 % (m/m) Span® 80	111	–
PBS 6.2	111	–
PBS 7.4	110	–
1-Propanol	56	1.4
THF	600	2.1
Water	113	0.28

Surprisingly, the EPR line width of LiNc-BuO crystals appeared to be dependent of their environment. In water, buffer, IPM, MCT, and paraffin, the line width was comparable
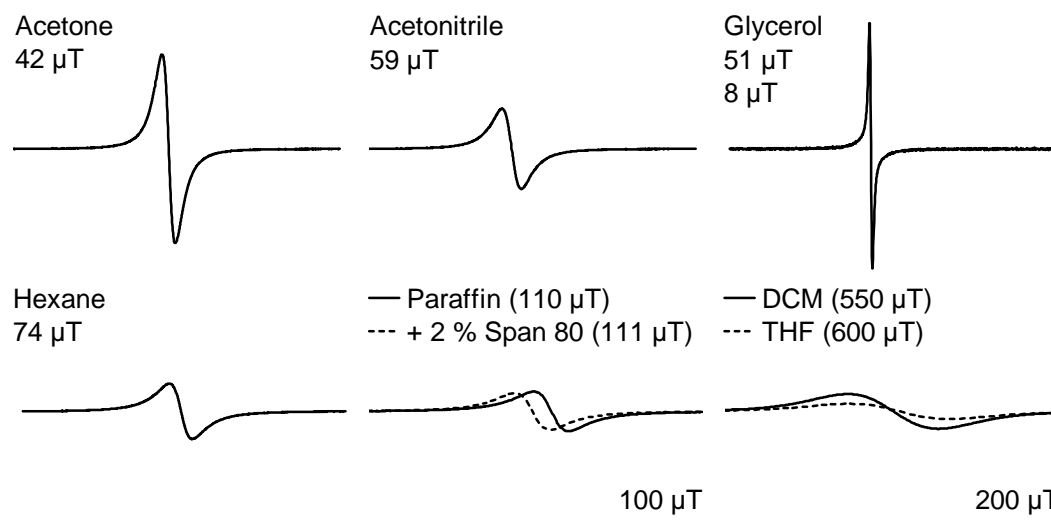
Figure 3.12: EPR spectra of LiNc-BuO (batch 1) in solution/dispersion (1 mg/ml) as measured on the day of preparation. Note that the sweep of the dichloromethane (DCM)/THF spectrum was twice as broad as of the others and the modulation amplitude was ten times higher. Thus, the DCM/THF spectrum is broader and less intensive than it appears here. Actually, under the same measurement parameters, the signal would have vanished in the noise. Note that small line shifts may have been caused by different tuning.

to the dry material. Albeit, upon storage in aqueous dispersion, the line width was not reliably stable (sections 3.5.5 and 3.7.4). In all other solvents, in which the radical was not (completely) dissolved, the line widths were narrower. This cannot be attributed to the different oxygen content in the solvents as can be concluded from comparing the line widths and oxygen solubilities in the respective solvents. Interestingly, two EPR species appeared in glycerol and isopropanol.

It is assumed that solvent molecules somehow interact with the spin probe: Probably, they are adsorbed at the surface or diffused into the microchannels of the crystals, thereby displacing oxygen molecules. Also chemical changes at the surface cannot be excluded. Unfortunately, it had not been tested whether these processes were reversible, *i.e.*, whether the line width was broadening again after evaporation of the solvents. Contradicting the statement of Pandian *et al.* that LiNc-BuO in its molecular form is not a stable radical [97], the spectrum in dichloromethane and THF solution could be detected. Only a higher modulation amplitude was needed as the line widths were very broad. Upon evaporation of the solvents and recrystallization, there was a wide variety of resulting line widths. It seemed to be uncontrollable, no matter which conditions had been chosen – slow or fast evaporation in vacuum or at elevated temperatures up to 80 °C.

The independence of the line width from environmental parameters other than oxygen was regarded as one of the main advantages of particulate spin probes in comparison to soluble ones. It is remarkable that although LiNc-BuO responds to the pO_2, its line width is not predictable either. However, here, LiNc-BuO and its formulations are intended for use in biological samples. The line width in aqueous media was similar to dry LiNc-BuO crystals, so LiNc-BuO is still regarded suitable for oximetric experiments at hand.

3.5.4 Oxygen response

Depending on the polymorphic form, different oxygen sensitivities had been determined for LiNc-BuO: For the triclinic polymorph, the broadening was $0.85\,\mu T/mmHg$ [58, 97], and $0.45\,\mu T/mmHg$ for the tetragonal form [94].

(a) LiNc-BuO, batch 1 (mean, $n = 3$). **(b)** LiNc-BuO, batch 2 ($n = 1$).
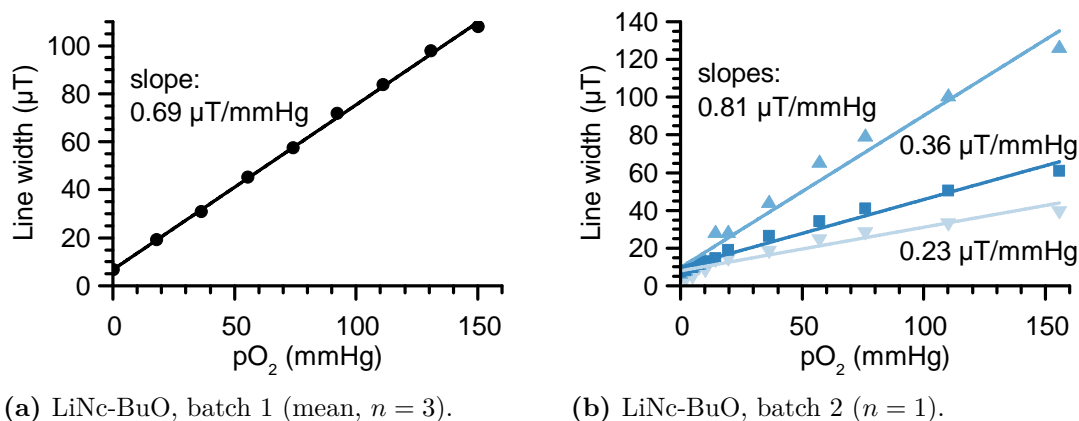
Figure 3.13: Oxygen calibration curves of dry LiNc-BuO crystals at $37\,°C$ (lines: linear regressions).

The EPR line width of batch 1 increased linearly with pO_2 (figure 3.13). The calculated slope was $0.69\,\mu T/mmHg$, which is in the reported range. Under all oxygen contents investigated, the EPR spectrum of batch 1 consisted of only one species. In contrast, the EPR spectrum of batch 2 always exhibited two species (section 3.5.3). Unfortunately, none of them responded linearly to an increasing pO_2 in the desired range of $0\,mmHg$ to $155\,mmHg$. The response was saturated. According to the two-spin states model, when all the mobile spin are fixed, increasing pO_2 does not influence the line width anymore [55]. Ilangovan *et al.* observed this saturation behavior for the apparent line width of LiPc already above $50\,mmHg$ [55]. They assumed that smaller crystals responded with higher sensitivity, but fast saturation, while with larger crystals, the linear range was broader, but the sensitivity was lower. This effect was caused by physical adsorption [62]. However,

with LiNc and LiNc-BuO, no such saturation behavior was observed, probably due to the wider channels [62]. Perhaps, the two species of batch 2 with different oxygen sensitivities also stemmed from different particles sizes. However, neither of the two species exhibited a linear response range which was broad enough for the purpose at hand. Moreover, LiNc-BuO formulations to be developed later in this work aim at being administered *in vivo*, where areas of lower and higher oxygen contents probably lie close together, which will already lead to a superposition of EPR species with different line widths. Hence, analysis of *in vivo* spectra would be aggravated enormously, and information would get lost.

The oxygen response of batch 1 determined at 37 °C was further compared to the response at 20 °C. The slope of the curves was similar meaning that the oxygen sensitivity was unchanged (see appendix, figure A.3).

To sum up, even if batch 1 was impured as assumed from section 3.5.2, the impurity did not have any negative impact on its usability as an oxygen sensing material. However, a reliable determination of oxygen contents using batch 2 was aggravated by the fact that its EPR spectrum showed two species, neither of which showed linear line broadening over the desired range. Consequently, batch 1 was rather useful for EPR oximetry and, therefore, used for microencapsulation and the subsequent experiments at hand. However, for the sake of completeness, the stability as well as identity and purity investigations were carried on with both batches.

3.5.5 Stability

The stability of the EPR signal of batch 1 during storage was investigated analogous to MPs. To facilitate a comparison between the stability of the raw material and the incorporated spin probe, all results are presented in section 3.7.4. It is further referred to section 3.6.2.2. During NP production, a decomposition of the radical was often noticed, which is elucidated therein.

3.5.6 Identity and purity

To assure the identity of the material at hand, several techniques have been employed. Knowledge of the purity was necessary to estimate the impact of potential impurities and, hence, the suitability of the material as a reliable oxygen sensor.

XRD

Since it was known that LiNc-BuO showed polymorphism, both batches of LiNc-BuO were analyzed by XRD in order to investigate their crystallinity. In figure 3.14, the diffractograms are compared to literature data of both polymorphic forms: For the triclinic

polymorph, a powder diffractogram had been published [58], while for the tetragonal form, a crystal information file of a single crystal was available [94], which was used to simulate its powder XRD pattern. Nc-BuO, which is the educt of the synthesis and might have been a possible impurity, was also measured.
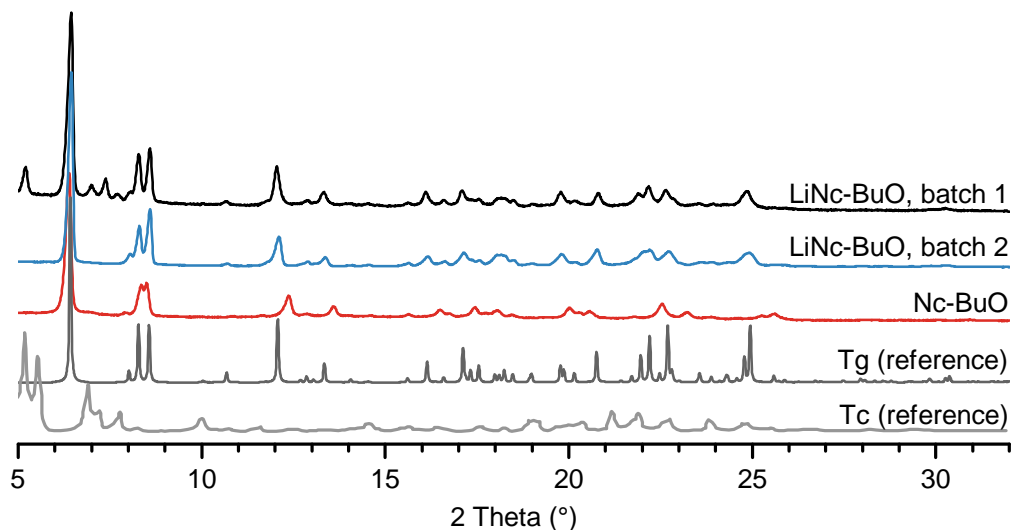
Figure 3.14: Powder x-ray diffractograms of LiNc-BuO and Nc-BuO. For comparison, reference powder XRD patterns of the tetragonal polymorph (Tg, simulated from a crystal information file [94]) as well as the triclinic form (Tc, digitized from a published powder diffractogram [58]) are shown as well.

As can be seen, the predominant polymorph in both batches was the tetragonal one. However, in case of batch 1, the peaks were slightly shifted to lower angles. Peak shifts were increasing with angle, which might have been caused by differences in the lattice parameters, in particular, an expanded unit cell. Further, there were some additional reflections, which did not occur in the reference diffractogram. Thus, there was a second phase. Unfortunately, these peaks could not be identified. It is unlikely, however, that they originated from the triclinic polymorph or Nc-BuO. The background pattern of batch 1 hinted at the presence of an amorphous phase or might have been influenced by crystals of different sizes and orientations. However, grinding of the material prior to XRD measurements was not possible due to destruction of the crystals. In contrast, the diffraction pattern of batch 2 showed narrow peaks and low background indicating high crystallinity of the sample. The positions and relative intensities of the peaks were comparable to those of the tetragonal polymorph. Thus, batch 2 was X-ray diffractometrically phase pure. However, this fact did not exclude the presence of impurities. There might have been traces of XRD amorphous impurities without proper Bragg diffraction peaks.

UV/Vis/NIR spectroscopy

The UV/Vis/NIR spectra of both batches of LiNc-BuO and Nc-BuO were compared to literature data [94] (figure 3.15). It was obvious that both batches contained LiNc-BuO. Pandian *et al.* found Q bands at 1005 nm, 705 nm, and a weak band at 857 nm whereas Nc-BuO showed a strong Q band at 865 nm [94].
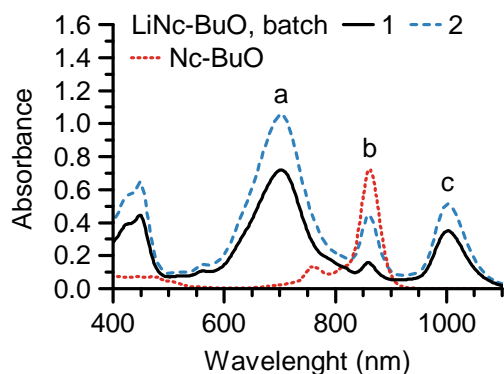
Figure 3.15: UV/Vis/NIR spectra of solutions of LiNc-BuO ($c = 20\,\mu\mathrm{g/ml}$) and Nc-BuO ($c = 5\,\mu\mathrm{g/ml}$) in THF against THF as blank.

In case of batch 1, the corresponding maxima were at 1002 nm, 702 nm, and 858 nm. Batch 2 had maxima at 1002 nm, 702 nm, and 860 nm. It was noticable, however, that bands a and c were slightly hypsochromically shifted, whereas the weak band b was bathochromically shifted, which was even more pronounced for batch 2. The relative peak heights could only hardly be compared to the literature data, since unfortunately no absolute values had been given. The height ratios of peak a to peak c corresponded to the estimated literature data quite well (batch 1, 1:0.49, batch 2, 1:0.49, literature, $\approx$ 1:0.53) [94]. It was conspicuous, though, that the height ratios of peak a to peak b of batch 1 (1:0.22) and, particularly, batch 2 (1:0.43) were strongly deviating from the estimated ratio of the literature data ($\approx$ 1:0.12) [94]. Both facts affirmed the assumption that batch 2 was impured by the educt Nc-BuO and peak b resulted from a superposition of the LiNc-BuO and the Nc-BuO peak. Both polymorphic phases are identical in their molecular form, so that UV/Vis/NIR spectrometry was incapable of giving further information on this issue.

IR spectroscopy

IR spectra of both batches of LiNc-BuO and Nc-BuO are depicted in figure 3.16. At higher wavenumbers in the group frequency region, prominent bands ($\nu_{\min}$ in cm^{-1}, ν: stretching vibration) were found at 3070 ($\nu_{\text{C-H}}$ aromatic), 2957 ($\nu_{\text{C-H}}$ methyl), 2929 ($\nu_{\text{C-H}}$ methylene), and 2870 ($\nu_{\text{C-H}}$ methyl). The educt Nc-BuO as well as batch 2 showed an additional band at 3298 ($\nu_{\text{N-H}}$ secondary amines). At lower wavenumbers, there was a strong band at 1585 (LiNc-BuO) or 1579 (Nc-BuO) ($\nu_{\text{C-C}}$ aromatic), which was also apparent in a reference spectrum [166]. Batch 1 showed additional weak bands at 1708 and 1734. The strongest
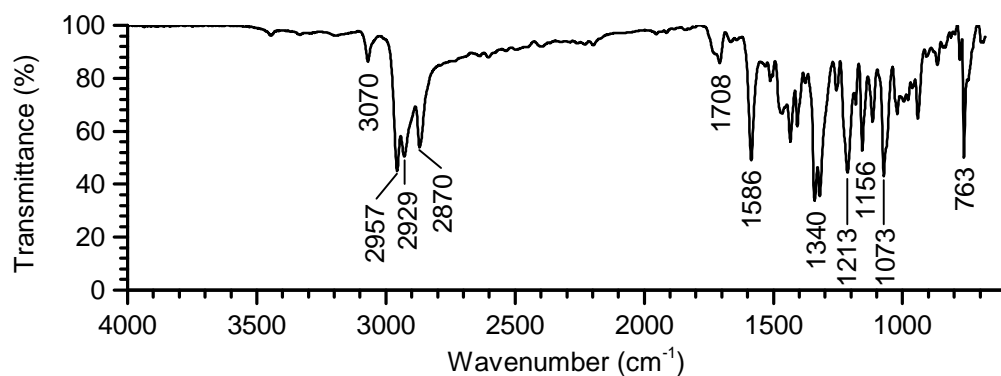
(a) LiNc-BuO, batch 1.
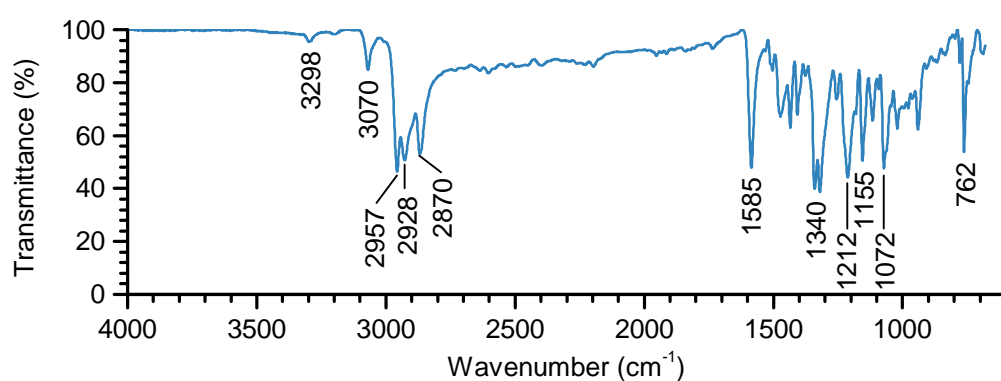
(b) LiNc-BuO, batch 2.
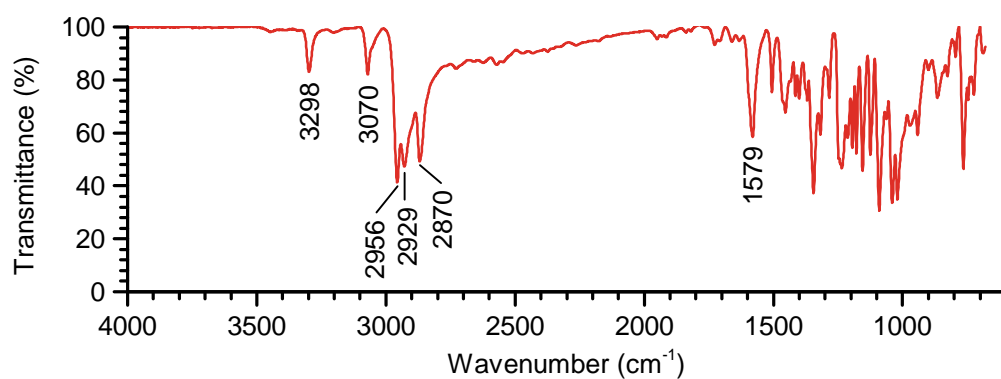
(c) Nc-BuO.

Figure 3.16: IR spectra of LiNc-BuO and Nc-BuO. Numbers label minima $\nu_{\min}$ in cm^{-1}.

bands in the fingerprint region at 1586, 1340, 1213, 1156, 1073, and 763 corresponded to the published spectrum [166]. The fingerprint regions of both batches of LiNc-BuO were very similar. These results confirmed that both batches contained LiNc-BuO. Batch

2, however, was probably impured by the educt Nc-BuO. The additional peaks in the spectrum of batch 1 were difficult to be interpreted. In this region, usually C=O stretching vibrations appear, but these bands are typically very strong and should not be present in this case. Pandian *et al.* investigated the impact of NO_2 on the properties of LiNc-BuO [166]. They found a band at 1721 which was attributed to free NO_2 trapped in the lattice. They also suggested that NO_2 would react with LiNc-BuO to diamagnetic LiNc-BuO$^+$ and nitrite ions. However, the IR spectrum at hand was free of any broadening effect or bands indicative of nitrite ions. Thus, it is very unlikely that batch 1 was impured by free NO_2. After all, it remained unclear, where the additional bands derived from.

HRMS

The molecular mass was analyzed by HRMS to confirm the identity and further investigate the purity. In figure 3.17, the interesting region of the mass spectrum is shown.

(a) LiNc-BuO, batch 1.   **(b)** LiNc-BuO, batch 2.
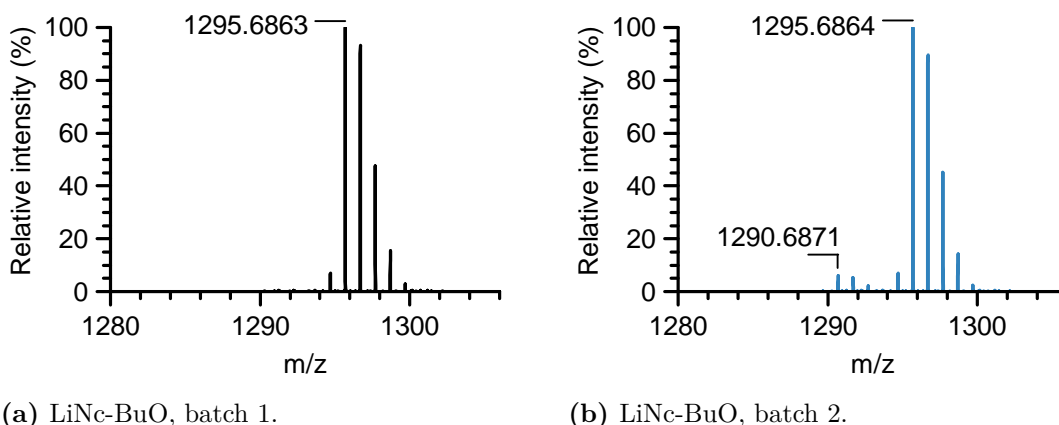
Figure 3.17: Pertinent range of mass spectra of LiNc-BuO. The whole spectra can be found in the appendix (figures A.4 and A.5) as well as the spectrum of Nc-BuO (figure A.6). Data is given as the mass-to-charge ratio (m/z, in u/e).

In batches 1 and 2, the identity of LiNc-BuO was verified by the presence of a base peak with m/z 1295.6863 and m/z 1295.6864, respectively. This corresponded to the calculated molecular mass of 1295.6880 u of the singly charged ion $C_{80}H_{88}O_8N_8Li$ [M]$^+$. The deviation was less than 2 ppm. In batch 2, however, another peak was found at m/z 1290.6871. It was assigned to the singly charged educt ion $C_{80}H_{90}O_8N_8$ [M]$^+$ with a calculated mass of 1290.6876 u. Thus, in contrast to the XRD results, batch 1 was mass spectrometrically pure, whereas batch 2 was most certainly impured by the educt Nc-BuO. However, the relative intensity compared to the base peak was only 6 %. All other impurities had a relative abundance of only <1 % and were attributed little importance.

DSC

Albeit XRD investigations indicated a high crystallinity of LiNc-BuO in both batches, the DSC curves did not show any endothermic melting peak (figure 3.18). In fact, both batches showed an exothermic peak at 240 °C (batch 1) or 239 °C (batch 2), which indicated decomposition. In the second heating curve, this peak was not present anymore suggesting that the decomposition was not reversible by cooling.
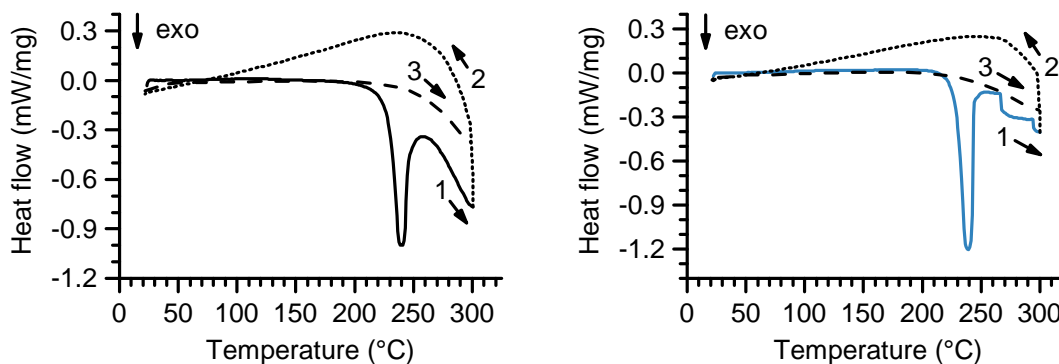
(a) LiNc-BuO, batch 1.   **(b)** LiNc-BuO, batch 2.

Figure 3.18: DSC thermograms of LiNc-BuO. Solid lines (1): first heating curves (1 K/min), dotted lines (2): cooling curves (−5 K/min), and dashed lines (3): second heating curves (1 K/min).

Conclusion

Taking all results into consideration, it could be ensured that both batches mainly contained LiNc-BuO, but it must be noted that most probably both were impured. In case of batch 1, it could not finally be clarified, to which substance some XRD and IR signals could be attributed. However, their abundance was low and their appearance did not have any negative impact on the EPR spectrum or the oxygen sensitivity. In contrast, UV/Vis/NIR, IR, and MS measurements left no doubt that batch 2 was impured by Nc-BuO. It might be remaining unreacted starting material or the decomposition product of the lithium salt. Nc-BuO should not affect the EPR measurements since the substance is diamagnetic. The EPR spectrum exhibited two species, though, which would exacerbate the interpretation of oxygen measurements. After all, an application of the LiNc-BuO batches for further investigations seemed to be reasonable, even though neither of them fully complied in terms of their purity. Whenever LiNc-BuO was dissolved and the crystals were destroyed anyway, *e.g.*, during NP preparation, probably both batches were applicable. For MP preparation, when the raw microcrystals were used, batch 1 was preferred.

3.6 NPs

The promising results with trityl loaded NCs described in part one of this chapter were encouraging to formulate LiNc-BuO as NPs. In contrast to soluble radicals, there is no line broadening at high concentrations due to the crystalline nature. Further, the spectrum is less susceptible to saturation meaning that higher microwave powers can be applied to enhance the signal intensity without compromising the oxygen sensitivity [97]. Thus, not only higher concentrations, but also higher microwave powers can be used to achieve better signal intensities without line distortions. Moreover, at least for the tetragonal form of LiNc-BuO, it was found that the oxygen sensitivity depends on the crystal size [94]. Pandian *et al.* compared the oxygen sensitivity of raw microcrystals with nanocrystalline particles obtained by sonication. On reduction of the crystal size, the oxygen sensitivity could be enhanced by about 50 %. However, NPs were produced by sonication. At the end, the dispersion was placed on ice, large particles were allowed to settle down, and only the decanted liquid was used for further measurements. It is not exactly stated in this paper from 2010, but it is assumed that the same method was used, which had been described in 2003 by the same group [97]. Disadvantages of this method are the loss of substance since a few large particles might carry the predominant part of the mass, as well as the unknown LiNc-BuO concentration in the resulting NP dispersion. In this work, different approaches had been tested to prepare well defined NPs with known LiNc-BuO content. Nanoprecipitation and microfluidics served as bottom-up techniques, whereas nanomilling was used as a representative top-down process.

3.6.1 Preparation

First, a solvent displacement method had been tested for NP preparation. At this early stage of formulation development, it was valuable to try the NP preparation with and without PVAc. When LiNc-BuO was nanoprecipitated without PVAc, uncoated LiNc-BuO nanocrystals were obtained. On addition of PVAc, the polymer was expected to form a shell surrounding the nanocrystals. The reasons to decide for coated devices have already been discussed for trityl radicals in section 3.3. With particulate spin probes such as LiNc-BuO, the main advantage is that spin probe-tissue interactions can be prevented. However, PVAc could probably disturb the crystallization process. Since both batches of LiNc-BuO were most likely impured, it was unclear which batch was more suitable for NP preparation and hence, both were tested. THF was used as the organic solvent as it dissolved LiNc-BuO and it was miscible with water. With poloxamer 188 (0.5 % (m/m) in the aqueous phase) as a hydrophilic stabilizer, stable NP dispersions could be obtained.

As an alternative, attempts have been made to transfer this beaker method to a mi-

crofluidic preparation process in order to receive uniform NPs under process conditions, which were easily reproducible. A micromixer chip with twelve mixing stages had been deployed. According to the manufacturer's data sheet, this device is suitable for rapid mixing of fluid streams, which is favorable for rapid crystallization and NP preparation. Its mixing performance was measured across a wide range of total flow rates. Using very small flow rates, only one mixing stage and 4200 ms were required to achieve complete mixing. At worst, seven mixing stages and 459 ms to 919 ms were needed at medium flow rates. At very high flow rates swirling occurs in the flow streams, reducing mixing time further. To achieve a ratio of 1:10 (v/v, organic to aqueous phase), the effective flow rates were first adjusted to 1:10. Starting from that, different flow rates (in the range of 1 µl/min to 50 µl/min) and flow rate ratios were tested. However, the results were not satisfactorily: Either the color turned from green to yellow/brown, by which a decomposition of the radical was easily recognizable (see UV/Vis/NIR spectra of LiNc-BuO and its precursor Nc-BuO, figure 3.15), or there was a precipitation and aggregation inside the micromixer chip. Even if only small debris were present, they immediately had to be removed and, hence, the whole preparation process had to be stopped.

Nanomilling was applied as a complementary method. Since LiNc-BuO did not have to be dissolved, the critical recrystallization step was omitted. To save substance, only a pilot study was performed with typically used milling parameters. To improve the wettability, different excipients were tested: Polysorbate 80 and poloxamer 108 as surfactants as well as ethanol as a co-solvent. Although comminution down to a submicron size range was feasible, resulting particle size distributions appeared to be highly polydisperse (PdI >0.4). Neither mild process conditions (180 min at 200 rpm) nor high energy milling (30 min at 800 rpm) led to narrower size distributions. Furthermore, the resulting EPR spectrum was very broad, probably since the LiNc-BuO crystals had been damaged. DSC measurements revealed that the exothermic peak, which had been characteristic for LiNc-BuO powder (figure 3.18), disappeared after grinding (see appendix, figure A.7).

After all, the most promising was the initial solvent displacement method. The results of the physicochemical characterization of the NPs are given in section 3.6.2.

3.6.2 Physicochemical characterization

The NP dispersions obtained by the solvent displacement method were intensively green colored and opalescent as well as free of visible aggregates. Analogous to trityl loaded oily core NCs, the size of LiNc-BuO loaded NPs was determined by DLS and NTA. Intensity weighted and number based particle size distributions of coated and uncoated NPs are shown in figure 3.19.

(a) Typical intensity weighted particle size distributions as obtained by DLS.

(b) Number size distributions as measured by NTA.
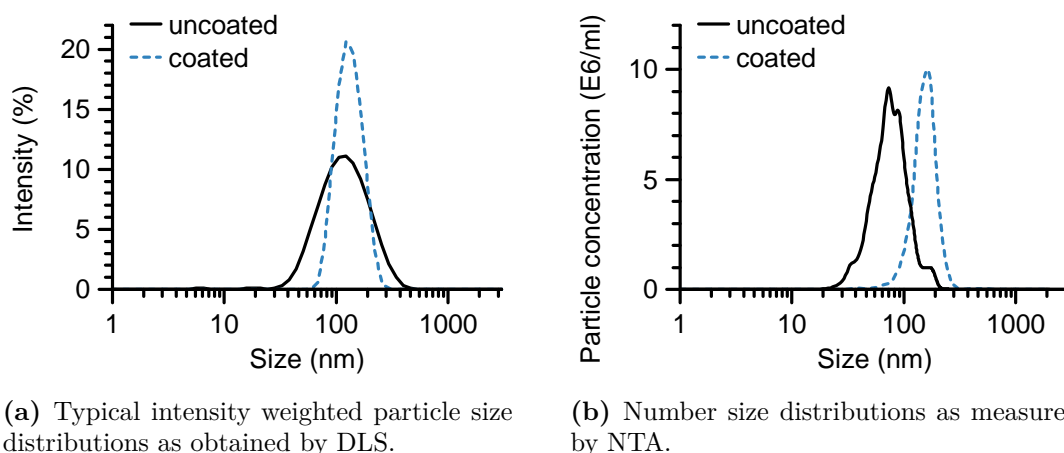
Figure 3.19: Hydrodynamic particle sizes of coated and uncoated NPs. Coated NPs were prepared with 1.25 mg LiNc-BuO and 5 mg PVAc in 0.5 mg THF, which were injected into 5 ml aqueous phase. Uncoated crystals were obtained by omitting PVAc.

The z-average of uncoated NPs obtained by DLS typically was about 94 nm. The particle size distributions were polymodal and polydisperse, indicated by a high PdI >0.25 and the appearance of side peaks at very small particle sizes, albeit their intensity was very low. At least, it is positively remarkable that the samples were free of large aggregates. NTA measurements confirmed that the size distribution was quite broad, but there was only one peak present. By NTA, the mean hydrodynamic diameter was found to be 92 nm, which is in good agreement with the DLS results.

In contrast, coating with PVAc led to a monomodal and monodisperse particle size distribution with a z-average of about 125 nm and a very low PdI <0.05 determined by DLS. By NTA measurements, the very narrow size distribution was affirmed, however, the calculated mean hydrodynamic diameter was 164 nm, which was markedly larger than the z-average gathered by DLS. As can be seen in figure 3.15, LiNc-BuO absorbs light at the wavelength of the employed red laser (633 nm). Additionaly, LiNc-BuO shows fluorescence in this range, which will be discussed in section 3.7.2. Both effects might disturb the measurements. It has to be stated that the attenuation, which had automatically been selected by the DLS measurement software, was always quite low (attenuation levels of 7-11, where 11 means no attenuation is applied). Probably due to absorption of the laser light, a very high intensity of the incident light was needed in order to achieve a count rate in the optimal range for the detector. Albeit the mean count rates were always in the desired range, these results should probably be treated with care.

(a) Uncoated LiNc-BuO nanocrystals.

(b) PVAc coated NPs.

(c) Uncoated LiNc-BuO nanocrystals.
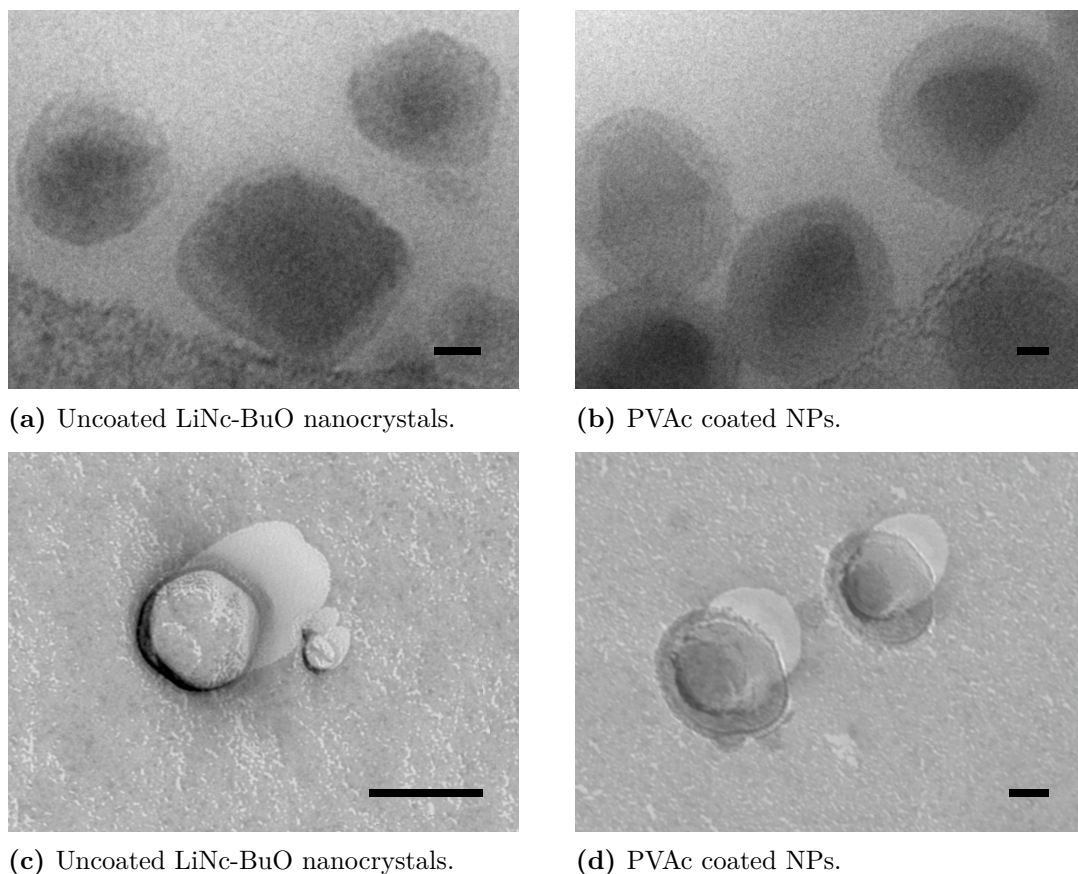
(d) PVAc coated NPs.

Figure 3.20: Morphology investigations of coated and uncoated NPs: (a, b) Cryo-TEM images (bar size: 20 nm) and (c, d) TEM images of freeze-fractured replica of NPs (bar size: 50 nm). Coated NPs were prepared with 1.25 mg LiNc-BuO and 5 mg PVAc in 0.5 mg THF, which were injected into 5 ml aqueous phase. Uncoated crystals were obtained by omitting PVAc.

The morphology of the NPs was investigated by TEM. In cryo-TEM images, uncoated nanocrystals appeared as irregular but mostly isometrically shaped crystals in a size range of 31 nm to 116 nm (figure 3.20a). PVAc coated NPs were almost spherical in shape; their size varied between approximately 46 nm to 192 nm (figure 3.20b). It must be stated that during sample preparation for cryo-TEM a particle selection occurs usually, and, moreover, the number of counted particles (about 50) was quite low, which might explain the deviation from DLS and NTA measurements described above. However, cryo-TEM was impressively capable of visualizing the inner morphology of the NPs, in particular, of the coated ones. In general, dark regions in TEM images result from strongly scattering materials, while the image is bright where scattering in specimen is weak. The contrast theories for amorphous and crystalline phases are quite different, though. Since the PVAc

shell is amorphous, there is only a short-range order of the atoms, but they are not arranged lattice-like as known from crystals [167]. Here, light and shade are mainly produced by mass-thickness contrast. As the name implies, it is a function of the thickness and the atomic numbers of the specimen [168]. This effect explains why NPs appear darker in the middle (figure 3.20a). Crystalline materials additionally show diffraction contrast, in which light and shade are determined by local orientations relative to the electron beam [169]. The electrons are diffracted according to Bragg's law. Depending on how well the Bragg condition is satisfied, the mass-thickness contrast is generally weaker and overshadowed by the stronger effects of electron diffraction (assuming there are no large differences in the atomic numbers) [170]. Hence, the TEM image (figure 3.20b) shows NPs with LiNc-BuO crystals whose lattice orientation was sufficient to meet the Bragg condition. That means, the embedded crystals diffracted the electron beam strongly and appeared as dark areas sharply contrasting with the brighter amorphous polymer shell.

With freeze-fracture TEM, these results could be confirmed. To make replica of the frozen-fractured surfaces, NPs were metal-coated unidirectional at an oblique angle. Consequently, features protruding from the interface show a black accumulation of platinum below and a white absence-of-platinum shadow above [171, 172]. The shadow behind each uncoated LiNc-BuO nanocrystal was clearly visible, suggesting that NPs were mainly fractured convexly (figure 3.20c). In contrast, the shadow of coated NPs had not been created behind the whole diameter of the NP (figure 3.20d). Thus, the PVAc shell of coated NPs was cross-fractured without producing a shadow. Embedded LiNc-BuO crystals were also most likely fractured convexly creating a shadow with smaller extent than the diameter of the NP. These results supported the initial assumption that LiNc-BuO nanocrystals were covered by a PVAc shell.

3.6.2.1 EPR spectroscopy

In contrast to the encouraging results of the particle size and morphology analysis, the EPR characterization of both uncoated and coated NPs was unsatisfying. As stated before (section 3.5.4), a single line EPR spectrum with one species serves best for reproducible oxygen measurements. The line width should be narrow in order to yield high SNRs. Unfortunately, no matter which LiNc-BuO batch had been deployed, the EPR spectra of the NPs were often composed of two species. That means, the spectra could only be simulated using two Lorentzian lines with different line widths. Neither of them was linearly sensitive to the oxygen content (data not shown), which would have complicated oxygen measurements enormously. Merely in particular cases the spectra could be regarded as single lined (figure 3.21a).

(a) Spectrum fitted by one species.

(b) Spectrum fitted by two species.
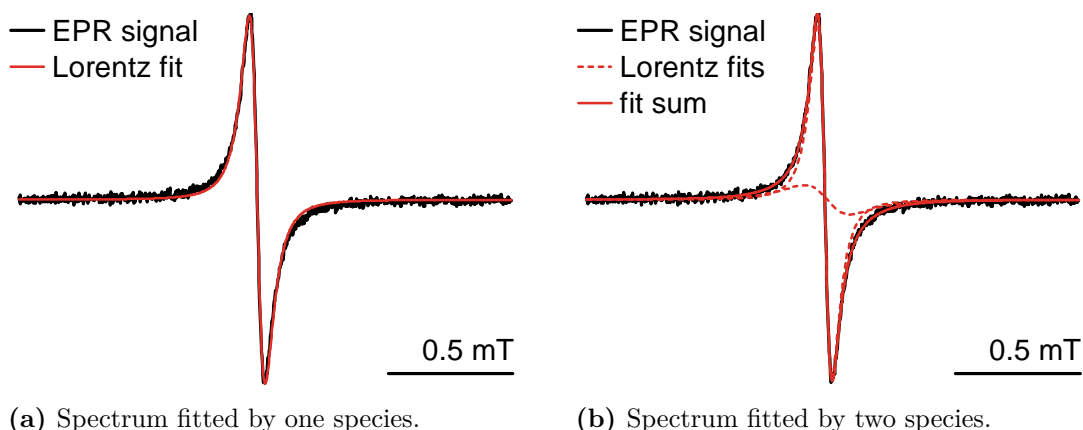
Figure 3.21: Best EPR spectrum of all prepared batches of uncoated LiNc-BuO nanocrystals. NPs were prepared with 1.25 mg LiNc-BuO in 0.75 mg THF, which were injected into 5 ml aqueous phase. The final NP dispersion was filled up to 2 g.

However in these rare cases, neither the line shapes nor the absolute line widths were reproducible in a new production process. Moreover, the line widths were unstable, *i.e.*, mostly decreasing, over time of storage as can be seen in figure 3.22. This figure also illustrates the wide variety of line widths, even on the day of preparation.
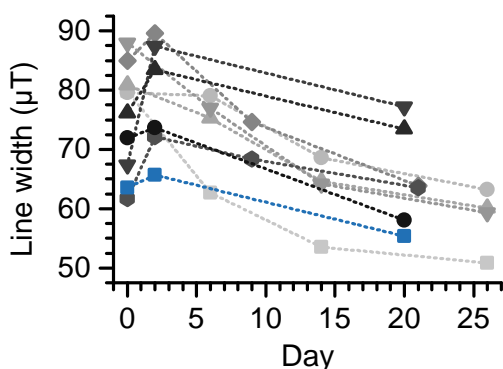
Figure 3.22: Changes in the apparent EPR line widths of selected NP dispersions over time of storage. NPs were prepared under several conditions, *i.e.*, concentrations, volumina, and phase-to-phase ratios were varied. However, all dispersions showed the same trend of unstable line widths. The curve highlighted in blue shows the apparent EPR line widths of the best NP batch, whose spectrum has been pictured in figure 3.21.

There are various conceivable explanations for the appearance of two EPR species as already mentioned in section 3.5.3. It had been described that the EPR line width of LiNc-BuO was dependent on the particle size of the crystals. Under aerobic conditions, Pandian *et al.* reported a line width of $<100 \, \mu T$ for raw microcrystals, which was markedly narrower compared to the line width of nanocrystals of 100 nm to 500 nm size as obtained by sonication ($>100 \, \mu T$). Particle size analysis of uncoated NPs showed that the size distribution was polydisperse or, in other words, quite broad. All methods revealed that particles with a size $<100 \, nm$ were present. There is no reference value for the EPR line

width of such small LiNc-BuO crystals. So, quite possibly, species with different line widths in the EPR spectrum stemmed from different particle sizes. However, since the size distribution did not show two equally defined particle size peaks, the EPR spectrum would more likely have been composed of multiple lines. Second, there might have been a co-crystallization of different polymorphs of LiNc-BuO. For the triclinic polymorph, a line width of $155\,\mu$T had been reported [97], and $76\,\mu$T for the tetragonal one [94]. Third, it had been stated that, possibly due to disordered growth, variations in particle size, EPR line width, and oxygen sensitivity could be observed from batch to batch of preparation or recrystallization of LiNc-BuO [94].

3.6.2.2 Attempts to optimize the NP preparation process

In close cooperation with Sebastian Beck (Prof. Dr. Karsten Mäder, Martin-Luther-Universität Halle-Wittenberg, Halle (Saale), Germany), several attempts were made to reproducibly avoid the occurrence of a second EPR species. Further details can be found in his Diploma thesis [173].

For instance, the LiNc-BuO concentration was changed by either varying the amount of spin probe itself ($0.75\,$mg to $1.5\,$mg LiNc-BuO dissolved in $0.5\,$ml THF) or by varying the volume of THF ($1\,$mg LiNc-BuO dissolved in $0.2\,$ml to $2\,$ml THF). The size of the resulting NPs could be controlled, *i.e.*, increasing concentrations of LiNc-BuO in the organic phase led to bigger particles. Also the absolute EPR line widths could be influenced, however, the EPR spectra always showed a superposition of at least two species. The velocity and smoothness of injecting the organic phase into the aqueous phase might have been considered as the critical step of the nanoprecipitation method in the beaker. It was assumed that small deviations in the preparation process might have contributed to the irreproducibility of the results. But even when extremely different injection velocities ($0.5\,$ml in $0.5\,$min to $5\,$min) were tested, the influence on the size and EPR properties of the NPs was negligible. Moreover, the position of injection was irrelevant as long as the organic phase had not just been dropped onto the aqueous phase.

To exclude a negative impact of interactions with the stabilizer, PVA and polysorbate 80 were tested as alternatives. While the deployment of polysorbate 80 resulted in an undesired bimodal particle size distribution, PVA was suitable to prepare monomodal particles as well. However, the EPR properties were not affected positively.

Some NP dispersions were prepared or tempered (a few minutes to several hours) at low (on ice) or high temperatures ($50\,°$C to $80\,°$C). The idea was to provoke conversion

into a certain polymorph. Aside from that, NPs were subjected to isostatic high pressure (3000 bar to 8000 bar). The second EPR species did not vanish, though. Hence, either the process conditions were insufficient to induce conversion of the modification or this might be a hint that polymorphism was not the reason for the occurrence of two EPR species.

Further, THF was added to the aqueous phase in order to slow down the diffusion velocity of THF into the aqueous phase, and hence, the crystallization process in order to prevent disordered growth of the nanocrystals. This approach was expected to be useful to further control the particle size of the NPs. 10 % to 40 % of water were replaced by THF. Additionally, the impact of an addition of LiCl to the aqueous phase was investigated (6.5 mg to 147 mg in a mixture of 1 ml THF and 4 ml water). LiCl was added in order to avoid leakage of Li^+ ions from the LiNc-BuO crystals. Possibly, the leakage could not only have been caused by simple diffusion. Li^+ ions as hard acids are known to form complexes with water and THF as hard bases due to electrostatic metal-ligand interactions [174]. But there is another effect, which probably had an influence. Even at low concentrations of salts like LiCl, NaCl, or $CaCl_2$, THF is salted out from the aqueous solution causing seperation into two liquids [175]. THF is thus dehydrated and enriched in the vapor phase. Thus, the diffusion velocity of THF into the aqueous phase might have been elevated. For the first time, the EPR spectra could be influenced in terms of the intensity proportions of each species as well as their line widths. Unfortunately, the EPR spectra were still composed of at least two species.

The salting out effect had also been applied later in order to prepare LiNc-BuO nanocrystals via an emulsion/solvent evaporation technique using a microfluidic device, namely a hydrophilic droplet junction chip. According to the manufacturer's data sheet, these chips are designed for generating monodisperse emulsion droplets. There are two separate droplet junctions on the chip: T- and X-junction, where the alphabetic character discloses the geometry of the junction. Here, the cross-flow type T-junction was used. PVA served as the stabilizer in the aqueous phase (2 %). The resulting o/w emulsions were fed into a round bottom flask containing water, where the salt concentration was lowered immediately, THF diffused into the water phase, and finally, LiNc-BuO precipitated. Using this method, it was possible to obtain LiNc-BuO nanocrystals. On variation of the flow rates, the particle sizes could be changed. However, the size distribution was bimodal and the EPR spectrum exhibited two species as well. In another trial, dichloromethane was used as an alternative solvent to form an emulsion. In this case, LiNc-BuO precipitated when dichloromethane was evaporated under reduced pressure. The particles obtained by this method were in the size range of several micrometer, though. At least, the occurrence of diamond-shaped crystals could be proven microscopically, which had been described for the tetragonal polymorph [94].

Contrary to Pandian *et al.*, who observed that the pH value of the medium in the range of 2 to 10 had no effect on the EPR sensitivity to oxygen [97], there were certain hints that LiNc-BuO was unstable in aqueous media. To investigate this, NPs were prepared at different pH values, namely at pH 2, 4, 8, 10, and 12. Lower pH values were adjusted with HCl, higher pH values using a NaOH solution. It was found that the EPR signal intensity was decreasing with increasing pH value. Further, the colors of the NP dispersions were different: Starting from yellowish-brown at pH 2 over brown (pH 4) to yellowish-green (pH 8), and finally, to intensively green at pH values 10 and 12. The UV/Vis/NIR spectrum of the yellowish-brown NP dispersion contained a significant band at 864 nm that most likely belonged to Nc-BuO, which showed a strong Q band at 865 nm [94]. In contrast, the UV/Vis/NIR spectra of the green dispersions complied with the spectrum of LiNc-BuO very well. Apparently, LiNc-BuO readily decomposed in protic solvents to its precursor, the metal-free Nc-BuO. Hence, the final attempt was to conduct the first step of LiNc-BuO NP preparation anhydrously in aprotic solvents. For that purpose, a non-solvent of LiNc-BuO was needed, which was miscible with THF and water. Further, the solvent should be characterized by a high vapor pressure to be completely removed under vacuum. Acetone met these criteria, but needed to be dried priorly. A solution of LiNc-BuO in THF (1 mg in 0.5 ml) was injected into 5 g acetone. Subsequently, a solution of PVA 0.1 % in water 5 g was added and the organic solvents were removed under reduced pressure. Finally, the resulting EPR spectrum could be well simulated by only one species, albeit the line widths were very broad with approximately 560 µT to 740 µT. Interestingly, these values lie in the range found for the molecular form dissolved in THF or dichloromethane (3.5.3.2). Possibly, here lies the key to success, but there is still need for optimization: The line width should be narrower to yield higher SNRs and there was uncontrolled precipitation of LiNc-BuO on the stirring bar, which should be prevented.

3.6.3 Conclusion and outlook

To sum up, all attempts failed to produce more or less monodisperse LiNc-BuO nanocrystals in the submicron range exhibiting a narrow single line EPR spectrum with linear response to oxygen. Even controlled process conditions using a microfluidic device were incapable of reproducibly preparing NPs with the desired properties. Whereas the particle sizes of the NPs were overall satisfying, the EPR spectrum often showed a superposition of at least two species. The reason for that remains uncertain, similar to the LiNc-BuO microcrystalline powder of batch 2 (section 3.5.3). Occasionally, there were encouraging results, *i.e.*, only one species had been found. However, either this could not reliably be reproduced or, in case of anhydrous production, the lines were very broad.

However, the number of parameters in this set of experiments was quite limited due to a lack of both, time and LiNc-BuO substance. Consequently, the feasibility of LiNc-BuO nanocrystal preparation cannot be assessed conclusively. A thorough screening of excipients and various preparation conditions is needed, in particular for microfluidics. An anhydrous preparation process might be useful and, possibly, be transferred to a microfluidic preparation method. Alternatively, if nanomaterials are desired, nanofibers might be a promising approach as well [142]. Unfortunately, in this publication it is not stated how they dealt with the complex recrystallization process of LiNc-BuO or whether its EPR characteristics were reproducible. However, most of all, it is strongly recommended to use well defined and purified LiNc-BuO powder, since finally, there is only one explanation left: Due to impurities of both batches of LiNc-BuO, the (re-)crystallization process as well as the accessibility of the surface areas or the inner microchannels for oxygen and other gases might have been affected.

3.7 MPs

The results presented in the following sections emerged from a close collaboration with Prof. Dr. Oliver Thews and his group and have partly been published in "Injectable LiNc-BuO loaded microspheres as in vivo EPR oxygen sensors after co-implantation with tumor cells." by Frank et al. [151].

In section 3.6, it was demonstrated how difficult it was to nanoformulate LiNc-BuO reproducibly. NPs certainly impress with their ability of being administered intravenously. They are able to distribute in the tissue of interest giving the opportunity of spatial resolved oxygen measurements until they are eliminated. Due to the abnormal tumor physiology and structure, which results in enhanced permeability of the vasculature and retention by an insufficient lymphatic system, also known as the EPR effect, NPs can passively be accumulated in tumors [176]. However, it was questionable if the amount of spin probe passively accumulated would have been high enough to obtain a sufficiently good SNR for oxygen determination. In this case, a formulation as polymeric MPs was advantageous since the spin probe crystals did not have to be dissolved or comminuted during formulation preparation. As mentioned in section 3.5.1, the particle size of LiNc-BuO crystals was $1\,\mu m$ to $10\,\mu m$, which allowed microencapsulation as a suspension. Thereby, the quality of the LiNc-BuO crystals was preserved. For the purpose at hand, MPs were just as applicable. Different tumor models should be investigated regarding their oxygenation

levels. In these preclinical studies, tumor cells had to be injected to induce tumor growth anyway. Thus, no additional invasive intervention was needed as MPs could be implanted simultaneously. Since PVAc had already been successfully used to nanoencapsulate trityl radicals (section 3.3), the same polymer was used here. For the preclinical investigation of oxygenation levels in tumors, there was no need to eliminate or surgically retrieve the particles after the measurements. The average duration of such experiments, from tumor inoculation to the measurements, was only one to several weeks. After that, the animals were sacrificed anyway. So, it was well acceptable that PVAc was non-biodegradable. Instead, a release of the spin probe and contact with the tissue was prevented.

3.7.1 Formulation development

Several methods are available for the preparation of drug loaded MPs. Traditional techniques include phase separation, also known as coacervation, emulsion/solvent evaporation and/or solvent extraction with simple set ups, as well as spray-drying and spray-freeze-drying [177]. By adjusting preparational parameters, the properties of the resulting MPs can be influenced stupendously. However, more sophisticated methods such as ultrasonic atomization, electrospraying, and microfluidics certainly are advantageous as they yield monodisperse particles and can be employed continuously [178]. In this case, the proof of principle had not been demonstrated yet. To the author's knowledge, LiNc-BuO and related radicals had never been microencapsulated before. Therefore, it was first necessary to establish an expedient preparation technique and examine the applicability of the MPs as oxygen sensors. A target particle size range of $10\,\mu m$ to $100\,\mu m$ was sufficient, monodisperse particles were not necessary. Thus, a traditional emulsion/solvent evaporation method was chosen, which convinces due to its simplicity [165]. It only requires a minimum of instrumental equipment and mild conditions such as ambient temperature [179]. According to a review article of Arshady, the underlying method had first been mentioned and patented in 1970 by Vrancken and Claeys and employed by Beck *et al.* in 1979 to prepare polylactide MCs [180–182].

The method of emulsion/solvent evaporation involves three processes: Initial droplet formation, droplet stabilization, which is usually supported by a stabilizer, and droplet hardening [180]. The preparative steps are the following. In brief, a polymer is dissolved in a volatile organic solvent. The drug is added to form a solution, an emulsion, or a suspension. In presence of a suitable emulsifying agent, the mixture is then emulsified in a non-solvent of the polymer and the drug, which is immiscible with the organic solvent. Subsequent evaporation of the organic solvent results in the solidification of drug loaded MPs, which are then washed, collected, and dried [164, 183].

At a first glance, some details of the specific method used in this work, which is depicted in figure 3.23, might not be obvious to the reader. The solvents employed are not state of the art, yet expedient. Therefore, some underlying reasons and aspects of the formulation development are discussed in this section. As mentioned before, it was important to avoid dissolution of the spin probe crystals during MP production to retain the quality of the LiNc-BuO crystals. Therefore, solvents were discovered, which dissolved the polymer PVAc, but not the spin probe (section 3.5.2). For encapsulation of hydrophobic compounds such as LiNc-BuO, usually o/w methods are used to achieve high encapsulation efficiencies [164, 165]. The typical solvent dichloromethane was impractical since LiNc-BuO was slightly soluble. Thus, ethyl acetate had been tested in pretrials, although LiNc-BuO possibly showed some solubility tendencies. It was found that the crystal quality was preserved. However, this method failed for PVAc as a polymer. MPs showed aggregation during the filtration and drying process. When the intermediate particles were examined microscopically, this process could be observed as well. As soon as the water evaporated, the particles coalesced. This process seems comprehensible knowing that PVAc is one of the most important polyvinyl ester adhesives. Upon evaporation of water, the swollen particles aggregate to form a coherent adhesive film.

Consequently, a non-aqueous method was sought, which was operating without dichloromethane. Early research from Tsai *et al.* in 1986 already mentioned an o/o, sometimes also referred to as w/o, method using acetonitrile as the dispersed and paraffin as the continuous phase, yet without further technical details [184]. They incorporated a water-soluble drug into poly(L-lactic acid) (PLA) MCs. Jalil and Nixon returned to this method in 1989 and 1990 and reported on preparative variables affecting the properties of PLA MCs [183, 185]. At the same time, Hyon and Ikada patented an o/o (w/o) method for microencapsulation by polymers of the PLA type [149, 186]. The method was actually invented for water-soluble drugs to enhance their encapsulation efficiency in comparison to (w/)o/w methods, where they tend to diffuse out into the continuous phase. They described the use of a hydrophilic organic solvent, which is well miscible with water but immiscible with a hydrophobic poor solvent of the drug and the polymer. The hydrophilic solvent is emulsified with the hydrophobic one using nonionic surfactants with a hydrophilic lipophilic balance (HLB) of 3 to 6.5 at concentrations of preferably 1 % to 3 %.

Based on this general method, the water-free (solid-in-)oil-in-oil (s/)o/o emulsion solvent evaporation method illustrated in figure 3.23 was developed. Except that an acetonitrile/paraffin system was employed and the MPs were washed with *n*-hexane, the preparation process only had limited comparability with the methods originally reported by Tsai *et al.* or Jalil and Nixon. The proportion of ingredients as well as various technical parameters had to be modified to establish optimal conditions for the formulation of
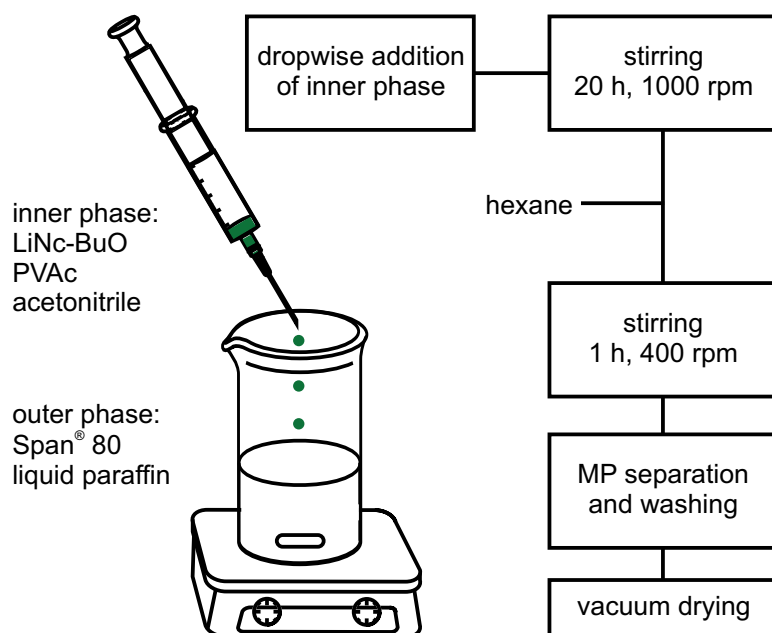
Figure 3.23: Steps of MP preparation by use of an (s/)o/o emulsion/solvent evaporation method.

the individual drug/polymer system. For instance, heating was avoided to not exceed the T_g of PVAc and, thus, avoid aggregation [187]. As a consequence, the evaporation process was decelerated. The method developed was not only suitable to prepare PVAc MPs successfully, it also provided favorable conditions for LiNc-BuO. As described in section 3.5.2, LiNc-BuO was practically insoluble in both acetonitrile and liquid paraffin, but slightly soluble in *n*-hexane. Thus, washing with the volatile solvent *n*-hexane did not only remove residues of the surfactant as well as the highly viscous paraffin to enable filtration and harvest of the MPs. It also dissolved debris of non-encapsulated spin probe crystals. Preparation parameters were adjusted to obtain MPs with an optimized particle size distribution and crystal load as discussed in the following paragraphs.

Concentration of surfactant in continuous phase

Jalil and Nixon described the impact of emulsifying agent concentration on the size of the MPs in an acetonitrile/paraffin system by means of Span® 40 and 65 [183]. From 1 % to 2 %, the mean volume diameter decreased sharply, but little change was observed above 2 %. This was contributed to the fact that at a certain concentration, the packing of emulsifier at the surface of the emulsion droplets reaches its optimum. Adding more surfactant will not give added protection against droplet coalescence if the excess remains in the continuous phase mainly. On the other hand, Iwata and McGinity pointed out that the encapsulation efficiency might be reduced with increasing surfactant concentration due to enhanced solubilizing properties of the continuous medium [188]. Below 0.25 % of Span®

(a) Volume weighted particle size distributions of MPs as obtained by SLS.

(b) Yields, encapsulation efficiencies, and crystal loadings of MPs.
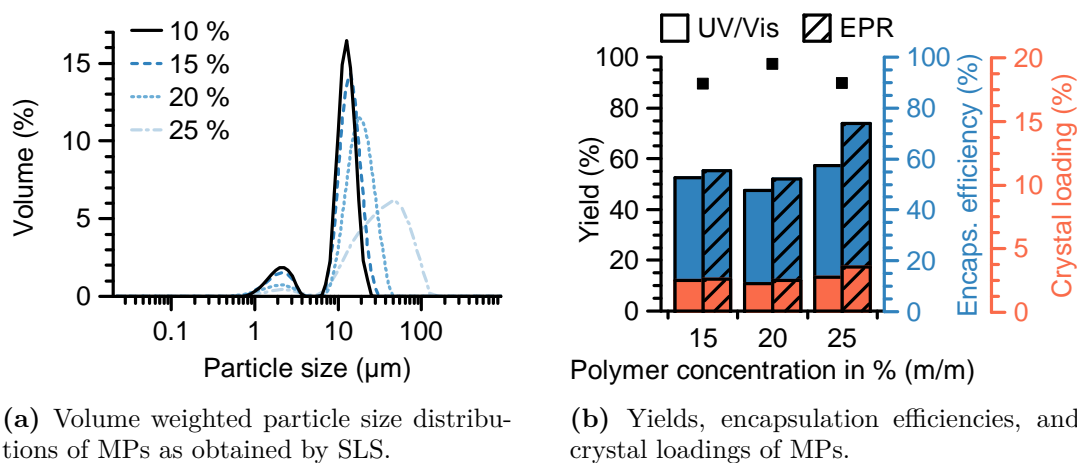
Figure 3.24: Influence of varied concentrations of PVAc in acetonitrile (in %, m/m) on resulting MPs. The spin-probe-to-polymer ratio was kept constant at 1:20 (m/m).

80, they observed agglomeration. Eventually, a concentration of 2 % (m/m) Span® 80 was chosen according to various literature reports [149, 183, 185, 187, 189, 190]. In section 3.5.2, the solubility of LiNc-BuO in paraffin was tested with and without the addition of 2 % (m/m) Span® 80. The mixtures were comparable in their intensities of coloration meaning that the solubilizing properties had not been altered perceptively.

Agitation rate

In pretrials, the rotational frequency during addition of the inner phase was varied from 750 rpm to 1500 rpm (according to a relative centrifugal force of approximately 24 g to 96 g at r_{max}). As expected from literature reports, both the particle size and the encapsulation efficiency decreased with raising rotor speed [183, 191]. Above 1000 rpm, the encapsulation efficiency further decreased, but the particle size could not be reduced drastically anymore. As a compromise, MPs were subsequently prepared at 1000 rpm.

Polymer concentration

The polymer concentration in the inner phase was increased from 10 % to 25 %. Thereby, the encapsulation efficiency usually was improved if only slightly [179, 192]. The higher viscosity of the internal phase probably impedes drug crystals penetrating the polymer phase [165]. With the data at hand this relationship could not be proven (figure 3.24b). However, the particle sizes and the width of the particle size distributions increased dramatically with polymer content (figure 3.24a) since highly viscous droplets tend to coalesce more readily than they re-divide [180]. At very low polymer concentrations, the entrapment efficiency was decreased drastically, such that the majority of MPs did not contain

(a) Volume weighted particle size distributions of MPs as obtained by SLS.

(b) Yields, encapsulation efficiencies and crystal loadings of MPs.
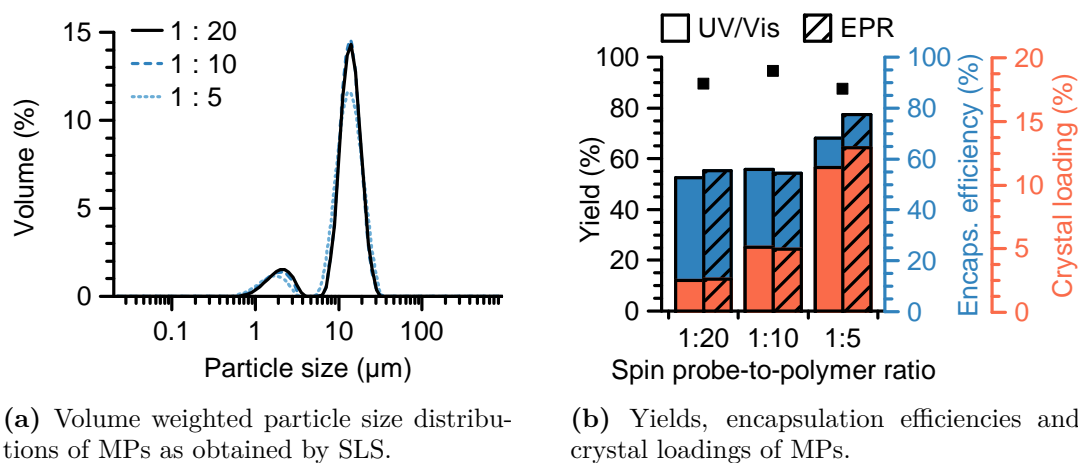
Figure 3.25: Influence of spin probe-to-polymer ratio (m/m) on properties of the resulting MPs. The concentration of PVAc in acetonitrile was kept constant at 15 % (m/m).

any spin probe crystals at all. MPs were too small to be collected with the method used for preparation. Hence, the MP yield was very low and a physicochemical characterization of the residual MPs seemed to be meaningless. So, the optimized polymer concentration in this experimental set up was determined by the size rather than the entrapment efficiency. The optimal PVAc concentration was found to be 15 % PVAc in the internal phase. It must be stated, though, that the results at hand could not be proven statistically. Since LiNc-BuO was poorly accessible and fairly expensive, the number of experiments was kept at a minimum. In pretrials, different batches of MPs were tested *in vivo* and no impact of the MP size on the tumor growth rate was found (data not shown). Hence, batches prepared with other polymer concentrations could also be applied successfully.

Spin probe-to-polymer ratio
The initial ratio of spin probe to polymer in the internal phase was raised from 1:20 to 1:5 (m/m), *i.e.*, 4.8 % to 16.7 % (m/m) spin probe in PVAc. Thereby, the entrapment efficiency could be increased from 53 % (measured by UV/Vis spectroscopy)/55 % (determined by EPR spectroscopy) to 68 % (UV/Vis)/78 % (EPR) (figure 3.25b). The particle size as well as the particle size distribution were comparable meaning that the amount of entrapped spin probe did not affect the particle size (figure 3.25a). However, again, the results could not be proven statistically. Zhu *et al.* also reported an increase of the entrapment efficiency on increased drug-to-polymer ratio up to a certain point [191]. They did not observe an impact on the particle size either. In the end, the spin probe-to-polymer ratio was chosen according to the target drug load of the MPs. Since a high entrapment was desired, a ratio of 1:5 was favored.

Conclusion

During MP formulation development, both the crystal loading as well as the encapsulation efficiency were optimized. Thus, the maximum SNR was achieved and the substance loss during production was minimized. The encapsulation efficiency was usually 60 % to 70 % (m/m). In general, a high yield of 85 % to 95 % was achieved. Typical MPs used for further experiments contained 5 % to 10 % (m/m) spin probe.

3.7.2 Physicochemical characterization of optimized MPs

MPs were examined microscopically (figure 3.26) to assure that no bubbles were trapped, which could have acted as a gas reservoir and affect the oxygen measurements [113, 136]. Microscopic images showed microspheres with dark green incorporated LiNc-BuO crystals. The particles were spherical in shape and the spin probe crystals were well distributed inside the bigger particles. However, there was a minor population of smaller particles without any spin probe crystals. Particle size measurements by SLS confirmed that the size distribution was bimodal (figures 3.25a and 3.24a). However, the volume fraction of smaller particles was low.

MPs were also investigated fluorescence microscopically using a blue filter set. The emission filter was capable of transmitting the signal from green, yellow, and red fluorophores having absorption bands in the central blue wavelength region.

(a) MPs prepared with 20 % (m/m) PVAc in acetonitrile.

(b) MPs prepared with 15 % (m/m) PVAc in acetonitrile.
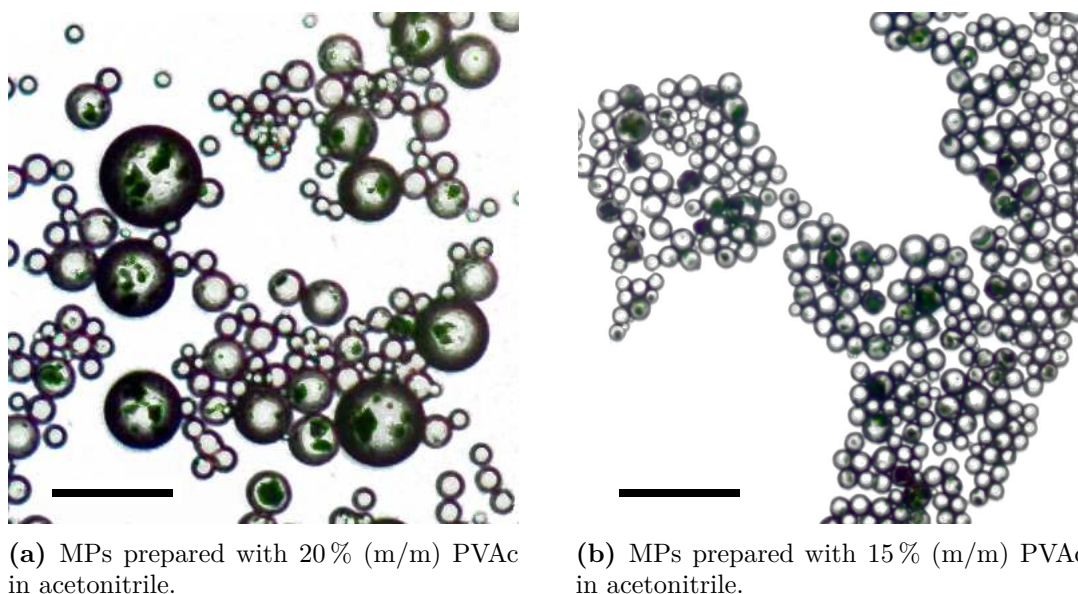
Figure 3.26: Microscopic images of MPs (bar size: 50 µm). Embedded LiNc-BuO crystals appear as dark green spots.

(a) Fluorescence microscopic image of pure LiNc-BuO crystals.

(b) Fluorescence microscopic image of pure PVAc MPs without LiNc-BuO.

(c) Fluorescence microscopic image of PVAc MPs containing embedded LiNc-BuO.

(d) Microscopic image of PVAc MPs containing embedded LiNc-BuO.
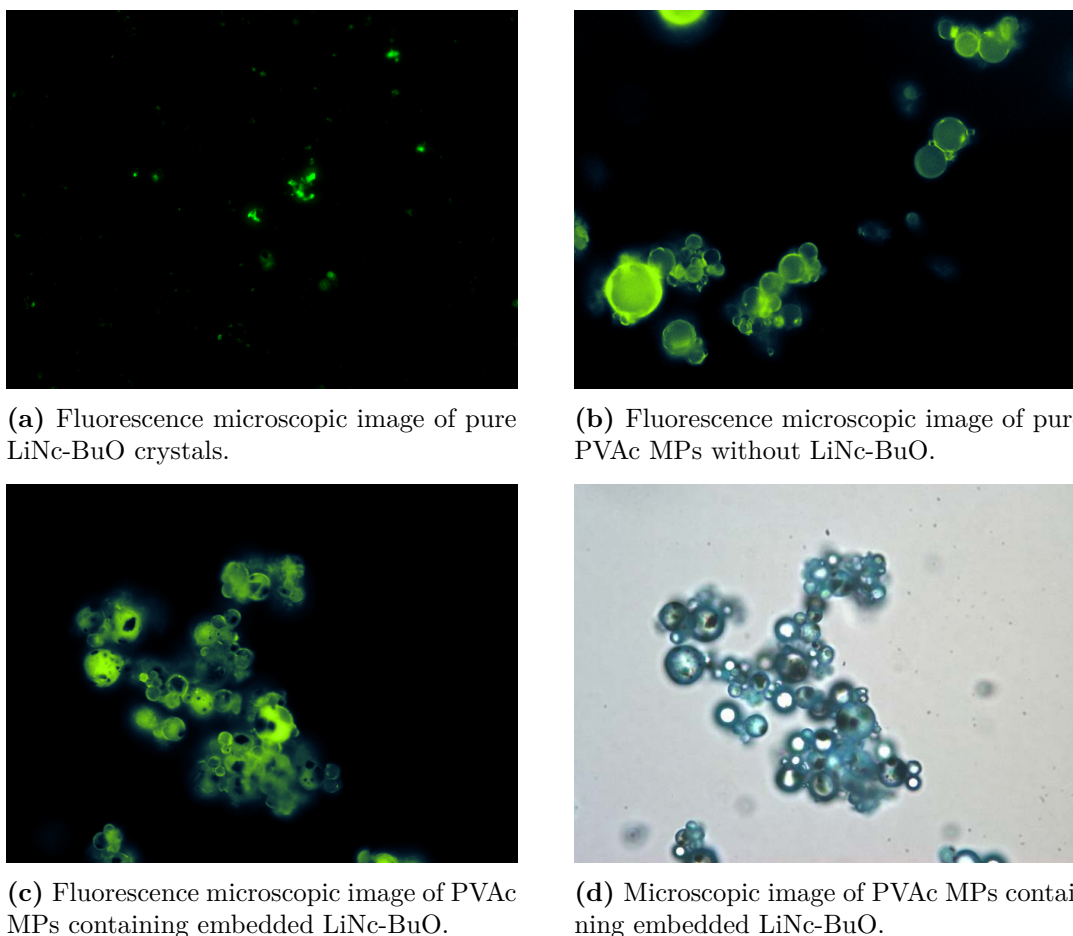
Figure 3.27: (a)-(c) Fluorescence microscopic investigations of LiNc-BuO and MPs. (d) Same section as in (c), but viewed in bright-field mode.

Not only LiNc-BuO crystals showed fluorescence (figure 3.27a). Fluorescence microscopic images of MPs without incorporated LiNc-BuO revealed that PVAc itself was fluorescing (figure 3.27b). Unfortunately, LiNc-BuO and PVAc had similar excitation and emission profiles. When LiNc-BuO crystals were incorporated, they appeared as non-fluorescing dark spots in the fluorescing MPs (figure 3.27c). The locations of the dark spots were congruent with the locations of LiNc-BuO crystals in the corresponding bright-field microscopic image (figure 3.27d). Possibly, light emitted by embedded LiNc-BuO crystals was immediately absorbed by the surrounding PVAc. Therefore, attempts to distinguish both signals failed. The spectrum of PVAc was used for unmixing (figure 3.28). This fluorescing property of the MPs was useful, for instance, to securely identify MPs in tumor tissue *ex vivo* by comparison of bright-field and fluorescence microscopic images of
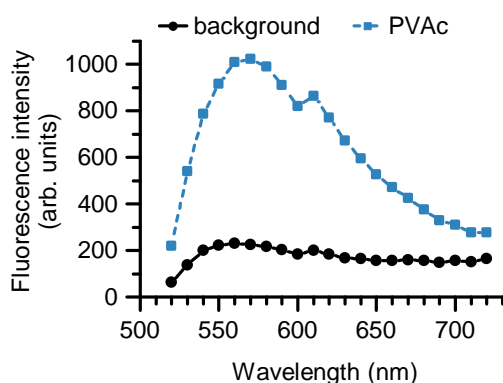
Figure 3.28: Fluorescence emission spectrum of PVAc.

tumor slices. It might as well be utilized to investigate the distribution of PVAc MPs – and probably also NPs – in certain tissues by fluorescence imaging. However, admittedly, an emission of yellowish green light is unfavorable for *in vivo* applications.

3.7.3 Oxygen response

The EPR line width of the MPs with incorporated LiNc-BuO increased linearly with the pO_2 (figure 3.29a). The corresponding EPR spectra under anoxic ($\Delta B_{PP} = 7.2 \, \mu T$) as well as normoxic conditions ($\Delta B_{PP} = 96.1 \, \mu T$) are shown in figure 3.29b. The slope of the curve, which reflects the oxygen sensitivity, was slightly lower for dry MPs ($0.60 \, \mu T/mmHg$) compared to non-encapsulated dry LiNc-BuO crystals ($0.69 \, \mu T/mmHg$). Probably, the
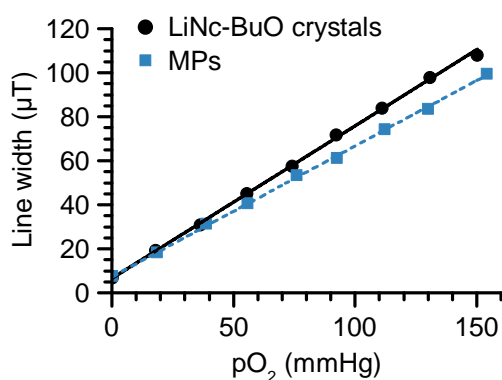
(a) Oxygen calibration curves of MPs with an oxygen sensitivity of $0.60 \, \mu T/mmHg$ compared to non-encapsulated LiNc-BuO crystals with $0.69 \, \mu T/mmHg$ (mean, $n = 3$, lines: linear regressions).
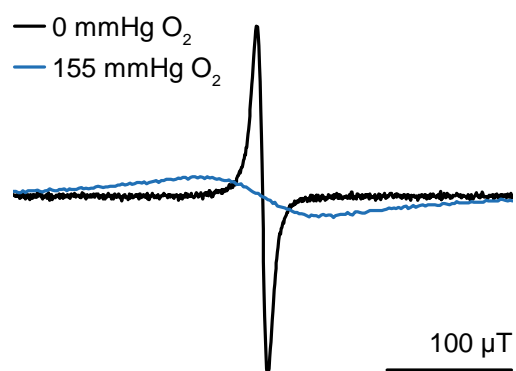
(b) EPR spectra of MPs. The estimated line widths were $96.1 \, \mu T$ under aerobic and $7.2 \, \mu T$ under anaerobic conditions.

Figure 3.29: Oxygen response of dry MPs.
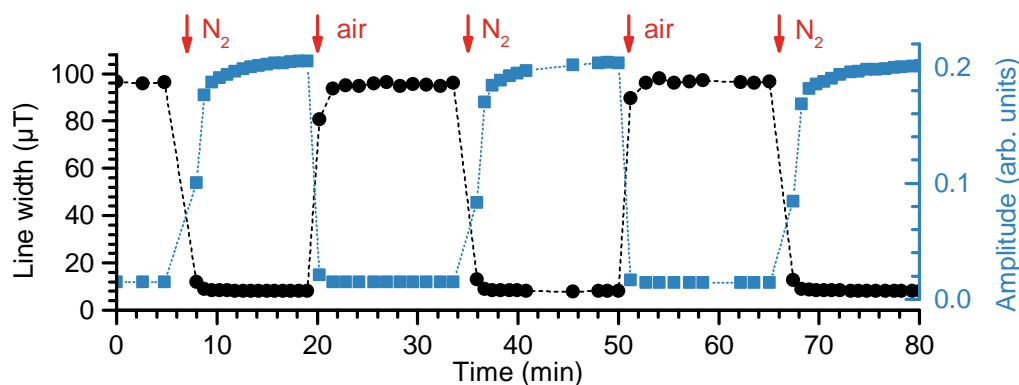
Figure 3.30: Kinetics of equilibrium after change from air to nitrogen and vice versa as measured by EPR spectroscopy.

crystalline structure or size and, thus, the oxygen sensitivity [94] of the spin probe crystals were marginally altered during the MP preparation, probably when the spin probe crystals were desagglomerated in acetonitrile (figure 3.23). Also an impact of PVAc cannot be excluded. Eteshola *et al.* incorporated LiPc in PVAc. The mean oxygen sensitivity of polymer-embedded LiPc was found to be slightly decreased in comparison to uncoated LiPc, albeit with the data basis they had, a significance of the observed difference could not be proven [123]. However, the oxygen response of the MPs was linear and the sensitivity was in the range reported for pure LiNc-BuO crystals [94, 97] (section 3.5.4). Hence, the MPs were well useable for EPR oximetry experiments.

As can be seen in figure 3.30, the changes in the line width were highly reversible meaning that there was no binding of oxygen or chemical alteration of the spin probe due to oxygen. The response time of the EPR signal of the MPs after switching from air to nitrogen or vice versa was approximately 2.5 min. After this time, a change in the line width could not be detected anymore although the amplitude was still slightly changing. For non-encapsulated LiNc-BuO, very fast response times of <1 s to 3 s have been reported [58, 193]. There might have been some delays due to the simple experimental setup at hand. However, the response of the MPs was definitely prolonged, probably because oxygen needs to diffuse through the polymer before encountering the spin probe crystals [137]. Thus, if a very fast response and recovery is needed in rapidly changing systems, nanofibers might be a better approach [142]. However, the response time of the MPs was adequate for the *in vivo* experiments at hand. It was comparable to other formulations described in the literature, for instance, LiNc-BuO in PDMS chips [137] or LiPc in PTFE implants [113, 136]. All in all, MPs enabled accurate and sufficiently fast EPR oximetry measurements over a broad measurement range rendering them suitable for *in vivo* oximetry.

3.7.4 Storage stability

(a) LiNc-BuO.

(b) MPs.
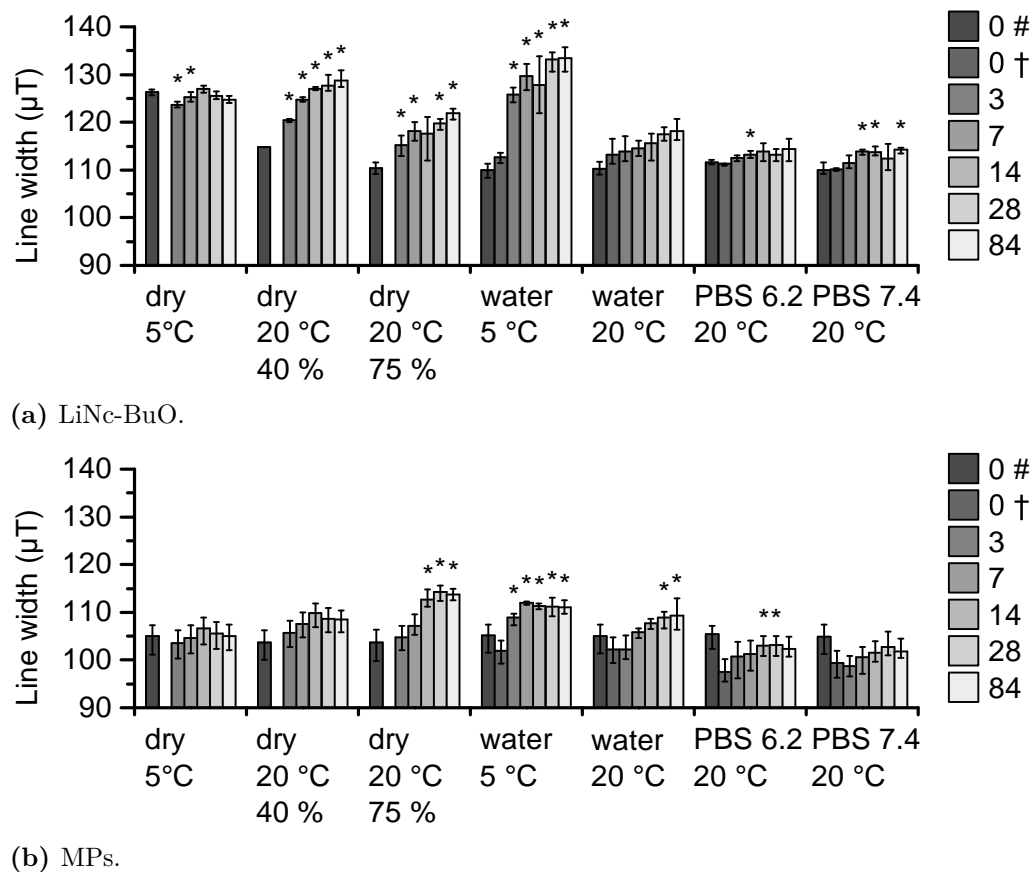
Figure 3.31: Stability testing of non-encapsulated LiNc-BuO crystals as well as MPs with entrapped spin probe: EPR line widths on days of storage under various conditions (dry/wet, different temperatures and relative humidities, see table 2.5). Note that the aliquot for stability testing of LiNc-BuO as dry crystals at $5\,°C$ had not been taken simultaneously with the others. Therefore, the sample might have had slightly different crystal properties or particles sizes and, hence, a broader line width. It is recommended to consider relative changes in one sample rather than the exact absolute values. Statistical significance (indicated by *) of the differences was assessed by paired Student's t test referred to day 0 # or day 0 †, if available (#: Dry crystals/MPs before addition of fluids, †: wetted crystals/MPs after addition of fluids, measurements were conducted in air, $n = 3$).

The stability of the EPR line width of MPs in comparison to pure LiNc-BuO crystals, as depicted in figure 3.31, was tested under various conditions (table 2.5). It was obvious that the line widths of the MPs were narrower than those of the pure spin probe, which was in accordance to the results described in section 3.7.3. The narrower line width under air conditions goes along with a lower oxygen sensitivity. Fortunately, when dry LiNc-BuO

powder or dry MPs were stored in the fridge (dry, 5 °C), the EPR line widths were stable over time. It is conspicuous, however, that a storage of the dry LiNc-BuO powder under ambient conditions (dry, 20 °C, 40 %) as well as elevated humidity (dry, 20 °C, 75 %) led to an increase in the line width. The same happened with a dispersion of LiNc-BuO in water stored in the fridge (water, 5 °C), whereas the line widths were not significantly increasing when the dispersion was stored at room temperature (water, 20 °C). The results of storage in buffer (PBS 6.2/PBS 7.4, 20 °C) were ambiguous: There was no distinct tendency.

Possibly, there were some interactions with water molecules at the surface or in the microchannels of the crystals. These processes might have been reversible, which had not been tested. These findings were contradictory to the literature: Pandian *et al.* stated that the line width of LiNc-BuO particulates was not affected in aqueous dispersion media (water, PBS, cell culture media) [97]. It was assumed that by incorporation into MPs, these line width changes could be prevented. Indeed, the line width changes of MPs appeared to be less pronounced. Hence, coating of LiNc-BuO improved its stability. Smaller deviations might be attributed to the fact that the measurement conditions on different days were probably not exactly the same, for instance, the temperature, the pressure, and the oxygen content inside the sample vials, which had intentionally not been controlled in this experiment. The measurements should not be disturbed by flushing the samples. Due to the air flow, water molecules possibly adsorbed at the surface or diffused into the microchannels could have been displaced. Further, it must be noted that the statistical power was too low to make reliable statements.

Additionally, the linearity of the oxygen response of both pure LiNc-BuO crystals and MPs was tested in PBS 7.4 on the day of preparation as well as up to six months of storage in the fridge. The oxygen sensitivities were slightly changed, which was expected from the different line widths under air conditions. The oxygen response, however, was still linear (data not shown here, it is referred to the appendix, figure A.8). Hence, after recalibration, LiNc-BuO and MPs were still usable as oxygen sensors. Alternatively, raw spin probe material as well as MPs were always stored in the fridge to ensure long term stability, and they were only redispersed just before usage.

3.7.5 Pilot study on sterilization

To sterilize the MPs, commonly used sterilization methods such as wet heat/autoclaving or dry heat could not be applied due to the high process temperatures. Softening and deformation of the polymer would lead to aggregation of the MPs. In fact, the stability of PVAc undergoing wet or dry heat sterilization was described as poor to fair [194]. Sterilization with ethylene oxide gas requires careful handling, and complete removal of residual

traces on the materials is difficult to achieve. Further, PVAc showed poor stability when sterilized with ethylene oxide [194]. In contrast, electron beam (β-) and gamma irradiation are well established methods for sterilizing polymer-based formulations. However, rather sophisticated and scarce equipment is needed. The stability of PVAc against radiation was described as good [194–196]. As an alternative, all substances used for preparation could have been sterilized by a suitable method and solutions could have been sterile filtered, respectively. All subsequent preparation steps would have required aseptic conditions. This method is fairly laborious. MPs were not routinely sterilized in this work, but one pilot study was performed. MPs with and without embedded LiNc-BuO as well as pure PVAc powder were sterilized with β- radiation. Before and after sterilization, LiNc-BuO loaded MPs were analyzed by EPR and UV/Vis spectroscopy, while SLS, DSC, and GPC measurements were performed on unladen MPs.

A creation of odor or changes in the optical appearance of MPs after sterilization were, if present, hardly noticeable. In particular, the evaluation of a possible discoloration was aggravated by the presence of incorporated LiNc-BuO due to its intense green color. An impairment of the wettability of the MPs could not be observed. However, the contact angle had not been determined. In figure 3.32a, the particle size distributions of three individual MP batches before and after irradiation are illustrated. As can be seen, the size distribution of unprocessed MPs was comparable to irradiated MPs.

The molar mass of PVAc (pure and formulated as MPs without spin probe) was determined by GPC. After sterilization of pure PVAc powder, both the weight averaged (M_w) as well as the number averaged molar masses (M_n) were reduced significantly. Before sterilization, M_w was 355 ku and M_n was 69 ku, whereas after irradiation, the values were 269 ku and 53 ku, respectively. On the other hand, filtration prior to the GPC measurements was harder when the samples had been irradiated. The PdI, which is the quotient M_w/M_n, was unchanged at 4.5. These results suggested that both crosslinking and degradation of the polymer chains took place with degradation as the probably dominating effect. The PdI remained unchanged indicating that chains were ruptured randomly. The degree of side chain degradation, which would have caused an undesired release of acetic acid [197], was probably low. In sterilized MPs, however, M_w was hardly changed (336 ku before and 333 ku after irradiation), while M_n was slightly reduced (83 ku before and 74 ku after irradiation). Consequently, the PdI increased from 4.1 to 5.1. M_n is more sensitive to chains of low molecular mass, and M_w to chains of high molecular mass. Thus, again, the predominant effect was chain scission suggested by the decrease of M_n. However, if compared to pure PVAc powder, M_w was hardly reduced. This might be attributed to a relative increase of crosslinking to chain scission. Hence, the distribution of molecular masses in the batch became significantly broader.
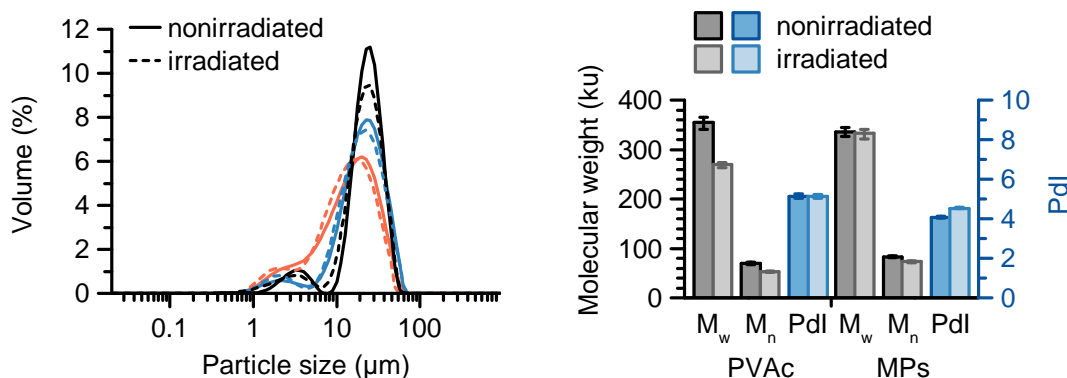
(a) Volume weighted particle size distributions of three individual MP batches before (solid lines) and after (dashed lines) irradiation as obtained by SLS. Note that MPs were prepared without LiNc-BuO and under slightly modified parameters, explaining variations in the particle size distributions.

(b) Results of GPC analysis of pure PVAc powder in comparison to MPs without embedded LiNc-BuO: Molar masses (M_w and M_n) as well as the resulting PdI of nonirradiated and irradiated samples ($n = 3$).

Figure 3.32: Impact of β^- irradiation on the size of MPs and the molar mass of PVAc.

To examine the impact of the molar mass change on the thermal behavior, pure PVAc powder and MPs were measured by DSC before and after sterilization. In principle, the shapes of the DSC curves were comparable, as can be seen in figure 3.33a. The curves showed a glass transition recognizable by a characteristic endothermic shift of the baseline with a step height of approximately $0.4\,\text{J/(g\,K)}$ to $0.5\,\text{J/(g\,K)}$. At this temperature, a polymer changes from a rigid glass to a fluid or rubbery state. However, particularly in the first heating curve, this process was superimposed by an endothermic peak, which was more distinct after irradiation of the polymer.

This endothermic peak, which appeared immediately after the glass transition, was attributed to a phenomenon called enthalpy relaxation. Glasses, which are thermodynamically non-equilibrium systems, undergo so-called physical aging, especially when stored at temperatures closely below T_g [198]. This relaxation process toward an equilibrium state is associated with an increase in density and a decrease in free volume and, hence, enthalpy of the material [199]. On heating of the aged polymer, the lost relaxation enthalpy is recovered, which can be seen as an endothermic peak in the DSC curve [198]. The area under the curve is a quantitative measure of the extent of aging. Hence, the aging process was accelerated during sterilization. The relaxation rate depends on the temperature relative to T_g. Thus, the temperature was probably elevated during irradiation to values close to T_g [198]. Additionally, β^- radiation itself might have induced rapid
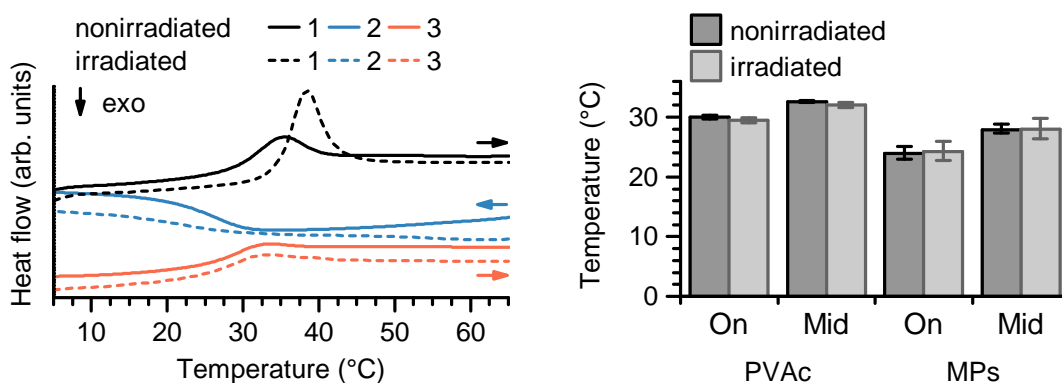
(a) Representative DSC thermograms of unprocessed and sterilized MPs: First (1) and second (3) heating curves were obtained at 10 K/min, cooling curves (2) at -10 K/min.

(b) Tg of PVAc (powder/MPs) before and after sterilization as determined from the second heating curves. Data reported as onset (On) and midpoint (Mid) ($n = 3$).

Figure 3.33: Impact of β^- irradiation on the thermal behavior of PVAc (as pure powder or formulated as MPs).

structural relaxation. Since physical aging is a reversible process, heating to above T_g erases the so-called thermal history of the material [199]. After subsequent cooling below T_g and reheating, T_g could be determined from the second heating curves. Small enthalpy relaxation peaks which reappeared possibly due to fast relaxation processes immediately below T_g, did not hamper the analysis.

T_gs obtained before and after sterilization are given in figure 3.33b. The incorporated spin probe possibly acted as a softener since the T_g of MPs was slightly lower. However, the mean T_gs of PVAc powder, 30 °C (onset)/32.6 °C (midpoint), and MPs, 23.9 °C (onset)/27.9 °C (midpoint), were not significantly changed after irradiation. That means that albeit the molecular mass was reduced, T_g of PVAc was not affected adversely.

The content of incorporated spin probe after sterilization was measured by UV/Vis and EPR spectroscopy and compared to unprocessed MPs. Any chemical modification accompanied with the loss of the radical nature of the spin probe would have been detectable with both methods. Since the desired radical LiNc-BuO is distinguished by its intense green color, a chemical reaction could have been noticed by an alteration in the absorbance of light in the UV/Vis region (see UV/Vis/NIR spectra of LiNc-BuO and its precursor Nc-BuO, figure 3.15). Further, a decomposition of the radical would have led to a decreased EPR signal intensity.

Neither of both methods proved a significant change in the crystal load of MPs after irradiation (figure 3.34a). This was in accordance with the literature, where LiNc-BuO
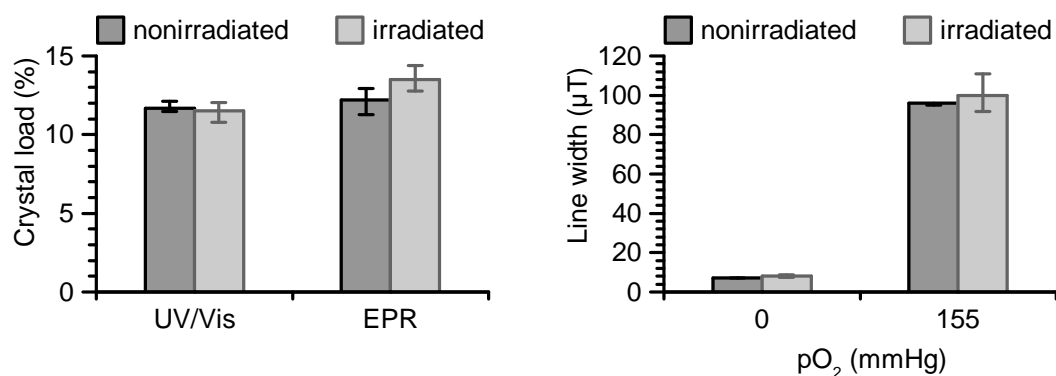
(a) Crystal load of MPs as determined by UV/Vis and EPR spectroscopy.

(b) Comparison of EPR line widths in nitrogen as well as in air.

Figure 3.34: Impact of β^- irradiation on the EPR properties of MPs ($n = 3$).

particulates had been treated with 15.5 kGy of Cobalt-60 gamma radiation for 10 min and no effect on the EPR properties of the particulates was found [97]. Although most likely radicals had been generated during β^- irradiation, they did not react with or affect the incorporated LiNc-BuO radicals. On the other hand, even if long-lasting radicals were still present during the subsequent EPR measurements, they did not significantly impact the EPR spectrum of LiNc-BuO. Both the line shape and the signal intensity were inconspicuous.

Moreover, the EPR line widths under anoxic and normoxic conditions were comparable to the values obtained before sterilization (figure 3.34b), suggesting that the oxygen sensitivity was unchanged and possible crosslinking did not impact the oxygen permeability of the polymer adversely.

To sum up, the β^- irradiation has shown its usefulness to sterilize LiNc-BuO loaded PVAc MPs. Molecular changes in the polymer did not adversely affect its material properties nor impede a further use of the MPs. However, to reduce these undesired effects of irradiation, the experiment could be repeated in inert (anoxic) nitrogen atmosphere and at lower temperature. PVAc might additionally be stabilized by suitable excipients. Most importantly, there was no evidence that this process had a negative impact on the EPR signal of embedded LiNc-BuO nor its oxygen sensing properties. However, as already mentioned, the effort of this method was rather high. However, MPs were only injected intramuscularly or subcutaneously, but not intravascularly. The animals were immunocompetent. Moreover, since organic solvents were used, the preparation was non-aqueous, and the MPs were stored as dry particles in the fridge, the bioburden most likely was low, anyway. Thus, it was reasonable to use non-sterilized MPs in further experiments.

3.7.6 *In vivo* stability of the oxygen response

Particulate spin probes are generally less affected by physiological oxidoreductants than soluble probes, and, hence, less quickly converted into diamagnetic species. However, when these probes are administered *in vivo* as pure crystals, they might loose their oxygen responsive behavior as well. Encapsulation was a promising approach to overcome these problems: Reactions with tissues might be reduced and the physical stability of the sensors can be increased when incorporated into a polymer.

To examine the long-term persistence of the oxygen responsive behavior, the MPs were implanted into SKH1-Hr^{hr} mice. One batch was implanted subcutaneously into their flank and another one intramuscularly into their thigh muscle. The mice were chosen with respect to their immunocompetence, so that immunological responses, if occurring, could be noticed and evaluated. Further, their hairless nature facilitated the optimal alignment of the surface coil. Thereby, positioning of the mice in the EPR spectrometer was accomplished as invariable as possible. Two weeks as well as up to six months after implantation of the MPs, the pO$_2$ at both implantation sites was assessed EPR spectroscopically under normoxic conditions as well as after 10 min of inspiratory hyperoxia. The duration of the hyperoxic challenge was possibly not long enough to reach maximum levels of pO$_2$ in the tissues, which would have required approximately 40 min [200]. However, it was sufficient to obtain significantly elevated oxygenation levels and was therefore regarded as reasonable to evaluate the response of the MPs, while minimizing stress on the animals.

All mice grew and behaved normally after implantation of the MPs. A subsequent swelling, which sometimes occurred at the subcutaneous injection sites, regressed within one or two weeks. Both subcutaneous and intramuscular pO$_2$ values increased under hyperoxic conditions, which was statistically significant (figure 3.35). For instance, six months after implantation, the subcutaneous pO$_2$ was (31 ± 9) mmHg under normoxia and (55 ± 18) mmHg under hyperoxia. In the muscle, the normoxic pO$_2$ of (50 ± 14) mmHg was raised to (62 ± 13) mmHg after hyperoxic challenge. These results proved that the MPs retained their oxygen sensitive behavior in prolonged *in vivo* experiments.

The pO$_2$ values determined by EPR were plausible and comparable to literature data. For instance, for murine subcutaneous tissue, pO$_2$ values of 38 mmHg [16] had been reported, whereas pO$_2$ values of 42 mmHg [16] and approximately 30 mmHg [200, 201] had been measured in muscle tissue under normoxia, which could be raised to approximately 50 mmHg [200] after 10 min of inspiratory hyperoxia. Smaller deviations might be attributed to the fact that the body temperature of the animals might have fallen slightly [200]. Animals were placed on heating pads, however, the temperature had not been controlled.

It must be noted, though, that the absolute pO$_2$ values in the subcutis under normoxic

(a) Subcutaneous pO$_2$ in the flank.

(b) Intramuscular pO$_2$ in the thigh.
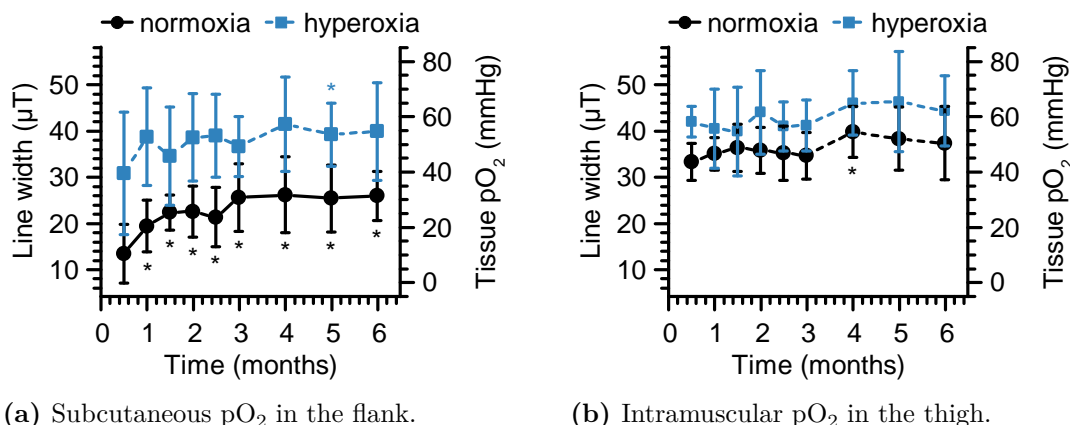
Figure 3.35: *In vivo* stability of the oxygen response of MPs: Tissue pO$_2$ assessed by EPR spectroscopy under normoxic conditions as well as after 10 min of inspiratory hyperoxia ($n = 8$). The differences in the pO$_2$ between inspiratory normoxia and hyperoxia were statistically significant two weeks as well as up to six months after injection of the MPs (not depicted in the graph). Additionally, all subsequent pO$_2$ values were compared to the first values obtained at the same injection site two weeks after injection. In general, there were no significant differences, except for the subcutaneous measurements under normoxia, as indicated by the asterisks. Only after 1.5 months, the values stabilized. Here, a paired Student's t test was used to evaluate the data ($\alpha = 0.05$).

conditions stabilized only after 1.5 months. The oxygen calibration curve was unchanged after recovery from the tissues *ex vivo* (data not shown here; it is referred to section 3.7.7). Thus, it is unlikely that the spin probe crystals had been altered chemically or physicochemically. However, an affection of the tissue cannot be excluded. It is inevitable that whenever biomedical devices are implanted into immunocompetent mammals and, hence, vascularized tissue is injured, a characteristic wound healing process is initiated [202, 203]. Swelling at the injection site indicated a starting immune response with the exudation of fluid, plasma proteins, and blood cells [203]. Inflamed lesions often become hypoxic as inflammation and hypoxia are known to be intimately linked, inducing and promoting one another [204, 205]. The most important transcription factors which are activated in response to hypoxic stimuli (HIF) and inflammation (κ-light-chain-enhancer of activated B cells, NF-κB) do not only have several common target genes, but also common regulators and stimuli [205]. Thus, the very low pO$_2$ determined by EPR in the first weeks after implantation suggests a development of hypoxia most probably following inflammation. After decay of the immune response, the pO$_2$ rose to normal and stabilized at the levels given above. Similar trends have been observed for LiPc/PTFE micro-inserts [113] and LiNc-BuO/PDMS chips [139].

Infiltration of inflammatory cells results in an inflammatory reaction with diverse cell signaling and is followed by migration of fibroblasts, which subsequently deposit a collagen capsule surrounding the device [203]. This capsule could act as a diffusion barrier for oxygen and, hence, disturb the measurements. DiEgidio *et al.* reviewed various attempts to eliminate fibrous capsule formation [202]. Neither surface modification or coating of the devices nor the administration of drugs inhibiting immune response reactions limited capsule formation satisfactorily. At best, the capsule thickness could be reduced.

After all, inhibiting inflammation after implantation of the MPs is a challenge, which goes beyond the scope of this work. Anderson defined biocompatibility practically as the ability of a medical device to perform as intended without significant harm to the host [203]. As long as there was no specific harm to the animals and the oxygen responsive behavior was retained, *i.e.*, oxygen was neither repelled nor accumulated by the capsule, any application of the MPs seemed possible. From these considerations, however, the following consequences resulted for subsequent *in vivo* experiments. To ensure the accuracy of the measurements, the absolute pO_2 values were either compared to literature values or verified by techniques based on different measurement principles. Moreover, the oxygen calibration curve was verified *ex vivo* after recovery from the tissue.

3.7.7 Biocompatibility

Immune response reactions are complex and depend on the tissue and the host [203]. Therefore, biocompatibility investigations in this work focus on selected tests, which only allow an evaluation of the applicability in the specific experiments at hand. The capability of the MPs as *in vivo* oxygen sensors was tested in two different syngeneic tumor models: The mammary carcinoma W256 in Wistar rats and the prostate carcinoma AT1 in Copenhagen rats. MPs were co-implanted with the tumor cells. So, it had to be ensured that this procedure did not affect the tumor proliferation or physiology. It has to be emphasized that in contrast to pure LiNc-BuO crystals, MPs could be redispersed in aqueous media effortlessly. This fact was advantageous with respect to their application. MPs allowed fast and easy mixing with tumor cells. The risk of damage to the tumor cells could be minimized and the MPs were homogeneously distributed in the cell suspension. The absence of agglomerates made MPs injectable even through very thin 30 G needles.

The cytotoxicity of the MPs was evaluated by incubating W256 and AT1 cells either with MPs or an equivalent amount of non-encapsulated LiNc-BuO crystals in comparison to untreated cells. Neither the lactate dehydrogenase (LDH, necrosis marker) nor the caspase 3 (apoptosis marker) activity was significantly altered compared to controls 8 h after exposition to MPs (figure 3.36). However, after 8 h of incubation with uncoated LiNc-

(a) Relative LDH activity.

(b) Relative caspase 3 induction.
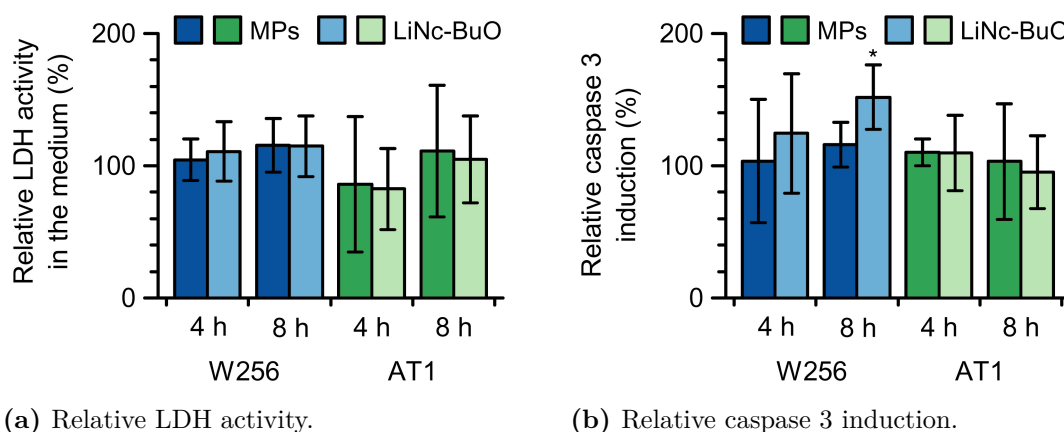
Figure 3.36: Cytotoxic effect of the MPs (1 mg/ml) in comparison to non-encapsulated LiNc-BuO (0.05 mg/ml) as determined *in vitro* ($n = 6$; all values were normalized to untreated control cells).

(a) W256 tumors.

(b) AT1 tumors.
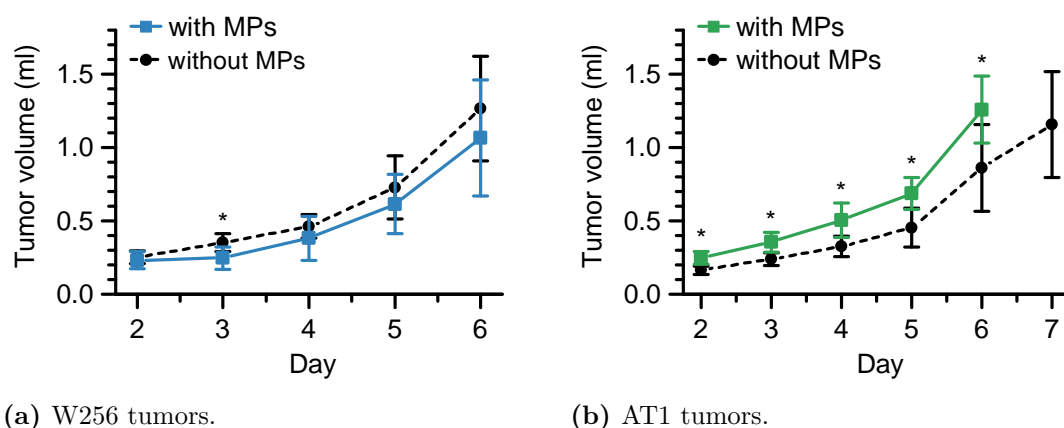
Figure 3.37: Growth curves of solid tumors *in vivo* after subcutaneous injection of cells ($4 \times 10^7/0.4$ ml) with approximately 10 mg or without MPs ($n = 10$ to 17).

BuO crystals, the caspase 3 activity in W256 cells was induced considerably, while the LDH release was not increased. These data indicate that LiNc-BuO crystals induced apoptotic cell death during which the cell membrane stayed intact (no LDH release). However, when using MPs, no evidence for cytotoxic activity was found. Hence, the encapsulation improved the biocompatibility of the LiNc-BuO crystals. After implantation of tumor cells with and without MPs, the tumor growth was monitored *in vivo*. Interestingly, while the growth of W256 tumors was independent from the presence of MPs, the growth rate of AT1 tumors accelerated significantly by co-implantation of MPs (figure 3.37).

(a) Density of CD163 positive cells.

(b) Vascular density.
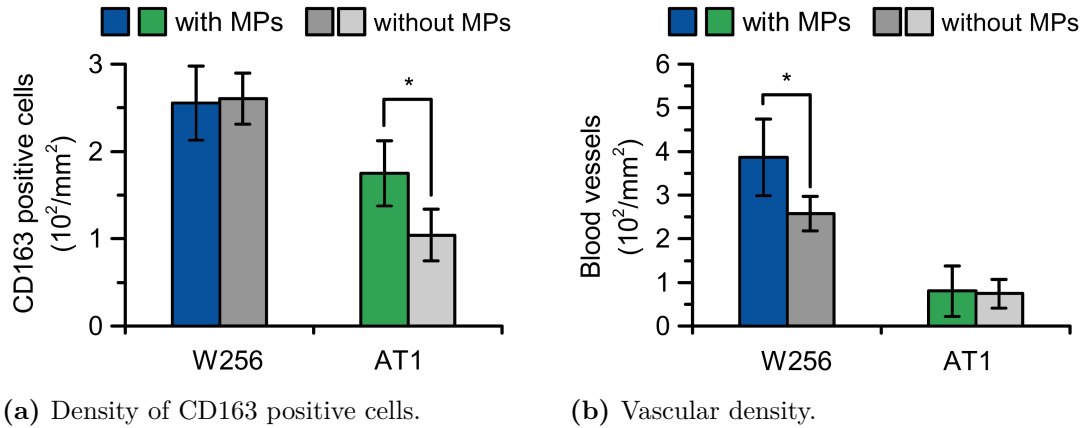
Figure 3.38: Results of immunohistochemical analysis *ex vivo* ($n = 4$ to 6).

(a) W256 tumors.

(b) AT1 tumors.
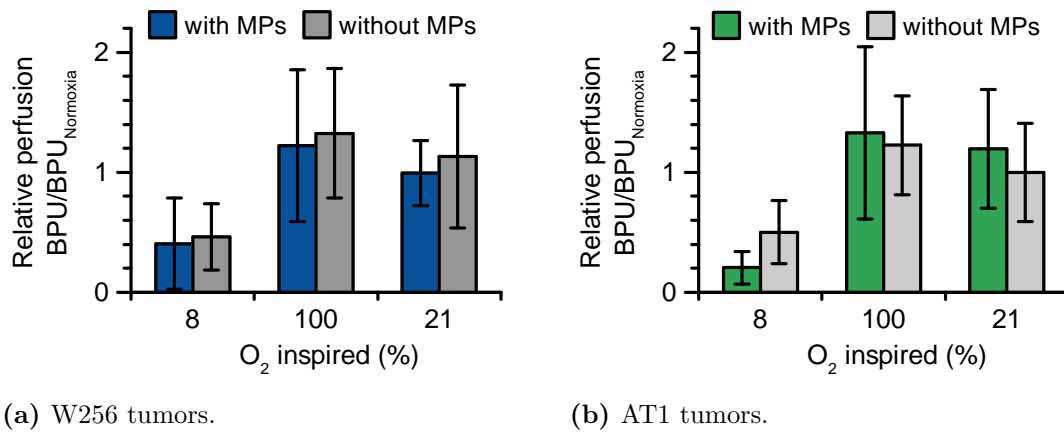
Figure 3.39: Relative tumor perfusion with or without MPs in the last two minutes of each treatment during fluorometric *in vivo* pO_2 measurements (section 3.7.9.1) ($n = 10$; values were normalized to perfusion measurements under initial normoxic conditions).

AT1 tumors with MPs showed an increased number of CD163 positive cells, a marker of monocytes and macrophages responsible for immune response, while in W256 tumors, no difference could be observed (figure 3.38a). This might explain the accelerated growth of AT1 tumors by the MPs (figure 3.37b). The greater infiltration and activation of macrophages in the tissue of AT1 tumors possibly led to a promoted angiogenesis and tumor growth [206]. The blood vessel density in AT1 tumors was unaffected by incorporation of MPs. On the contrary, it was significantly increased in W256 tumors when MPs were co-implanted (figure 3.38b). However, the relative blood perfusion was not significantly changed by the presence of MPs in both tumor models (figure 3.39). The perfusion was
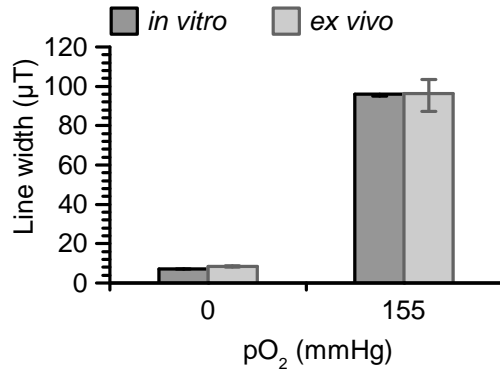
Figure 3.40: Comparison of EPR line widths of *in vitro* and *ex vivo* calibrations in nitrogen as well as in air ($n = 3$).

monitored during the fluoro-optical measurements described in section 3.7.9.1. Hence, neither the increased vascular density in W256 tumors nor the increased density of CD163 positive cells in AT1 tumors seemed to affect the tumor perfusion.

It was further assured that the oxygen sensitivity remained unchanged during the *in vivo* experiments. Therefore, the MPs were recalibrated *ex vivo* after resection and homogenization of MP containing tumors. The EPR line widths under anoxic and normoxic conditions were comparable to the values obtained before implantation (figure 3.40).

Taking all these aspects into consideration, there was no evidence for cytotoxic effects of the MPs. Neither the tumor physiology nor the oxygen sensitivity of the MPs were affected appreciably. Hence, the MPs can be used for *in vivo* measurements of extracellular tumor pO_2 in both tumor models by EPR oximetry.

3.7.8 Distribution of MPs in the tumor tissue

In previous pilot studies, it was found that an injection of the MPs into an already existing tumor resulted in a rather local and non-homogeneous distribution of the MPs in the tumor tissue. It has to be considered that hypoxic areas are often heterogeneously dispersed within the tumor tissue on a millimeter scale [207], and particulate probes are known to report pO_2 levels only from a limited volume around their surface [20]. Consequently, when EPR probes are injected intratumorally and stay at the injection site, the resulting measurement volume is small. Hence, the pO_2 values measured might not be characteristic for the mean overall tumor oxygenation.

One approach to overcome these problems is the pre-internalization of spin probe crystals into tumor cells prior to inoculation, but this method is rather complex [100, 103, 108]. Another option is to inject the MPs simultaneously with the tumor cells. Ilangovan *et al.* co-embedded uncoated LiPc crystals with tumor cells [28]. However, the particulates were found to be aggregated mainly in the middle of the tumor, probably due to the low
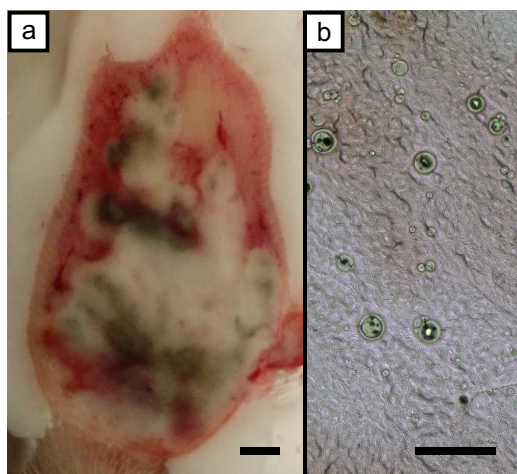
Figure 3.41: Distribution of the MPs inside the tumor tissue. (a) Photograph of a typical cryosection of an AT1 tumor (bar size: 2 mm). Note that the MPs appear as dark green-grey colored areas all over the tissue. (b) Microscopic image of a typical AT1 tumor slice (thickness 20 μm) after cryosection showing that the MPs were not aggregated in the tissue (bar size: 100 μm).

wettability of the hydrophobic spin probe crystals. As mentioned above, by incorporation into MPs, the dispersibility could be improved considerably. The MPs showed no tendency to aggregate. Hence, it was assumed that by co-embedding MPs with tumor cells a more homogeneous distribution could be achieved, such that the pO_2 could be assessed in multiple sites of the tumor tissue.

After a horizontal cryosection through an AT1 tumor it could be observed that the dark colored spots of MPs were distributed all over the entire tumor volume (figure 3.41a). The distribution was not completely homogeneous which might have been a result of variations of the proliferation rates of cells in different tumor regions. However, microscopy revealed that even in areas, which macroscopically did not appear colored, MPs were incorporated. Microscopic images showed that MPs were embedded as separate particles, which were not aggregated (figure 3.41b).

Additionally, MPs were counted in $1\,mm^2$ areas of 20 μm cryosections (figure 3.42). Since the distribution was approximately lognormal, there were only a few areas with several hundred MPs or without any MPs. Hence, some MPs were certainly clustered, but in general, they were more or less evenly distributed as separate particles in all dimensions of the tumor tissue.

These results suggest that the co-implantation of MPs would also be a particularly promising approach for *in vivo* EPR imaging experiments, which generally have a spatial resolution of 1 mm [208]. Hence, the MPs might have the potential to combine advantages of both soluble and particulate EPR probes. The MPs were more or less evenly distributed within the tissue allowing for multiple site measurements, which is generally only achieved by soluble probes. On the other hand, they provide a high oxygen sensitivity and long-term stability which is typical for particulate probes and offers the possibility of repeated oximetry (imaging) measurements *in vivo*.

(a) W256 tumors.

(b) AT1 tumors.
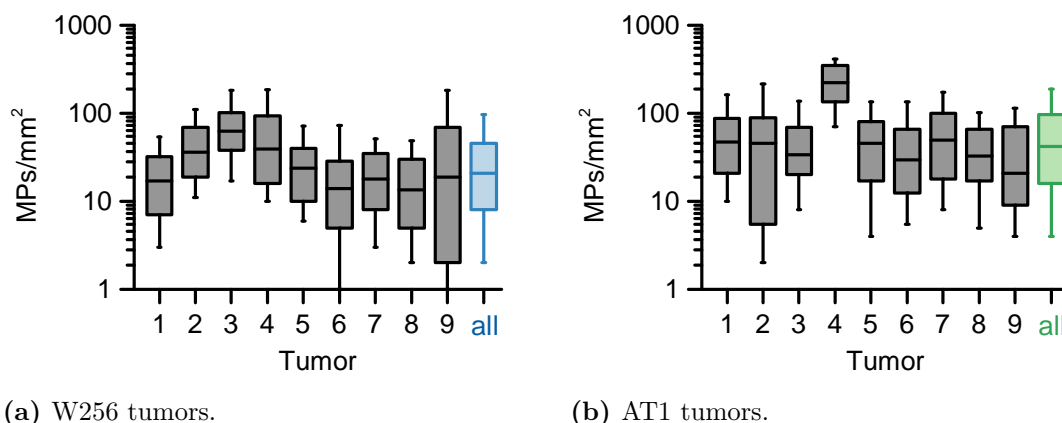
Figure 3.42: Density of MPs counted in 20 µm thick slices. Whiskers are determined by the 10th and 90th percentiles, boxes by the 25th, 50th, and 75th percentiles. MPs, which were much larger than the thickness of the slice (>20 µm), might have been excluded from the counting.

3.7.9 *In vivo* experiments

3.7.9.1 Time course measurements of tumor pO_2 by EPR spectroscopy in comparison to fluorometric measurements

The MPs were applied *in vivo* to determine the intratumoral pO_2 in two tumor models, namely W256 and AT1 tumors. When the tumors reached the targeted volume, the oxygenation was measured by EPR spectroscopy in anesthetized animals. Over a total of 60 min, the inspiratory gas mixture was changed in four periods from room air ($\approx 21\,\%$ O_2) to inspiratory hypoxia ($\approx 8\,\%$ O_2), to inspiratory hyperoxia ($100\,\%$ O_2), and finally back to room air (see scheme in figure 3.43) to investigate the accuracy and the dynamic behavior of the EPR oximetric measurements.

For comparison, the pO_2 in the tumor tissue was also determined invasively by optical fluorescence oxygen sensors (Oxylite) following the same procedure. During each treatment period, arterial blood gases were analyzed. However, taking blood samples meant additional stress to the animals, particularly under hypoxia, where circulatory disorders were already provoked. Thus, it was only performed if the respective situation allowed it.

Blood gas analysis

The animals were anesthetized with pentobarbital. As typical for all barbiturates it causes a depression of the central nervous system resulting in decreased heart and respiratory rates. When the breathing is rather slow and shallow, more CO_2 is retained. Failure to

Table 3.5: Results of arterial blood gas analysis in Wistar rats during treatment with various inspiratory gases, where pCO_2 is the partial pressure of CO_2, sO_2 is the oxygen saturation, $c(HCO_3^-)$ is the calculated concentration of bicarbonate in the blood, reported as mean (range) [$n = 8$ (1st normoxia), $n = 1$ (hypoxia), $n = 3$ (hyperoxia), $n = 4$ (2nd normoxia)].

Analyte	1st Normoxia	Hypoxia	Hyperoxia	2nd Normoxia
pH value	7.4 (7.35 - 7.44)	7.48	7.36 (7.26 - 7.46)	7.43 (7.4 - 7.44)
pCO_2 (mmHg)	51 (37 - 62)	33	56 (43 - 79)	47 (45 - 50)
pO_2 (mmHg)	87 (67 - 112)	34	413 (371 - 473)	89 (70 - 114)
sO_2 (%)	96 (92 - 98)	70	100 (100 - 100)	96 (94 - 98)
$c_{HCO_3^-}$ (mM)	31 (24 - 34)	24	30 (26 - 34)	30 (30 - 30)

breathe off CO_2 can lead to respiratory acidosis if it is not compensated by the renal system, which modulates the HCO_3^- concentration. Mean reference values obtained from awake rats in different studies were 7.43 to 7.47 for arterial pH value, 34.5 mmHg to 41.2 mmHg for pCO_2, 90.0 mmHg to 94.1 mmHg for pO_2, and the calculated HCO_3^- concentration was 25.5 mM, respectively [209, 210]. Under anesthesia with pentobarbital, the pH value was found to be lower, but slightly increasing with time, whereas the pCO_2 was higher, but slightly decreasing. The HCO_3^- concentration was slightly increased.

Also in this study, under normoxia, the pCO_2 was relatively high indicating a beginning respiratory acidosis. It is compensated by HCO_3^- as can be seen from the pH value, which is low but still in the normal range, and the increased concentration of HCO_3^-. Compared to normoxia, where the respiratory rate usually was 60 breaths/min to 90 breaths/min, the breathing was very fast under hypoxia and oxygen insufficiency (120 breaths/min to 160 breaths/min). Apparently, thereby, more CO_2 was breathed off and the pCO_2 was decreased as well as the pH value, which indicates an uncompensated respiratory alkalosis. Under hyperoxic conditions, the breathing was very slow (20 breaths/min to 70 breaths/min), whereby pCO_2 was retained again and the pH value was rather low. Here, the respiratory acidosis was compensated by HCO_3^- as well.

The data also revealed that not only the arterial sO_2, which represents the portion of oxygen-saturated hemoglobin in relation to total hemoglobin in the blood, is changing with inspiratory oxygen content but also the pO_2. Under normoxia, hemoglobin already

is almost saturated with oxygen (here: 96%, the mean pO_2 was $87\,\text{mmHg}$ to $89\,\text{mmHg}$). Under hypoxia, not only the sO_2 was decreased severely to 70%, also the pO_2 was very low ($34\,\text{mmHg}$). Under hyperoxia, the sO_2 reached 100%, which means that all hemoglobin was saturated by oxygen. Excess oxygen remained physically dissolved in the blood resulting in a very high pO_2 of $413\,\text{mmHg}$.

This correlation is important when the oxygen status of the blood is sought. By EPR spectroscopy, only the physically dissolved amount of oxygen and the pO_2 in the blood could be measured, respectively. These values are not equal to the total oxygen content in the blood as the hemoglobin-bound portion cannot be gathered EPR spectroscopically. However, in this work, the tissue pO_2 is of interest, which is expected to change with the content of oxygen in the arterial blood.

Oximetry measurements

To compare the dynamics of both oximetry methods, the time courses of oxygenation during the change of the inspiratory gas mixture are shown in figure 3.43. The data revealed that W256 tumors were well oxygenated. After switching the inspiratory gas, the pO_2 in W256 tumors followed rapidly within $5\,\text{min}$. Comparable results were obtained by invasive fluoro-optical measurements. Actually, the dynamics of EPR oximetry measurements were slightly faster than those of the Oxylite system.

Note that pO_2 values above $100\,\text{mmHg}$ were out of range for Oxylite but not for EPR measurements. This limitation might explain the slightly different time course of the tumor pO_2 during inspiratory hyperoxia. The Oxylite measurements reached an almost constant value of approximately $90\,\text{mmHg}$ within the hyperoxic period. The averaged absolute tissue pO_2 measured by EPR was comparable. However, the pO_2 was slightly but constantly increasing during the hyperoxic phase.

In contrast, the oxygenation level of AT1 tumors of comparable size was much lower and the relative variability of the measurements higher than in W256 tumors. It should be noted that the deviations of the pO_2 values under normoxia measured by the Oxylite system showed a drift, which probably indicates that in a few individuals, the equilibrium had not been reached before the pO_2 measurement was started. Here, the EPR results seemed to reflect more realistic values.

To further evaluate the accuracy of the EPR oximetry measurements, the pO_2 values of both methods, which were obtained from the last interval of treatment with the respective gas mixture, were compared in figure 3.44. In the tumor models investigated, the results of both oximetry techniques were comparable indicating that the accuracy of the EPR measurements using MPs as oxygen sensors was sufficient. Moreover, the pO_2 values measured with the Oxylite system were independent from the presence or absence of MPs
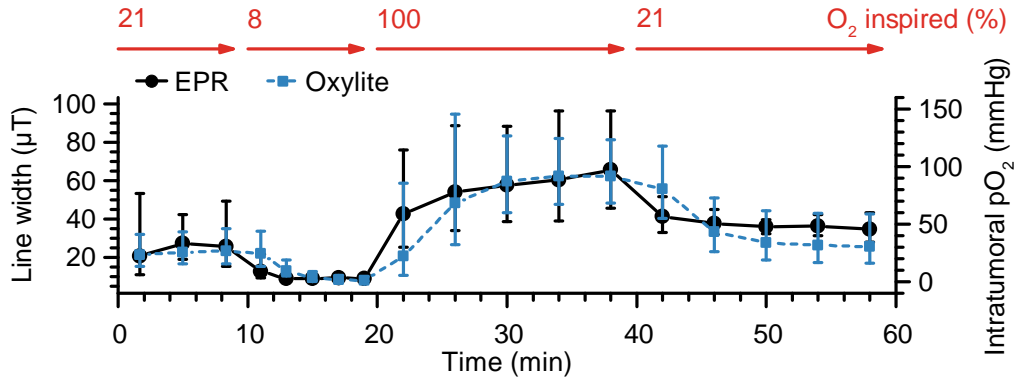
(a) W256 tumors.
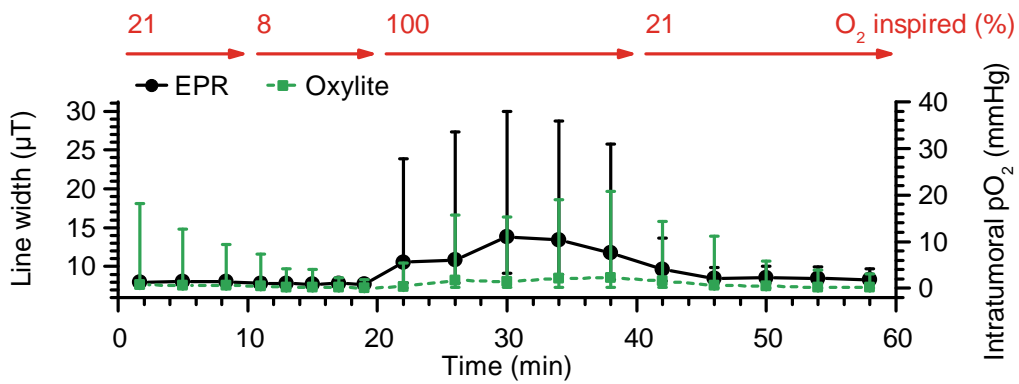
(b) AT1 tumors.

Figure 3.43: Time course of *in vivo* pO_2 measurements measured by EPR spectroscopy and a fluoro-optical method (Oxylite) during modulation of the inspiratory gas. Note that most of the Oxylite measurements in W256 tumors under hyperoxia (9 of 10 with MPs, 7 of 8 without MPs) were out of range (above 100 mmHg), and therefore assumed to be 100 mmHg. Data reported as geometrical mean (GM) and standard deviation (GSD), in particular, GM $\div$ GSD as lower and GM $\cdot$ GSD as upper limit ($n = 8$ to 10).

in the tumor tissue. Apparently, the tumor oxygenation was not altered significantly due to the MPs, even though the vascular density was markedly increased in W256 tumors when MPs were co-implanted (figure 3.38b).

Admittedly, in AT1 tumors under hyperoxic conditions, both measurement techniques showed deviations, which was most likely caused by a high interindividual variance as well as intraindividual heterogeneity of the tumor oxygenation. Earlier studies, which compared EPR and Oxylite oximetry, already stated that the measurement volume of the fluoro-optical sensors was relatively small [211, 212]. Obviously, the Oxylite system is less suitable to describe the averaged pO_2 of the entire tumor tissue. However, the pO_2 values

(a) W256 tumors.

(b) AT1 tumors.
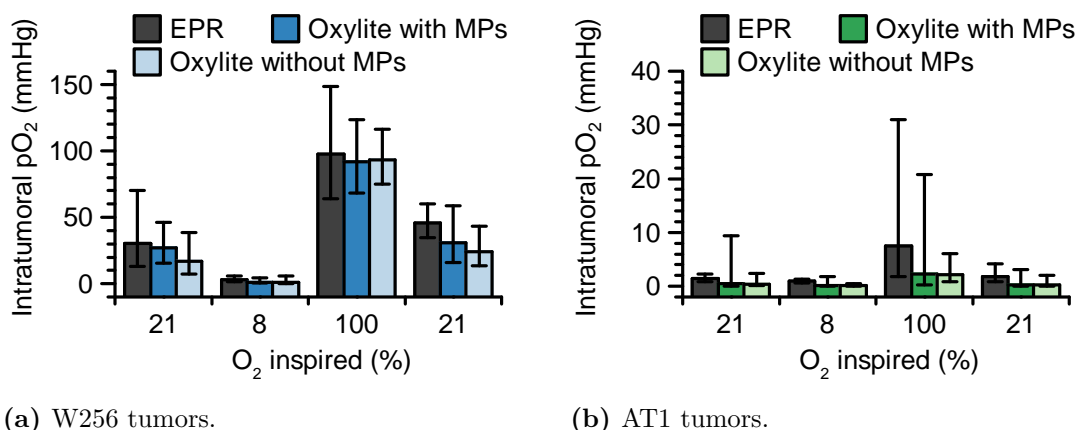
Figure 3.44: Comparison of pO_2 values obtained from the last interval of treatment with the respective gas mixture. Note that most of the Oxylite measurements in W256 tumors under hyperoxia (9 of 10 with MPs, 7 of 8 without MPs) were out of range (above $100\,\text{mmHg}$),and therefore assumed to be $100\,\text{mmHg}$. Data reported as GM and GSD, in particular, GM $\div$ GSD as lower and GM $\cdot$ GSD as upper limit ($n = 8$ to 10). Neither the differences between pO_2 values obtained by EPR and Oxylite measurements nor between Oxylite measurements with and without MPs were statistically significant (Mann-Whitney-U test, $\alpha = 0.05$).

measured by EPR were comparable to what had been gathered polarographically in $1.5\,\text{ml}$ to $2\,\text{ml}$ large AT1 tumors, namely approximately $3\,\text{mmHg}$, $1\,\text{mmHg}$, and $12\,\text{mmHg}$ under inspiratory normoxia, hypoxia, and hyperoxia, respectively [213]. The pO_2 determined in W256 tumors under normoxia was in agreement with the literature, too, where an averaged oxygen tension of $(32.9 \pm 6.7)\,\text{mmHg}$ had been calculated from dynamic contrast enhanced MRI measurements [214].

3.7.9.2 Correlation of pO_2 measured by EPR spectroscopy with presence of hypoxic regions detected by pimonidazole

Since the fluoro-optical oximetry technique is not suitable to measure the heterogeneity of the entire tumor oxygenation, EPR measurements were compared to the binding of a hypoxia marker on a microscopic scale. Therefore, the irreversible adducts of pimonidazole were determined immunohistochemically and compared to pO_2 values acquired by EPR spectroscopy. Pimonidazole binds to peptide thiols specifically in hypoxic cells [215]. In particular, areas with pO_2 values below $10\,\text{mmHg}$ are detected [216], where hypoxia becomes clinically relevant [15].
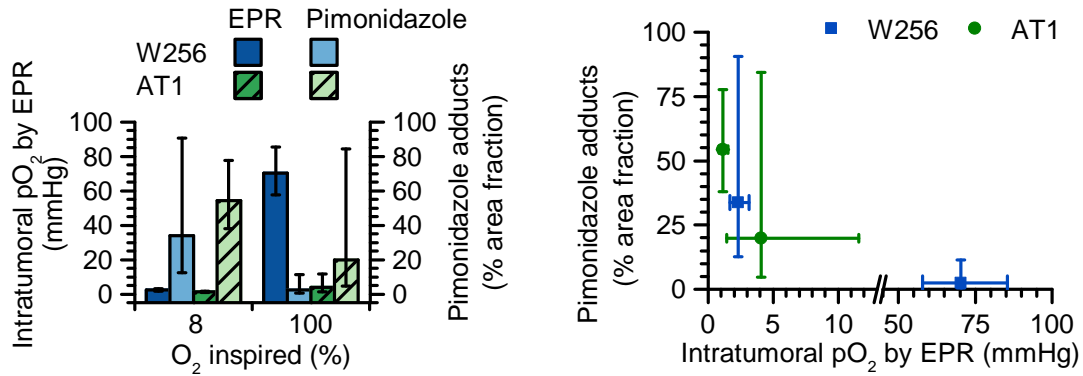
(a) Intratumoral pO_2 values measured *in vivo* by EPR spectroscopy as well as fraction of hypoxic regions as determined *ex vivo* by immunofluorescence using pimonidazole.

(b) Correlation between both methods.

Figure 3.45: Effect of 90 min exposure to either hypoxia or hyperoxia. Data reported as GM and GSD, in particular, GM $\div$ GSD as lower and GM $\cdot$ GSD as upper limit ($n = 5$).

Under inspiratory hypoxia, the pO_2 values measured by EPR were markedly below 10 mmHg in both tumor models (figure 3.45a). After treatment with pure oxygen, the pO_2 in W256 tumors increased dramatically (≈ 71 mmHg), whereas AT1 tumors remained hypoxic (≈ 4 mmHg). Accordingly, the highest accumulation of pimonidazole was observed in AT1 tumors under hypoxia ($\approx 54\%$ area fraction), and the lowest in W256 tumors under hyperoxic conditions ($\approx 3\%$ area fraction).

In figure 3.45b, the correlation between the pO_2 obtained by EPR oximetry and the pimonidazole binding is shown. The relationship is comparable to the correlation which had been found between the mean pO_2 measured by EPR oximetry and the binding of another nitroimidazole-based hypoxia marker (EF5) in NFSA tumors [217].

The pO_2 values of AT1 tumors measured by EPR, which are shown in figure 3.45a, (≈ 4 mmHg) were somewhat lower than those of the experiments presented in figure 3.44b (≈ 8 mmHg). This difference, however, reflects the large intertumoral variability of AT1 tumors during inspiratory hyperoxia.

Typical fluorescence microscopic images affirmed that the pimonidazole binding and, thus, hypoxic areas were heterogeneously dispersed all over the tumor area rather than located at specific sites (figure 3.46). These results underline that an even distribution of the spin probes is necessary to obtain representative overall oxygenation values, which are less affected by intraindividual heterogeneities.
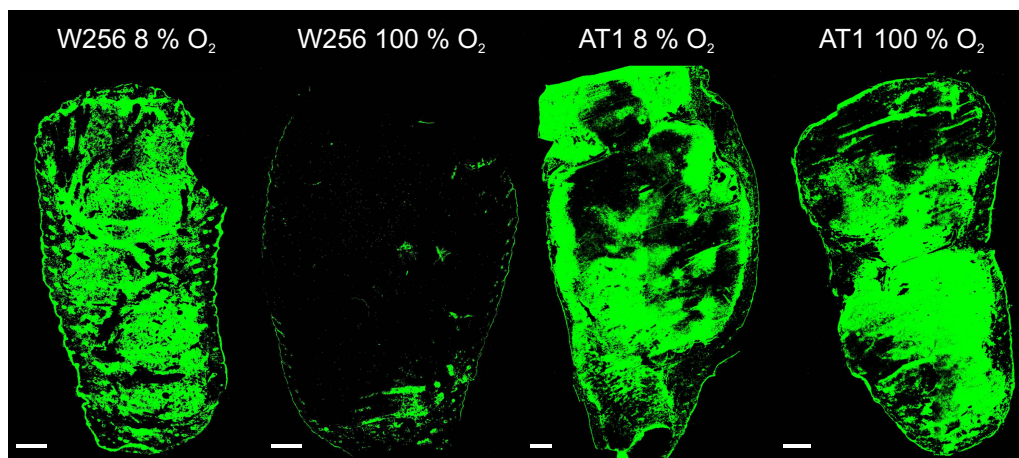
Figure 3.46: Fluorescence microscopic images of typical W256 and AT1 tumors under hypoxia and hyperoxia showing hypoxic regions as determined *ex vivo* by immunofluorescence using pimonidazole (bar size: 1 mm).

3.8 Conclusion and outlook

EPR oximetry with particulate materials like LiNc-BuO promised several advantages over soluble probes such as trityl radicals. Most of them could be confirmed.

First of all, LiNc-BuO showed excellent oxygen sensitivity, which refers not only to the raw spin probe crystals, but also to the incorporated material, namely the MPs.

The specificity of particulates for oxygen should be very high. Since they respond to changes in the pO_2, rather than concentration of oxygen, their line width should not be influenced by microenvironmental parameters other than oxygen. Actually, it was shown that a raise from room temperature to body temperature did not have any effect on oxygen sensitivity. However, unfortunately, the line width was not completely independent of the surrounding milieu. Different line widths in various solvents were attributed to some kind of interactions with the same. Also in aqueous dispersion media, the line width was slightly changed, however, the oxygen response remained linear. By microencapsulation, these effects could be reduced.

Further, particulate materials exhibit a higher spin density without concentration broadening effect as well as more favorable microwave power saturation properties in comparison to soluble probes. In fact, pure LiNc-BuO as well as MPs showed excellent signal intensities. With the equipment used in this work, even *in vivo*, satisfactory SNRs were obtained in adequate time. Comparisons with fluorometric oximetry measurements as well as the binding of a hypoxia marker proved the reliability and accuracy of the EPR measurements.

Particulates are generally more resistant against redox reactions and, therefore, have longer *in vivo* half life times than soluble probes. However, their *in vivo* stability might be affected by alteration of their complex crystalline structure or fibrous capsule formation in the tissue. It was assumed that incorporation into oxygen-permeable biocompatible polymers might enhance the physical stability. The barrier provided by encapsulation further mitigates a potential toxicity of the radical. Nevertheless, implantation of the polymeric devices was expected to induce foreign body responses (inflammatory cell in-filtration, fibrous capsule formation) [123]. Although these reactions were unavoidable, it was shown that the oxygen responsive behavior of the MPs remained over six months without being altered due to implantation. After implantation, the MPs stayed at the injection site without migration. Thereby, measurements could be made localized wit-hout the radical partitioning out of the tissue of interest. All in all, the MPs allowed for repeated measurements at the same location in prolonged *in vivo* studies.

For various issues in preclinical research, not only the average oxygenation of tissues might be useful, but also its spatial distribution. LiNc-BuO loaded NPs would probably distribute homogeneously in tissues like soluble radicals. For several reasons, which are discussed above, better SNRs can be achieved with LiNc-BuO NPs in comparison to trityl loaded NCs. However, it is questionable if the signal intensity would be sufficient for *in vivo* experiments. NPs would be administered intravenously, where the applicable volume in small animals such as mice and rats is limited to 5 mL/kg body weight. More precisely, in mice only approximately 100 µL to 200 µL and in rats approximately 1 mL to 2 mL can be administered. By passive targeting, only part of the substance would be accumulated in the tumor. Since the distribution of NPs in the body depends on various factors and might be improved by active targeting, further experiments are needed to evaluate the *in vivo* applicability of the NPs. Unfortunately, all attempts to reproducibly nanoformulate LiNc-BuO failed. Apart from the apparent line width, which was varying drastically from batch to batch, two EPR species appeared in the spectrum. While the first problem could be handled if the oxygen sensitivity of every batch was calibrated prior to usage in an experiment, the second aspect would exacerbate oximetry experiments decisively.

However, *ex vivo* analysis revealed that by co-implantation with tumor cells, MPs were homogeneously dispersed within the tumor tissues as well. This could be achieved since LiNc-BuO loaded MPs were easily dispersable and injectable. Hence, LiNc-BuO loaded MPs might be an alternative for EPR imaging in tumor tissues. Since the proof of concept was successful, further formulations for LiNc-BuO are conceivable. For instance, the process parameters might be tuned such that very small MPs, *i.e.*, up to 2 nm to 3 nm, with narrow size distribution would form, which would allow to be administered intravascularly. Further, in respect of an eventual clinical use, the size of the oxygen sensor might also

be enlarged to enable retrieval from the tissue. Alternatively, MPs could be embedded in a polymer mesh pouch [218]. If desired, alternative polymers, such as PDMS [137], PTFE [136], cellulose acetate [123], ethyl cellulose, polyethylene, poly-ϵ-caprolactone, and poly(meth)acrylates can be deployed.

To conclude, it must be said that the particulate spin probe LiNc-BuO was superior to soluble trityl radicals in many aspects. Especially LiNc-BuO loaded MPs showed their suitability for EPR oximetry experiments, in particular *in vivo*.

4 Summary

Whenever oxygen is involved in physiological or pathological processes, a reliable quantification of tissue oxygenation is important to gain a deeper insight into underlying mechanisms. Despite extensive research efforts, the *in vivo* determination of tissue pO$_2$ is still a challenge and none of the techniques developed fully satisfies all requirements. However, EPR oximetry became an indispensable tool as it allows for noninvasive, absolute, and accurate oxygen measurements in real-time. Albeit being a diradical, oxygen cannot be detected directly, but solely upon interaction with oxygen sensitive spin probes. Thereby, the EPR lines of these radicals become broadened. The need for employment of these stable radicals is connected with concerns regarding their biocompatibility, and stability in tissues. Moreover, synthesis of these radicals is sophisticated, but high quality in terms of their physicochemical and oxygen sensing properties is crucial for reliable oximetric measurements. To address the main goal of this work, which was the noninvasive investigation of tissue oxygenation in two preclinical tumor models, two different types of radicals were comprehensively investigated to assess their *in vivo* applicability. For the most promising radicals, appropriate formulations were developed, which enhanced their biocompatibility, and preserved their oxygen responsive behavior.

The first part of this work deals with soluble trityl radicals, which had been synthesized and analytically characterized by cooperation partners. To evaluate their suitability as oxygen sensors, the sensitivity, linearity, and specificity of the oxygen response were investigated. The EPR properties of various hydrophilic trityl radicals were studied in aqueous media. These radicals were distinguished by their extremely narrow EPR line widths. As they can be administered directly in aqueous solution, the specificity of line width changes for oxygen was crucial. It was shown that within physiological limits of osmolarity, viscosity, and pH value, there was, for practical purposes, no impact on the EPR line widths. The EPR line width broadened linearly with increasing oxygen content. Thus, hydrophilic trityl radicals proved to be useful EPR oximetry probes. But since c$_{O_2}$ in water does not change much with pO$_2$, their oxygen sensitivity was rather low. Hence, the accuracy, and capability of detecting small changes in pO$_2$ were rather poor.

Furthermore, several lipophilic trityl triesters were studied in MCT and IPM as the solubility of oxygen in oils is significantly higher. The nondeuterated triethyl esters of TAM

and dTAM showed hfs in deoxygenated solutions. Other triesters exhibited single EPR lines with line widths directly proportional to the oxygen concentration, rendering them candidates for oxygen measurements rather than triesters showing hfs. The perdeuterated triethyl ester dTAM-dEE combined good synthetic accessibility and promising EPR properties. It showed a favorably narrow EPR line under anoxic conditions and a high oxygen sensitivity, especially when dissolved in IPM – higher than any water-soluble probe can provide. Therefore, encapsulation of dTAM-dEE into MCT/IPM-core/PVAc-shell NCs was a promising approach. The NC preparation method developed in this work allowed reproducible preparation of NCs with appropriate particle characteristics and EPR properties. It was shown that the oxygen responsiveness of the incorporated radical was retained. Using IPM for encapsulation, a very high oxygen sensitivity of the NCs could be ensured, especially suitable for measuring low oxygen contents. MCT provided stable NCs for long term measurements. Major concerns such as the toxicity of trityl radicals and their sensitivity to biological oxidoreductants could be overcome. An ascorbic acid reduction assay suggested that dTAM-dEE was lipophilic enough to stay inside the NCs and revealed that encapsulated radicals were shielded against reduction. Hence, encapsulation of lipophilic trityl radicals offers potential for nanosensors with high oxygen sensitivity, specificity, and stability, particularly suitable for EPR oximetry in complex biological systems. However, the major limitation of these NCs, exacerbating *in vivo* applications, was their poor EPR signal intensity due to the intrinsic low amount of encapsulated radical.

As an alternative, in the second part of this work, the particulate radical LiNc-BuO was tested, which is employed as a solid. Synthesis of LiNc-BuO is sophisticated, hardly yielding reproducible particle and crystal properties. Therefore, thorough physicochemical analysis was sought in order to affirm the identity and purity. Several analytical techniques revealed that the material, obtained by a commercial supplier, was well usable for oximetric experiments, although it did not fully comply in terms of its purity. Abundance of impurities was very low and their appearance did not have any negative impact on the EPR spectrum or the oxygen sensitivity. LiNc-BuO was nanoprecipitated as polydisperse nanocrystals. By coating with PVAc, the properties of the NPs could be significantly improved: The preparation method yielded monodisperse NPs with reproducible particle size characteristics. The SNR was higher in comparison to trityl loaded NCs. Nevertheless, it was still questionable if the signal intensity would be sufficient for *in vivo* experiments. Morover, the EPR spectrum often showed a superposition of at least two species, aggravating spectra analysis. This was probably caused by the instability of LiNc-BuO in water or by impurities mentioned before, which may have affected the (re-) crystallization process as well as the accessibility of the surface areas or the inner microchannels for oxygen and other gases.

To circumvent the complex crystallization process and avoid aqueous media, a non-aqueous method for preparation of PVAc coated LiNc-BuO loaded MPs was developed. Nonbiodegradability and the preparation method, which ensured that no non-encapsulated spin probe was left, reliably prevents spin probe-tissue contact. Encapsulation improved the stability of LiNc-BuO in dispersion. These microparticulate sensors showed excellent oxygen sensitivity, which was slightly reduced in comparison to the raw material, but still favorably high, perfectly linear, and reproducible. The oxygen response was sufficiently fast and reversible, demonstrating that the polymer matrix did not impact the oxygen sensing properties by, *e.g.*, accumulation of oxygen. Due to the high spin density of LiNc-BuO without any concentration broadening effect, even *in vivo*, satisfactory SNRs were obtained with MPs in adequate time. The oxygen responsive behavior of the MPs remained over six months *in vivo* without being altered due to implantation, which was proven by *ex vivo* calibration. After implantation, the MPs stayed at the injection site without considerable migration. Thereby, measurements could be made localized without the radical diffusing out of the tissue of interest, allowing for repeated measurements at the same location in long term *in vivo* studies. By co-implantation with tumor cells, MPs were administered minimally invasive, tissue injury and trauma were avoided. Different oxygenation levels of two tumor models (W256 and AT1 tumors) under normoxia, hypoxia, and hyperoxia were assessed reproducibly. Comparison with fluorometric oximetry measurements as well as with the accumulation of a hypoxia marker (pimonidazole) confirmed that the MPs allowed reliable and accurate oxygen measurements in tumor tissues. In contrast to the raw material, LiNc-BuO loaded MPs were easily dispersable and injectable. Hence, MPs were distributed as individual particles all over the tumor tissue reporting pO_2 values from various regions of the tumor, which was crucial since the oxygenation is heterogeneously distributed. There was no evidence that the MPs were toxic, in another way not biocompatible, or altered the tumor physiology. MPs can be sterilized by β^- irradiation, which did not affect the particle or oxygen sensing properties of the MPs adversely.

Three formulations approached in this work (hydrophilic trityl radicals in aqueous solution, oily core NCs with incorporated lipophilic trityl triesters, and LiNc-BuO loaded MPs) are useful as *in vitro* oximetry sensors, which are interchangeable depending on the research issue. Especially the easily injectable MPs developed in this work are well suitable EPR oxygen sensors for preclinical research *in vivo*, which may be particularly useful for real-time measurements, long term studies, as well as EPR imaging in tissues. MPs have the potential to promote not only the noninvasive assessment of tissue oxygenation *in vivo* but also the therapy improvement of numerous pathological conditions, paving the way toward individualized therapy strategies.

References

[1] R. Cowen, "Chapter 1: The origin of life on earth", in *Hist. life, 4th ed.* Blackwell Publishing, 2005, pp. 1–15.

[2] M. Rizotti, "History of life", in *Biol. Sci. Fundam. Syst.* EOLSS Publications, 2009, pp. 212–230.

[3] E. Rabinowitch and Govindjee, *Photosynthesis.* John Wiley & Sons, Inc., 1969.

[4] J. Whitmarsh and Govindjee, "Section I.2. The photosynthetic process", in *Concepts Photobiol. Photosynth. Photomorphogenes.* Springer Science & Business Media, 2012.

[5] N. N. Greenwood and A. Earnshaw, "Chapter 14: Oxygen", in *Chem. Elem. 2nd ed.* Elsevier, 2012.

[6] C. Starr, C. Evers, and L. Starr, "How cells release chemical energy", in *Biol. A Hum. Emphasis, 8th ed.* Cengage Learning, 2010.

[7] F. Sizer and E. Whitney, "Food choices and human health", in *Nutr. Concepts Controv. Band 10*, Cengage Learning, 2007.

[8] V. J. Thannickal, "Oxygen in the evolution of complex life and the price we pay", *Am. J. Respir. Cell Mol. Biol.*, vol. 40, no. 5, pp. 507–510, 2009. DOI: `10.1165/rcmb.2008-0360PS`.

[9] J. C. Walsh, A. Lebedev, E. Aten, K. Madsen, L. Marciano, and H. C. Kolb, "The clinical importance of assessing tumor hypoxia: Relationship of tumor hypoxia to prognosis and therapeutic opportunities", *Antioxid. Redox Signal.*, vol. 21, no. 10, pp. 1516–54, 2014. DOI: `10.1089/ars.2013.5378`.

[10] C. Michiels, "Physiological and pathological responses to hypoxia", *Am. J. Pathol.*, vol. 164, no. 6, pp. 1875–1882, 2004. DOI: `10.1016/S0002-9440(10)63747-9`.

[11] G. L. Semenza, "Hypoxia-inducible factor 1 and cardiovascular disease", *Annu. Rev. Physiol.*, vol. 76, pp. 39–56, 2014. DOI: `10.1146/annurev-physiol-021113-170322`.

[12] Destatis, *Todesursachenstatistik*, 2015.

[13] P. Vaupel, O. Thews, and M. Hoeckel, "Treatment resistance of solid tumors: Role of hypoxia and anemia", *Med. Oncol.*, vol. 18, no. 4, pp. 243–259, 2001. DOI: `10.1385/MO:18:4:243`.

[14] J. Pacheco-Torres, P. Lopez-Larrubia, P. Ballesteros, and S. Cerdan, "Imaging tumor hypoxia by magnetic resonance methods", *NMR Biomed.*, vol. 24, pp. 1–16, 2011. DOI: `10.1002/nbm.1558`.

[15] M. Höckel and P. Vaupel, "Tumor hypoxia: Definitions and current clinical, biologic, and molecular aspects", *J. Natl. Cancer Inst.*, vol. 93, no. 4, pp. 266–276, 2001. DOI: `10.1093/jnci/93.4.266`.

[16] R. Grigoryan, N. Keshelava, C. Anderson, and C. P. Reynolds, "In vitro testing of chemosensitivity in physiological hypoxia", *Methods Mol. Med.*, vol. 110, no. 4, pp. 87–100, 2005. DOI: `10.1385/1-59259-869-2:087`.

[17] B. Gallez, C. Baudelet, and B. F. Jordan, "Assessment of tumor oxygenation by electron paramagnetic resonance: Principles and applications", *NMR Biomed.*, vol. 17, no. 5, pp. 240–262, 2004. DOI: `10.1002/nbm.900`.

[18] K. A. Hossmann, "The hypoxic brain. Insights from ischemia research", *Adv. Exp. Med. Biol.*, vol. 474, pp. 155–169, 1999.

[19] F. J. Giordano, "Oxygen, oxidative stress, hypoxia, and heart failure", *J. Clin. Invest.*, vol. 115, no. 3, pp. 500–508, 2005. DOI: `10.1172/JCI200524408.500`.

[20] H. M. Swartz and R. B. Clarkson, "The measurement of oxygen in vivo using EPR techniques", *Phys. Med. Biol.*, vol. 43, pp. 1957–1975, 1998. DOI: `10.1088/0031-9155/43/7/017`.

[21] H. M. Swartz, N. Khan, J. Buckey, R. Comi, L. Gould, O. Grinberg, A. Hartford, H. Hopf, H. Hou, E. Hug, A. Iwasaki, P. Lesniewski, I. Salikhov, and T. Walczak, "Clinical applications of EPR: Overview and perspectives", *NMR Biomed.*, vol. 17, no. 5, pp. 335–351, 2004. DOI: `10.1002/nbm.911`.

[22] C. M. Desmet, A. Lafosse, S. Veriter, P. E. Porporato, P. Sonveaux, D. Dufrane, P. Leveque, and B. Gallez, "Application of electron paramagnetic resonance (EPR) oximetry to monitor oxygen in wounds in diabetic models", *PLoS One*, vol. 10, no. 12, pp. 1–16, 2015. DOI: `10.1371/journal.pone.0144914`.

[23] S. Schreml, R. M. Szeimies, L. Prantl, S. Karrer, M. Landthaler, and P. Babilas, "Oxygen in acute and chronic wound healing", *Br. J. Dermatol.*, vol. 163, pp. 257–268, 2010. DOI: `10.1111/j.1365-2133.2010.09804.x`.

[24] H. M. Swartz, "Using EPR to measure a critical but often unmeasured component of oxidative damage: Oxygen", *Antioxid. Redox Signal.*, vol. 6, no. 3, pp. 677–686, 2004. DOI: 10.1089/152308604773934440.

[25] ——, "Measuring real levels of oxygen in vivo: Opportunities and challenges", *Biochem. Soc. Trans.*, vol. 30, no. 2, pp. 248–252, 2002. DOI: 10.1042/BST0300248.

[26] R. Ahmad and P. Kuppusamy, "Theory, instrumentation, and applications of electron paramagnetic resonance oximetry", *Chem. Rev.*, vol. 110, no. 5, pp. 3212–3236, 2010. DOI: 10.1021/cr900396q.

[27] R. P. Mason, D. Zhao, J. Pacheco-Torres, W. Cui, V. D. Kodibagkar, P. K. Gulaka, G. Hao, P. Thorpe, E. W. Hahn, and P. Peschke, "Multimodality imaging of hypoxia in preclinical settings", *Q. J. Nucl. Med. Mol. Imaging*, vol. 54, no. 3, pp. 259–280, 2010.

[28] G. Ilangovan, A. Bratasz, H. Li, P. Schmalbrock, J. L. Zweier, and P. Kuppusamy, "In vivo measurement and imaging of tumor oxygenation using coembedded paramagnetic particulates", *Magn. Reson. Med.*, vol. 52, no. 3, pp. 650–657, 2004. DOI: 10.1002/mrm.20188.

[29] L. J. Berliner and J. Reuben, *Spin labeling: Theory and applications.* Springer Science & Business Media, 2012. DOI: 10.1007/978-1-4613-0743-3.

[30] W. K. Subczynski and H. M. Swartz, "Chapter 10: EPR oximetry in biological and model samples", in *Biomed. EPR, Part A Free radicals, Met. Med. Physiol.* 2005, pp. 229–282. DOI: 10.1007/0-387-26741-7_10.

[31] P. Kuppusamy and J. L. Zweier, "Cardiac applications of EPR imaging", *NMR Biomed.*, vol. 17, pp. 226–239, 2004. DOI: 10.1002/nbm.912.

[32] B. Epel and H. J. Halpern, "In vivo pO2 imaging of tumors: Oxymetry with very low-frequency electron paramagnetic resonance", *Methods Enzymol.*, vol. 564, pp. 501–527, 2015. DOI: 10.1016/bs.mie.2015.08.017.

[33] N. Khan, B. B. Williams, H. Hou, H. Li, and H. M. Swartz, "Repetitive tissue pO2 measurements by electron paramagnetic resonance oximetry: Current status and future potential for experimental and clinical studies", *Antioxid. Redox Signal.*, vol. 9, no. 8, pp. 1169–1182, 2007. DOI: 10.1089/ars.2007.1635.

[34] H. Wolfson, R. Ahmad, Y. Twig, P. Kuppusamy, and A. Blank, "A miniature electron spin resonance probehead for transcutaneous oxygen monitoring", *Appl. Magn. Reson.*, vol. 45, no. 10, pp. 955–967, 2014. DOI: 10.1007/s00723-014-0593-8.

[35] H. M. Swartz, B. B. Williams, B. I. Zaki, A. C. Hartford, L. A. Jarvis, E. Y. Chen, R. J. Comi, M. S. Ernstoff, H. Hou, N. Khan, S. G. Swarts, A. B. Flood, and P. Kuppusamy, "Clinical EPR: Unique opportunities and some challenges", *Acad Radiol.*, vol. 21, no. 2, pp. 197–206, 2014. DOI: `doi:10.1016/j.acra.2013.10.011`.

[36] H. M. Swartz, H. Hou, N. Khan, L. A. Jarvis, E. Y. Chen, B. B. Williams, and P. Kuppusamy, "Advances in probes and methods for clinical EPR oximetry", *Adv Exp Med Biol.*, vol. 812, pp. 73–79, 2014. DOI: `10.1007/978-1-4939-0620-8`.

[37] L. J. Berliner, *In vivo EPR (ESR): Theory and application.* Springer US, 2003.

[38] A. Lund, M. Shiotani, and S. Shimada, *Principles and applications of ESR spectroscopy*, I. Springer Science & Business Media, 2011, p. 461. DOI: `10.1007/978-1-4020-5344-3`.

[39] D. J. Lurie and K. Mäder, "Monitoring drug delivery processes by EPR and related techniques - principles and applications", *Adv. Drug Deliv. Rev.*, vol. 57, pp. 1171–1190, 2005. DOI: `10.1016/j.addr.2005.01.023`.

[40] J. A. Weil and J. R. Bolton, *Electron paramagnetic resonance: Elementary theory and practical applications.* John Wiley & Sons, Inc., 2007, p. 688.

[41] *Nobel lectures, Physics 1901-1921.* Amsterdam: Elsevier Publishing Company, 1967.

[42] W. Gerlach and O. Stern, "Der experimentelle Nachweis der Richtungsquantelung im Magnetfeld", *Z. Phys.*, vol. 9, no. 1, pp. 349–352, 1922. DOI: `doi:10.1007/BF01326983`.

[43] O. Lombardi and D. Dieks, "Modal interpretations of quantum mechanics", in *Stanford Encycl. Philos.* Spring 201, Metaphysics Research Lab, Stanford University, 2017.

[44] J. Mehra, *The golden age of theoretical physics.* World Scientific, 2001, p. 1436.

[45] G. E. Uhlenbeck and S. Goudsmit, "Ersetzung der Hypothese vom unmechanischen Zwang durch eine Forderung bezueglich des inneren Verhaltens jedes einzelnen Elektrons", *Naturwissenschaften*, vol. 13, no. 47, pp. 953–954, 1925. DOI: `doi:10.1007/BF01558878`.

[46] E. Zavoisky, "Paramagnetic relaxation of liquid solutions for perpendicular fields", *J. Phys. USSR*, vol. 9, pp. 211–216, 1945.

[47] OpenStax, "Chapter 8: Advanced theories of covalent bonding", in *Chemistry (Easton).* OpenStax CNX, 2016.

[48] M. P. Eastman, R. G. Kooser, M. R. Das, and J. H. Freed, "Studies of Heisenberg spin exchange in ESR spectra. I. Linewidth and saturation effects", *J. Chem. Phys.*, vol. 51, no. 1969, pp. 2690–2709, 1969. DOI: 10.1063/1.1672395.

[49] M. J. N. Junk, "Chapter 2: Electron paramagnetic resonance theory", in *Assess. Funct. Struct. Mol. Transp. by EPR Spectrosc.* Springer, 2012, pp. 7–51. DOI: 10.1007/978-3-642-25135-1.

[50] J. R. Wright, W. A. Hendrickson, S. Osaki, and G. T. James, "Chapter 5: Electron spin resonance spectroscopy (ESR)", in *Phys. methods Inorg. Biochem.* Springer Science & Business Media, 2012. DOI: 10.1145/101328.101333.

[51] T. I. Smirnova, A. I. Smirnov, R. B. Clarkson, and R. Linn Belford, "Accuracy of oxygen measurements in T2 line width EPR oximetry", *Magn. Reson. Med.*, vol. 33, no. 6, pp. 801–810, 1995. DOI: 10.1002/mrm.1910330610.

[52] W. K. Subczynski and J. S. Hyde, "Diffusion of oxygen in water and hydrocarbons using an electron spin resonance spin-label technique", *Biophys. J.*, vol. 45, no. April, pp. 743–748, 1984. DOI: 10.1016/S0006-3495(84)84217-4.

[53] A. Dash, S. Singh, and J. Tolman, "Chapter 2: Physical states and thermodynamic principles in pharmaceutics", in *Pharm. Basic Princ. Appl. to Pharm. Pract.* Academic Press, 2013.

[54] F. Bensebaa and J. J. Andre, "Effect of oxygen on phthalocyanine radicals. 1. ESR study of lithium phthalocyanine spin species at different oxygen concentrations", *J. Phys. Chem.*, vol. 96, no. 14, pp. 5739–5745, 1992. DOI: 10.1021/j100193a016.

[55] G. Ilangovan, J. L. Zweier, and P. Kuppusamy, "Electrochemical preparation and EPR studies of lithium phthalocyanine. Part 2: Particle-size-dependent line broadening by molecular oxygen and its implications as an oximetry probe", *J. Phys. Chem. B*, vol. 104, no. 40, pp. 9404–9410, 2000. DOI: 10.1021/jp0013863.

[56] P. Turek, J.-J. Andre, A. Giraudeau, and J. Simon, "Preparation and study of a lithium phthalocyanine radical: optical and magnetic properties", *Chem. Phys. Lett.*, vol. 134, no. 5, pp. 471–476, 1987. DOI: 10.1016/0009-2614(87)87175-0.

[57] H. Sugimoto, M. Mori, H. Masuda, and T. Taga, "Synthesis and molecular structure of a lithium complex of the phthalocyanine radical", *J. Chem. Soc., Chem*, no. 12, pp. 962–963, 1986. DOI: 10.1039/c39860000962.

[58] R. P. Pandian, Y.-I. Kim, P. M. Woodward, J. L. Zweier, P. T. Manoharan, and P. Kuppusamy, "The open molecular framework of paramagnetic lithium octabutoxy-naphthalocyanine: implications for the detection of oxygen and nitric oxide using EPR spectroscopy", _J. Mater. Chem._, vol. 16, pp. 3609–3618, 2006. DOI: 10.1039/b517976a.

[59] R. P. Pandian, M. Dolgos, C. Marginean, P. M. Woodward, P. C. Hammel, P. T. Manoharan, and P. Kuppusamy, "Molecular packing and magnetic properties of lithium naphthalocyanine crystals: Hollow channels enabling permeability and paramagnetic sensitivity to molecular oxygen", _J. Mater. Chem._, vol. 19, no. 24, pp. 4138–4147, 2009. DOI: 10.1038/jid.2014.371.

[60] B. B. Williams and H. J. Halpern, "Chapter 11: In vivo EPR imaging", in _Biomed. EPR, Part A Free radicals, Met. Med. Physiol._ Springer Science & Business Media, 2005, pp. 283–313.

[61] P. Turek, J.-J. Andre, and J. Simon, "Extreme spin exchange narrowing in a neutral phthalocyanine radical: The lithium phthalocyanine", _Solid State Commun._, vol. 63, no. 8, pp. 741–744, 1987. DOI: 10.1016/0038-1098(87)90122-0.

[62] G. Ilangovan, J. L. Zweier, and P. Kuppusamy, "Mechanism of oxygen-induced EPR line broadening in lithium phthalocyanine microcrystals", _J. Magn. Reson._, vol. 170, no. 1, pp. 42–48, 2004. DOI: 10.1016/j.jmr.2004.05.018.

[63] H. Li, H. Hou, A. Sucheta, B. B. Williams, J. P. Lariviere, N. Khan, P. N. Lesniewski, B. Gallez, and H. M. Swartz, "Implantable resonators - a technique for repeated measurement of oxygen at multiple deep sites with in vivo EPR", _Adv. Exp. Med. Biol._, vol. 662, pp. 265–272, 2010. DOI: 10.1007/978-1-4419-1241-1_38.

[64] B. Driesschaert, P. Leveque, B. Gallez, and J. Marchand-Brynaert, "RGD-conjugated triarylmethyl radical as probe for electron paramagnetic imaging", _Tetrahedron Lett._, vol. 54, no. 44, pp. 5924–5926, 2013. DOI: 10.1016/j.tetlet.2013.08.120.

[65] S. R. Burks, J. Bakhshai, M. A. Makowsky, S. Muralidharan, P. Tsai, G. M. Rosen, and J. P. Y. Kao, "2H,15N-substituted nitroxides as sensitive probes for electron paramagnetic resonance imaging", _J. Org. Chem._, vol. 75, no. 19, pp. 6463–6467, 2010. DOI: 10.1021/jo1011619.

[66] I. Dhimitruka, O. Grigorieva, J. L. Zweier, and V. V. Khramtsov, "Synthesis, structure, and EPR characterization of deuterated derivatives of Finland trityl radical", *Bioorganic Med. Chem. Lett.*, vol. 20, no. 13, pp. 3946–3949, 2010. DOI: `10.1016/j.bmcl.2010.05.006`.

[67] B. Epel, G. Redler, and H. J. Halpern, "How in vivo EPR measures and images oxygen", vol. 812, pp. 113–119, 2014. DOI: `10.1007/978-1-4939-0620-8`.

[68] L. Yong, J. Harbridge, R. W. Quine, G. A. Rinard, S. S. Eaton, G. R. Eaton, C. Mailer, E. Barth, and H. J. Halpern, "Electron spin relaxation of triarylmethyl radicals in fluid solution", *J. Magn. Reson.*, vol. 152, no. 1, pp. 156–161, 2001. DOI: `10.1006/jmre.2001.2379`.

[69] I. Dhimitruka, M. Velayutham, A. A. Bobko, V. V. Khramtsov, F. A. Villamena, C. M. Hadad, and J. L. Zweier, "Large-scale synthesis of a persistent trityl radical for use in biomedical EPR applications and imaging", *Bioorganic Med. Chem. Lett.*, vol. 17, pp. 6801–6805, 2007. DOI: `10.1016/j.bmcl.2007.10.030`.

[70] M. Gomberg, "An instance of trivalent carbon: Triphenylmethyl", *J. Am. Chem. Soc.*, vol. 22, no. 11, pp. 757–771, 1900. DOI: `10.1021/ja02049a006`.

[71] S. Andersson, F. Radner, A. Rydbeek, R. Servin, and L.-G. Wistrand, *Free radicals*. US Patent, US5530140 A, 1996.

[72] S. Andersson, F. Radner, A. Rydbeck, R. Servin, and L.-G. Wistrand, *Free radicals*. US Patent, US5728370 A, 1998.

[73] Y. Liu, F. A. Villamena, and J. L. Zweier, "Highly stable dendritic trityl radicals as oxygen and pH probe", *Chem. Commun.*, pp. 4336–4338, 2008. DOI: `10.1039/b807406b`.

[74] M. Ballester, "Inert carbon free radicals", *Pure Appl. Chem.*, vol. 15, no. 1, pp. 123–125, 1967. DOI: `10.1351/pac196715010123`.

[75] M. Ballester, J. Riera-Figueras, J. Castaner, C. Badfa, and J. M. Monso, "Inert carbon free radicals. I. Perchlorodiphenylmethyl and perchlorotriphenylmethyl radical series", *J. Am. Chem. Soc.*, vol. 93, no. 9, pp. 2215–2225, 1971. DOI: `10.1021/ja00738a021`.

[76] M. Ballester, J. Riera, J. Castaner, A. Rodriguez, C. Rovira, and J. Veciana, "Inert carbon free radicals. 3. Monofunctionalized radicals from perchlorotriphenylcarbenium hexachloroantimonate", *J. Org. Chem.*, vol. 47, no. 23, pp. 4498–4505, 1982. DOI: `10.1021/jo00144a019`.

[77] A. Bratasz, A. C. Kulkarni, and P. Kuppusamy, "A highly sensitive biocompatible spin probe for imaging of oxygen concentration in tissues", *Biophys. J.*, vol. 92, no. 8, pp. 2918–2925, 2007. DOI: 10.1529/biophysj.106.099135.

[78] V. K. Kutala, N. L. Parinandi, R. P. Pandian, and P. Kuppusamy, "Simultaneous measurement of oxygenation in intracellular and extracellular compartments of lung microvascular endothelial cells", *Antioxid. Redox Signal.*, vol. 6, no. 3, pp. 597–603, 2004. DOI: 10.1089/152308604773934350.

[79] Y. Liu, F. A. Villamena, J. Sun, T.-y. Wang, and J. L. Zweier, "Esterified trityl radicals as intracellular oxygen probes", *Free Radic. Biol. Med.*, vol. 46, no. 7, pp. 876–883, 2009. DOI: 10.1016/j.freeradbiomed.2008.12.011.

[80] C. Rizzi, A. Samouilov, V. K. Kutala, N. L. Parinandi, J. L. Zweier, and P. Kuppusamy, "Application of a trityl-based radical probe for measuring superoxide", *Free Radic. Biol. Med.*, vol. 35, no. 12, pp. 1608–1618, 2003. DOI: 10.1016/j.freeradbiomed.2003.09.014.

[81] V. Dang, J. Wang, S. Feng, C. Buron, F. A. Villamena, P. G. Wang, and P. Kuppusamy, "Synthesis and characterization of a perchlorotriphenylmethyl (trityl) triester radical: A potential sensor for superoxide and oxygen in biological systems", *Bioorganic Med. Chem. Lett.*, vol. 17, pp. 4062–4065, 2007. DOI: 10.1016/j.bmcl.2007.04.070.

[82] V. K. Kutala, F. A. Villamena, G. Ilangovan, D. Maspoch, N. Roques, J. Veciana, C. Rovira, and P. Kuppusamy, "Reactivity of superoxide anion radical with a perchlorotriphenylmethyl (trityl) radical", *J. Phys. Chem. B*, vol. 112, no. 1, pp. 158–167, 2008. DOI: 10.1021/jp076656x.

[83] Y. Liu, Y. Song, F. D. Pascali, X. Liu, F. A. Villamena, and J. L. Zweier, "Tetrathiatriarylmethyl radical with a single aromatic hydrogen as a highly sensitive and specific superoxide probe", *Free Radic. Biol. Med.*, vol. 53, no. 11, pp. 2081–2091, 2012. DOI: 10.1016/j.freeradbiomed.2012.09.011.

[84] A. A. Bobko, I. Dhimitruka, J. L. Zweier, and V. V. Khramtsov, "Trityl radicals as persistent dual function pH and oxygen probes for in vivo electron paramagnetic resonance spectroscopy and imaging: Concept and experiment", *J. Am. Chem. Soc.*, vol. 129, no. 23, pp. 7240–7241, 2007. DOI: 10.1021/ja071515u.

[85] B. Driesschaert, V. Marchand, P. Leveque, B. Gallez, and J. Marchand-Brynaert, "A phosphonated triarylmethyl radical as a probe for measurement of pH by EPR", *Chem. Commun.*, vol. 48, no. 34, pp. 4049–4051, 2012. DOI: 10.1039/c2cc00025c.

[86] Y. Liu, F. A. Villamena, Y. Song, J. Sun, A. Rockenbauer, and J. L. Zweier, "Synthesis of 14N- and 15N-labeled trityl-nitroxide biradicals with strong spin-spin interaction and improved sensitivity to redox status and oxygen", *J. Org. Chem.*, vol. 75, no. 22, pp. 7796–7802, 2010. DOI: 10.1021/jo1016844.

[87] G. Y. Shevelev, O. A. Krumkacheva, A. A. Lomzov, A. A. Kuzhelev, O. Y. Rogozhnikova, D. V. Trukhin, T. I. Troitskaya, V. M. Tormyshev, M. V. Fedin, D. V. Pyshnyi, and E. G. Bagryanskaya, "Physiological-temperature distance measurement in nucleic acid using triarylmethyl-based spin labels and pulsed dipolar EPR spectroscopy", *J. Am. Chem. Soc.*, vol. 136, no. 28, pp. 9874–9877, 2014. DOI: 10.1021/ja505122n.

[88] A. A. Bobko, I. Dhimitruka, J. L. Zweier, and V. V. Khramtsov, "Fourier transform EPR spectroscopy of trityl radicals for multifunctional assessment of chemical microenvironment", *Angew. Chem.*, vol. 126, no. 10, pp. 2773–2776, 2014. DOI: 10.1002/anie.201310841.

[89] M. Elas, B. B. Williams, A. Parasca, C. Mailer, C. A. Pelizzari, M. A. Lewis, J. N. River, G. S. Karczmar, E. D. Barth, and H. J. Halpern, "Quantitative tumor oxymetric images from 4D electron paramagnetic resonance imaging (EPRI): Methodology and comparison with blood oxygen level-dependent (BOLD) MRI", *Magn. Reson. Med.*, vol. 49, no. 4, pp. 682–691, 2003. DOI: 10.1002/mrm.10408.

[90] Y. Deng, S. Petryakov, G. He, E. Kesselring, P. Kuppusamy, and J. L. Zweier, "Fast 3D spatial EPR imaging using spiral magnetic field gradient", *J. Magn. Reson.*, vol. 185, no. 2, pp. 283–290, 2007. DOI: 10.1016/j.jmr.2007.01.001.

[91] M. Serda, Y.-K. Wu, E. D. Barth, H. J. Halpern, and V. H. Rawal, "EPR imaging spin probe trityl radical Oxo63: A method for its isolation from animal effluent, redox chemistry of its quinone methide oxidation product, and in vivo application in a mouse", *Chem. Res. Toxicol.*, vol. 29, no. 12, pp. 2153–2156, 2016. DOI: 10.1021/acs.chemrestox.6b00277.

[92] Y. Liu, F. A. Villamena, J. Sun, Y. Xu, I. Dhimitruka, and J. L. Zweier, "Synthesis and characterization of ester-derivatized tetrathiatriarylmethyl radicals as intracellular oxygen probes", *J. Org. Chem.*, vol. 73, no. 4, pp. 1490–1497, 2008. DOI: 10.1021/jo7022747.

[93] J. F. Dunn and H. M. Swartz, "In vivo electron paramagnetic resonance oximetry with particulate materials", *Methods*, vol. 30, pp. 159–166, 2003. DOI: 10.1016/S1046-2023(03)00077-X.

[94]   R. P. Pandian, N. P. Raju, J. C. Gallucci, P. M. Woodward, A. J. Epstein, and P. Kuppusamy, "A new tetragonal crystalline polymorph of lithium octa-n-butoxy-naphthalocyanine (LiNc-BuO) radical: Structural, magnetic and oxygen-sensing properties", *Chem. Mater.*, vol. 22, pp. 6254–6262, 2010. DOI: `10.1021/cm101733h`.

[95]   B. B. Williams, N. Khan, B. Zaki, A. Hartford, M. S. Ernstoff, and H. M. Swartz, "Clinical electron paramagnetic resonance (EPR) oximetry using India Ink", *Adv. Exp. Med. Biol.*, vol. 662, pp. 149–156, 2010. DOI: `10.1007/978-1-4419-1241-1_21`.

[96]   G. Ilangovan, A. Manivannan, H. Li, H. Yanagi, J. L. Zweier, and P. Kuppusamy, "A naphthalocyanine-based EPR probe for localized measurements of tissue oxygenation", *Free Radic. Biol. Med.*, vol. 32, no. 2, pp. 139–147, 2002. DOI: `10.1016/S0891-5849(01)00784-5`.

[97]   R. P. Pandian, N. L. Parinandi, G. Ilangovan, J. L. Zweier, and P. Kuppusamy, "Novel particulate spin probe for targeted determination of oxygen in cells and tissues", *Free Radic. Biol. Med.*, vol. 35, no. 9, pp. 1138–1148, 2003. DOI: `10.1016/S0891-5849(03)00496-9`.

[98]   R. P. Pandian, M. Dolgos, V. Dang, J. Z. Sostaric, P. M. Woodward, and P. Kuppusamy, "Structure and oxygen-sensing paramagnetic properties of a new lithium 1,8,15,22-tetraphenoxyphthalocyanine radical probe for biological oximetry", *Chem. Mater.*, vol. 19, no. 14, pp. 3545–3552, 2007. DOI: `10.1021/cm070622k`.

[99]   R. P. Pandian, V. K. Kutala, A. Liaugminas, N. L. Parinandi, and P. Kuppusamy, "Lipopolysaccharide-induced alterations in oxygen consumption and radical generation in endothelial cells", *Mol. Cell. Biochem.*, vol. 278, no. 1-2, pp. 119–127, 2005. DOI: `10.1007/s11010-005-6936-x`.

[100] T. D. Eubank, R. D. Roberts, M. Khan, J. M. Curry, G. J. Nuovo, P. Kuppusamy, and C. B. Marsh, "GM-CSF inhibits breast cancer growth and metastasis by invoking an anti-angiogenic program in tumor-educated macrophages", *Cancer Reseach*, vol. 69, no. 5, pp. 2133–2140, 2009. DOI: `10.1158/0008-5472.CAN-08-1405`.

[101] H. Hou, N. Khan, M. Nagane, S. Gohain, E. Y. Chen, L. A. Jarvis, P. E. Schaner, B. B. Williams, A. B. Flood, H. M. Swartz, and P. Kuppusamy, "Skeletal muscle oxygenation measured by EPR oximetry using a highly sensitive polymer-

encapsulated paramagnetic sensor", *Adv Exp Med Biol.*, vol. 923, pp. 351–357, 2016.

[102] M. Ueno, S. Matsumoto, A. Matsumoto, S. Manda, I. Nakanishi, K.-i. Matsumoto, J. B. Mitchell, M. C. Krishna, and K. Anzai, "Effect of amifostine, a radiation-protecting drug, on oxygen concentration in tissue measured by EPR oximetry and imaging", *J. Clin. Biochem. Nutr.*, vol. 60, no. 3, pp. 151–155, 2017. DOI: `10.3164/jcbn.15`.

[103] A. Bratasz, R. P. Pandian, Y. Deng, S. Petryakov, J. C. Grecula, N. Gupta, and P. Kuppusamy, "In vivo imaging of changes in tumor oxygenation during growth and after treatment", *Magn. Reson. Med.*, vol. 57, pp. 950–959, 2007. DOI: `10.1002/mrm.21212`.

[104] H. Fujii, K.-i. Sakata, Y. Katsumata, R. Sato, M. Kinouchi, M. Someya, S.-i. Masunaga, M. Hareyama, H. M. Swartz, and H. Hirata, "Tissue oxygenation in a murine SCC VII tumor after X-ray irradiation as determined by EPR spectroscopy", *Radiother. Oncol.*, vol. 86, no. 3, pp. 354–360, 2008. DOI: `10.1016/j.radonc.2007.11.020`.

[105] M. Nagane, H. Yasui, T. Yamamori, S. Zhao, Y. Kuge, N. Tamaki, H. Kameya, H. Nakamura, H. Fujii, and O. Inanami, "Radiation-induced nitric oxide mitigates tumor hypoxia and radioresistance in a murine SCCVII tumor model", *Biochem. Biophys. Res. Commun.*, vol. 437, no. 3, pp. 420–425, 2013. DOI: `10.1016/j.bbrc.2013.06.093`.

[106] K. Selvendiran, A. Bratasz, M. L. Kuppusamy, M. F. Tazi, B. K. Rivera, and P. Kuppusamy, "Hypoxia induces chemoresistance in ovarian cancer cells by activation of signal transducer and activator of transcription 3", *Int. J. Cancer*, vol. 125, no. 9, pp. 2198–2204, 2009. DOI: `10.1002/ijc.24601.Hypoxia`.

[107] G. A. McCann, S. Naidu, K. S. Rath, H. K. Bid, B. J. Tierney, A. Suarez, S. Varadharaj, J. Zhang, K. Hideg, P. Houghton, P. Kuppusamy, D. E. Cohn, and K. Selvendiran, "Targeting constitutively-activated STAT3 in hypoxic ovarian cancer, using a novel STAT3 inhibitor", *Oncoscience*, vol. 1, no. 3, pp. 216–228, 2014. DOI: `10.18632/oncoscience.26`.

[108] A. A. Bobko, J. Evans, N. C. Denko, and V. V. Khramtsov, "Concurrent longitudinal EPR monitoring of tissue oxygenation, acidosis, and reducing capacity in mouse xenograft tumor models", *Cell Biochem. Biophys.*, vol. 75, no. 2, pp. 247–253, 2017. DOI: `10.1007/s12013-016-0733-x`.

[109]   X. Zhao, G. He, Y.-R. Chen, R. P. Pandian, P. Kuppusamy, and J. L. Zweier, "Endothelium-derived nitric oxide regulates postischemic myocardial oxygenation and oxygen consumption by modulation of mitochondrial electron transport", *Circulation*, vol. 111, pp. 2966–2972, 2005. DOI: `10.1161/CIRCULATIONAHA.104.527226`.

[110]   M. Hashem, M. Weiler-Sagie, P. Kuppusamy, G. Neufeld, M. Neeman, and A. Blank, "Electron spin resonance microscopic imaging of oxygen concentration in cancer spheroids", *J. Magn. Reson.*, vol. 256, pp. 77–85, 2015. DOI: `10.1016/j.jmr.2015.04.012`.

[111]   K. J. Liu, P. Gast, M. Moussavi, S. W. Norby, N. Vahidi, T. Walczak, M. Wu, and H. M. Swartz, "Lithium phthalocyanine: A probe for electron paramagnetic resonance oximetry in viable biological systems", *Proc. Natl. Acad. Sci. U. S. A.*, vol. 90, no. 12, pp. 5438–5442, 1993. DOI: `10.1073/pnas.90.12.5438`.

[112]   B. Gallez and K. Mäder, "Accurate and sensitive measurements of pO2 in vivo using low frequency EPR spectroscopy: How to confer biocompatibility to the oxygen sensors", *Free Radic. Biol. Med.*, vol. 29, no. 11, pp. 1078–1084, 2000. DOI: `10.1016/S0891-5849(00)00405-6`.

[113]   M. Dinguizli, N. Beghein, and B. Gallez, "Retrievable micro-inserts containing oxygen sensors for monitoring tissue oxygenation using EPR oximetry", *Physiol. Meas.*, vol. 29, pp. 1247–1254, 2008. DOI: `10.1088/0967-3334/29/11/001`.

[114]   S. Xia, F. A. Villamena, C. M. Hadad, P. Kuppusamy, Y. Li, H. Zhu, and J. L. Zweier, "Reactivity of molecular oxygen with ethoxycarbonyl derivatives of tetrathiatriarylmethyl radicals", *J. Org. Chem.*, vol. 71, no. 19, pp. 7268–7279, 2006. DOI: `10.1021/jo0610560`.

[115]   A. P. Jagtap, I. Krstic, N. C. Kunjir, R. Hänsel, T. F. Prisner, and S. T. Sigurdsson, "Sterically shielded spin labels for in-cell EPR spectroscopy: Analysis of stability in reducing environment", *Free Radic. Res.*, vol. 49, no. 1, pp. 78–85, 2015. DOI: `10.3109/10715762.2014.979409`.

[116]   J. H. Ardenkjaer-Larsen, I. Laursen, I. Leunbach, G. Ehnholm, L.-G. Wistrand, J. S. Petersson, and K. Golman, "EPR and DNP properties of certain novel single electron contrast agents intended for oximetric imaging", *J. Magn. Reson.*, vol. 133, pp. 1–12, 1998.

[117]   Y. Song, Y. Liu, W. Liu, F. A. Villamena, and J. L. Zweier, "Characterization of the binding of the Finland trityl radical with bovine serum albumin", *RSC Adv.*, vol. 4, pp. 47 649–47 656, 2014. DOI: `10.1039/C4RA04616A`.

[118] C. Decroos, J.-L. Boucher, D. Mansuy, and Y. Xu-Li, "Reactions of amino acids, peptides, and proteins with oxidized metabolites of tris(para-carboxyltetrathia-aryl)methyl radical EPR probes", *Chem. Res. Toxicol.*, vol. 27, no. 4, pp. 627–636, 2014. DOI: `dx.doi.org/10.1021/tx400467p`.

[119] V. Chechik and D. M. Murphy, *Electron paramagnetic resonance: Volume 25.* Royal Society of Chemistry, 2016, p. 235.

[120] J. He, N. Beghein, P. Ceroke, R. B. Clarkson, H. M. Swartz, and B. Gallez, "Development of biocompatible oxygen-permeable films holding paramagnetic carbon particles: Evaluation of their performance and stability in EPR oximetry", *Magn. Reson. Med.*, vol. 46, no. 3, pp. 610–614, 2001. DOI: `10.1002/mrm.1234`.

[121] M. Amann and O. Minge, "Biodegradability of poly(vinyl acetate) and related polymers", *Adv. Polym. Sci.*, vol. 245, pp. 137–172, 2012. DOI: `DOI:10.1007/12_2011_153`.

[122] S. Strübing, "Development and characterization of poly (vinyl acetate) based oral dosage forms", PhD thesis, Martin-Luther-Universität Halle-Wittenberg, Halle, 2008.

[123] E. Eteshola, R. P. Pandian, S. C. Lee, and P. Kuppusamy, "Polymer coating of paramagnetic particulates for in vivo oxygen-sensing applications", *Biomed. Microdevices*, vol. 11, pp. 379–387, 2009. DOI: `10.1007/s10544-008-9244-x`.

[124] K. Abbas, A. Boutier-Pischon, F. Auger, D. Francon, A. Almario, Y.-M. Frapart, D. Francon, A. Almario, and Y.-M. Frapart, "In vivo triarylmethyl radical stabilization through encapsulation in Pluronic F-127 hydrogel", *J. Magn. Reson.*, vol. 270, pp. 147–156, 2016. DOI: `10.1016/j.jmr.2016.07.009`.

[125] Y. Song, Y. Liu, C. Hemann, F. A. Villamena, and J. L. Zweier, "Esterified dendritic TAM radicals with very high stability and enhanced oxygen sensitivity", *J. Org. Chem.*, vol. 78, pp. 1371–1376, 2013. DOI: `10.1021/jo301849k`.

[126] W. Liu, J. Nie, X. Tan, H. Liu, N. Yu, G. Han, Y. Zhu, F. A. Villamena, Y. Song, J. L. Zweier, and Y. Liu, "Synthesis and characterization of PEGylated trityl radicals: Effect of PEGylation on physicochemical properties", *J. Org. Chem.*, vol. 82, no. 1, pp. 588–596, 2017. DOI: `10.1021/acs.joc.6b02590`.

[127] J. Z. Sostaric, R. P. Pandian, A. Bratasz, and P. Kuppusamy, "Encapsulation of a highly sensitive EPR active oxygen probe into sonochemically prepared microspheres", *J. Phys. Chem. B*, vol. 111, pp. 3298–3303, 2007. DOI: `10.1021/jp0682356`.

[128]   K. J. Liu, M. W. Grinstaff, J. Jiang, K. S. Suslick, H. M. Swartz, and W. Wang, "In vivo measurement of oxygen concentration using sonochemically synthesized microspheres", *Biophys. J.*, vol. 67, pp. 896–901, 1994. DOI: 10.1016/S0006-3495(94)80551-X.

[129]   N. Charlier, B. Driesschaert, N. Wauthoz, N. Beghein, V. Preat, K. Amighi, J. Marchand-Brynaert, and B. Gallez, "Nano-emulsions of fluorinated trityl radicals as sensors for EPR oximetry", *J. Magn. Reson.*, vol. 197, no. 2, pp. 176–180, 2009. DOI: 10.1016/j.jmr.2008.12.013.

[130]   I. Dhimitruka, Y. Alsayed Alzarie, C. Hemann, A. Samouilov, and J. L. Zweier, "Trityl radicals in perfluorocarbon emulsions as stable, sensitive, and biocompatible oximetry probes", *Bioorg. Med. Chem. Lett.*, 2016. DOI: 10.1016/j.bmcl.2016.10.066.

[131]   G. Meenakshisundaram, E. Eteshola, A. Blank, S. C. Lee, and P. Kuppusamy, "A molecular paramagnetic spin-doped biopolymeric oxygen sensor", *Biosens. Bioelectron.*, vol. 25, no. 10, pp. 2283–2289, 2010. DOI: 10.1016/j.bios.2010.03.011.

[132]   T. Ren, L. Cong, Y. Wang, Y. Tang, B. Tian, X. Lin, Y. Zhang, and X. Tang, "Lipid emulsions in parenteral nutrition: current applications and future developments", *Expert Opin. Drug Deliv.*, vol. 10, no. 11, pp. 1533–1549, 2013.

[133]   J. C. Walton, "Analysis of radicals by EPR", in *Encycl. radicals Chem. Biol. Mater.* 2012.

[134]   A. Kogan and N. Garti, "Microemulsions as transdermal drug delivery vehicles", *Adv. Colloid Interface Sci.*, vol. 123-126, pp. 369–385, 2006. DOI: 10.1016/j.cis.2006.05.014.

[135]   B. Gallez, B. F. Jordan, and C. Baudelet, "Microencapsulation of paramagnetic particles by pyrroxylin to preserve their responsiveness to oxygen when used as sensors for in vivo EPR oximetry", *Magn. Reson. Med.*, vol. 42, pp. 193–196, 1999. DOI: 10.1002/(SICI)1522-2594(199907)42:1<193::AID-MRM25>3.0.CO;2-C.

[136]   M. Dinguizli, S. Jeumont, N. Beghein, J. He, T. Walczak, P. N. Lesniewski, H. Hou, O. Y. Grinberg, A. Sucheta, H. M. Swartz, and B. Gallez, "Development and evaluation of biocompatible films of polytetrafluoroethylene polymers holding lithium phthalocyanine crystals for their use in EPR oximetry", *Biosens. Bioelectron.*, vol. 21, pp. 1015–1022, 2006. DOI: 10.1016/j.bios.2005.03.009.

[137] G. Meenakshisundaram, E. Eteshola, R. P. Pandian, A. Bratasz, S. C. Lee, and P. Kuppusamy, "Fabrication and physical evaluation of a polymer-encapsulated paramagnetic probe for biomedical oximetry", *Biomed. Microdevices*, vol. 11, no. 4, pp. 773–782, 2009. DOI: `10.1007/s10544-009-9292-x`.

[138] R. P. Pandian, G. Meenakshisundaram, A. Bratasz, E. Eteshola, S. C. Lee, and P. Kuppusamy, "An implantable Teflon chip holding lithium naphthalocyanine microcrystals for secure, safe, and repeated measurements of pO2 in tissues", *Biomed. Microdevices*, vol. 12, no. 3, pp. 381–387, 2010. DOI: `10.1007/s10544-009-9394-5`.

[139] G. Meenakshisundaram, E. Eteshola, R. P. Pandian, A. Bratasz, K. Selvendiran, S. C. Lee, M. C. Krishna, H. M. Swartz, and P. Kuppusamy, "Oxygen sensitivity and biocompatibility of an implantable paramagnetic probe for repeated measurements of tissue oxygenation", *Biomed. Microdevices*, vol. 11, no. 4, pp. 817–826, 2009. DOI: `10.1007/s10544-009-9298-4`.

[140] G. Meenakshisundaram, R. P. Pandian, E. Eteshola, S. C. Lee, and P. Kuppusamy, "A paramagnetic implant containing lithium naphthalocyanine microcrystals for high-resolution biological oximetry", *J. Magn. Reson.*, vol. 203, no. 1, pp. 185–189, 2010. DOI: `10.1016/j.jmr.2009.11.016`.

[141] J. He, N. Beghein, R. B. Clarkson, H. M. Swartz, and B. Gallez, "Microencapsulation of carbon particles used as oxygen sensors in EPR oximetry to stabilize their responsiveness to oxygen in vitro and in vivo", *Phys. Med. Biol.*, vol. 46, pp. 3323–3329, 2001. DOI: `10.1088/0031-9155/46/12/317`.

[142] V. P. Bhallamudi, R. Xue, C. M. Purser, K. F. Presley, Y. K. Banasavadi-Siddegowda, J. Hwang, B. Kaur, P. C. Hammel, M. G. Poirier, J. J. Lannutti, and R. P. Pandian, "Nanofiber-based paramagnetic probes for rapid, real-time biomedical oximetry", *Biomed. Microdevices*, vol. 18, no. 2, p. 38, 2016. DOI: `10.1007/s10544-016-0063-1`.

[143] J. Frank, M. Elewa, M. M. Said, H. A. El Shihawy, M. El-Sadek, D. Müller, A. Meister, G. Hause, S. Drescher, H. Metz, P. Imming, and K. Mäder, "Synthesis, characterization, and nanoencapsulation of tetrathiatriarylmethyl and tetrachlorotriarylmethyl (trityl) radical derivatives - A study to advance their applicability as in vivo EPR oxygen sensors", *J. Org. Chem.*, vol. 80, no. 13, pp. 6754–6766, 2015. DOI: `10.1021/acs.joc.5b00918`.

[144] M. A. E.-m. M. Elewa, "Synthesis, EPR characterization and chitosan labelling of triarylmethyl radicals", PhD thesis, Martin-Luther-Universität Halle-Wittenberg, 2015.

[145] Council of Europe, "Monographs", in *Eur. Pharmacopoeia 7th ed. 7.0*, Strasbourg, 2011, p. 2759.

[146] P. Workman, E. O. Aboagye, F. Balkwill, A. Balmain, G. Bruder, D. J. Chaplin, J. A. Double, J. Everitt, D. A. H. Farningham, M. J. Glennie, L. R. Kelland, V. Robinson, I. J. Stratford, G. M. Tozer, S. Watson, S. R. Wedge, and S. A. Eccles, "Guidelines for the welfare and use of animals in cancer research", *Br. J. Cancer*, vol. 102, no. 11, pp. 1555–1577, 2010. DOI: `10.1038/sj.bjc.6605642`.

[147] Council of Europe, "General notices", in *Eur. Pharmacopoeia 8th ed. Suppl. 8.2*. Strasbourg, 2014, p. 3900.

[148] H. Fessi, F. Puisieux, J. Devissaguet, N. Ammoury, and S. Benita, "Nanocapsule formation by interfacial polymer deposition following solvent displacement", *Int. J. Pharm.*, vol. 55, R1–R4, 1989. DOI: `10.1016/0378-5173(89)90281-0`.

[149] S.-H. Hyon and Y. Ikada, *Polylactic acid type microspheres containing physiologically active substance and process for preparing the same*. Eur. Patent, 0330180, 1989.

[150] A. Rübe and K. Mäder, "Electron spin resonance study on the dynamics of polymeric nanocapsules", *J. Biomed. Nanotechnol.*, vol. 1, pp. 208–213, 2005.

[151] J. Frank, D. Gündel, S. Drescher, O. Thews, and K. Mäder, "Injectable LiNc-BuO loaded microspheres as in vivo EPR oxygen sensors after co-implantation with tumor cells", *Free Radic. Biol. Med.*, vol. 89, pp. 741–749, 2015. DOI: `10.1016/j.freeradbiomed.2015.10.401`.

[152] M. Elewa, N. Maltar-Strmecki, M. M. Said, H. A. El Shihawy, M. El-Sadek, J. Frank, S. Drescher, M. Drescher, K. Mäder, D. Hinderberger, and P. Imming, "Synthesis and EPR-spectroscopic characterization of the perchlorotriarylmethyl tricarboxylic acid radical (PTMTC) and its 13C labelled analogue (13C-PTMTC)", *Phys. Chem. Chem. Phys.*, vol. 19, no. 9, pp. 6688–6697, 2017. DOI: `10.1039/C6CP07200C`.

[153] P. Vaupel, F. Kallinowski, and P. Okunieff, "Blood flow, oxygen and nutrient supply, and metabolic microenvironment of human tumors: A review", vol. 49, pp. 6449–6465, 1989.

[154] R. Battino, T. R. Rettich, and T. Tominaga, *The solubility of oxygen and ozone in liquids*, 1983. DOI: 10.1063/1.555680.

[155] Glycerine Producer's Association, *Physical properties of glycerol and its solutions.* 1963, pp. 1–27.

[156] I. Kutsche, G. Giidehaus, D. Schuller, and A. Schumpe, "Aqueous Alcohol Solutions", *J. Chem. Eng. Data*, vol. 29, no. 3, pp. 286–287, 1984.

[157] E. Joubert-Huebner, a. Gerdes, and H.-H. Sievers, "An in vitro evaluation of a new cannula tip design compared with two clinically established cannula-tip designs regarding aortic arch vessel perfusion characteristics", *Perfusion*, vol. 15, no. 1, pp. 69–76, 2000. DOI: 10.1177/026765910001500110.

[158] R. Stößer and W. Herrmann, "Isotope effects in ESR spectroscopy", *Molecules*, vol. 18, no. 6, pp. 6679–6722, 2013. DOI: 10.3390/molecules18066679.

[159] M. Montalti, A. Credi, L. Prodi, and M. T. Gandolfi, "Solvent properties", in *Handb. Photochem. third ed.* 2006, pp. 535–559.

[160] R. Battino, "Oxygen and ozone", in *Solubility Data Ser.* Vol. 7, 1981.

[161] A. Rübe, G. Hause, K. Mäder, and J. Kohlbrecher, "Core-shell structure of miglyol poly(D,L-lactide) poloxamer nanocapsules studied by small-angle neutron scattering", *J. Control. Release*, vol. 107, no. 2, pp. 244–252, 2005. DOI: 10.1016/j.jconrel.2005.06.005.

[162] N. F. S. De Melo, R. Grillo, V. A. Guilherme, D. R. De Araujo, E. De Paula, A. H. Rosa, and L. F. Fraceto, "Poly(lactide-co-glycolide) nanocapsules containing benzocaine: Influence of the composition of the oily nucleus on physico-chemical properties and anesthetic activity", *Pharm. Res.*, vol. 28, pp. 1984–1994, 2011. DOI: 10.1007/s11095-011-0425-6.

[163] C. Kroll, "Analytik, Stabilität und Biotransformation von Spinsonden", PhD thesis, Humboldt-Universität zu Berlin, 1999.

[164] P. B. O'Donnell and J. W. McGinity, "Preparation of microspheres by the solvent evaporation technique", *Adv. Drug Deliv. Rev.*, vol. 28, pp. 25–42, 1997. DOI: 10.1016/S0169-409X(97)00049-5.

[165] C. Wischke and S. P. Schwendeman, "Principles of encapsulating hydrophobic drugs in PLA/PLGA microparticles", *Int. J. Pharm.*, vol. 364, no. 2, pp. 298–327, 2008. DOI: 10.1016/j.ijpharm.2008.04.042.

[166] R. P. Pandian, V. Dang, P. T. Manoharan, J. L. Zweier, and P. Kuppusamy, "Effect of nitrogen dioxide on the EPR property of lithium octa-n-butoxy 2,3-naphthalocyanine (LiNc-BuO) microcrystals", *J. Magn. Reson.*, vol. 181, no. 1, pp. 154–161, 2006. DOI: 10.1016/j.jmr.2006.04.004.

[167] J. Thomas and T. Gemming, *Analytical transmission electron microscopy: An introduction for operators.* Springer Science & Business, 2014, p. 152.

[168] D. B. Williams and c. B. Carter, *Transmission electron microscopy: A textbook for materials science, Band 2.* Springer Science & Business Media, 2009, p. 373.

[169] I. M. Watt, *The principles and practice of electron microscopy.* Cambridge University Press, 1997, p. 190.

[170] B. Fultz and J. M. Howe, "Diffraction contrast in TEM images", in *Transm. electron Microsc. diffractometry Mater.* 4. ed., 2013, p. 340.

[171] N. J. Severs, "Freeze-fracture electron microscopy", *Nat. Protoc.*, vol. 2, no. 3, pp. 547–576, 2007. DOI: 10.1038/nprot.2007.55.

[172] L. Isa, F. Lucas, R. Wepf, and E. Reimhult, "Measuring single-nanoparticle wetting properties by freeze-fracture shadow-casting cryo-scanning electron microscopy", *Nat. Commun.*, vol. 2, no. 438, pp. 1–9, 2011. DOI: 10.1038/ncomms1441.

[173] S. Beck, *Design of oxygen sensitive nanocrystals for in vivo oxygen monitoring*, Diploma thesis, Martin-Luther-Universität Halle-Wittenberg, 2017.

[174] U. Olsher, R. M. Izatt, J. S. Bradshaw, and N. K. Dalley, "Coordination chemistry of lithium ion: A crystal and molecular structure review", *Chem. Rev.*, vol. 91, no. 2, pp. 137–164, 1991. DOI: 10.1038/167434a0.

[175] E. Sada, T. Morisue, and K. Miyahara, "Salt effect in vapor-liquid equilibrium", *J. Chem. Eng.*, vol. 20, no. 3, pp. 283–287, 1969.

[176] S. D. Steichen, M. Caldorera-Moore, and N. A. Peppas, "A review of current nanoparticle and targeting moieties for the delivery of cancer therapeutics", *Eur. J. Pharm. Sci.*, vol. 48, no. 3, pp. 416–427, 2013. DOI: 10.1016/j.ejps.2012.12.006..

[177] R. A. Jain, "The manufacturing techniques of various drug loaded biodegradable poly(lactide-co-glycolide) (PLGA) devices", *Biomaterials*, vol. 21, pp. 2475–2490, 2000. DOI: 10.1016/S0142-9612(00)00115-0.

[178] M. Ye, S. Kim, and K. Park, "Issues in long-term protein delivery using biodegradable microparticles", *J. Control. Release*, vol. 146, no. 2, pp. 241–260, 2010. DOI: 10.1016/j.jconrel.2010.05.011.

[179] B. K. Kim, S. J. Hwang, J. B. Park, and H. J. Park, "Preparation and characterization of drug-loaded polymethacrylate microspheres by an emulsion solvent evaporation method", *J. Microencapsul.*, vol. 19, no. 6, pp. 811–822, 2002. DOI: `10.1080/0265204021000022770`.

[180] R. Arshady, "Preparation of biodegradable microspheres and microcapsules: 2. Polyactides and related polyesters", *J. Control. Release*, vol. 17, no. 1, pp. 1–21, 1991. DOI: `10.1016/0168-3659(91)90126-X`.

[181] M. N. Vrancken and D. A. Claeys, *Process for encapsulating water and compounds in aqueous phase by evaporation.* US Patent, 3523906 A, 1970.

[182] L. R. Beck, D. R. Cowsar, D. H. Lewis, R. J. Cosgrove, C. T. Riddle, S. L. Lowry, and T. Epperly, "A new long-acting injectable microcapsule system for the administration of progesterone", *Fertil. Steril.*, vol. 31, no. 5, pp. 545–551, 1979.

[183] R. Jalil and J. R. Nixon, "Microencapsulation using poly (L-lactic acid) II: Preparative variables affecting microcapsule properties", *J. Microencapsul.*, vol. 7, no. 1, pp. 25–39, 1990. DOI: `10.3109/02652049009028421`.

[184] D. C. Tsai, S. A. Howard, T. F. Hogan, C. J. Malanga, S. J. Kandzari, and J. K. H. Ma, "Preparation and in vitro evaluation of polylactic acid-mitomycin C microcapsules", *J. Microencapsul.*, vol. 3, no. 3, pp. 181–193, 1986. DOI: `10.3109/02652048609031572`.

[185] R. Jalil and J. R. Nixon, "Microencapsulation using poly(L-lactic acid) I: Microcapsule properties affected by the preparative technique", *J. Microencapsul.*, vol. 6, no. 4, pp. 473–484, 1989. DOI: `10.3109/02652048909031167`.

[186] R. Wada, S. H. Hyon, and Y. Ikada, "Lactic acid oligomer microspheres containing hydrophilic drugs", *J. Pharm. Sci.*, vol. 79, no. 10, pp. 919–924, 1990. DOI: `10.1002/jps.2600791016`.

[187] C. Sturesson, J. Carlfors, K. Edsman, and M. Andersson, "Preparation of biodegradable poly(lactic-co-glycolic) acid microspheres and their in vitro release of timolol maleate", *Int. J. Pharm.*, vol. 89, pp. 235–244, 1993. DOI: `10.1016/0378-5173(93)90249-F`.

[188] M. Iwata and J. W. McGinity, "Preparation of multi-phase microspheres of poly-(D,L-lactic acid) and poly(D,L-lactic-co-glycolic acid) containing a w/o emulsion by a multiple emulsion solvent evaporation technique", *J. Microencapsul.*, vol. 9, no. 2, pp. 201–214, 1992. DOI: `10.3109/02652049109021237`.

[189] K. R. Rao, P. Senapati, and M. K. Das, "Formulation and in vitro evaluation of ethyl cellulose microspheres containing zidovudine", *J. Microencapsul.*, vol. 22, no. 8, pp. 863–876, 2005. DOI: 10.1080/02652040500273498.

[190] S. K. Sahoo, A. A. Mallick, B. B. Barik, and P. C. Senapati, "Preparation and in vitro evaluation of ethyl cellulose microspheres containing stavudine by the double emulsion method", *Pharmazie*, vol. 62, no. 2, pp. 117–121, 2007. DOI: 10.1691/ph.2007.2.6076.

[191] K. J. Zhu, J. X. Zhang, C. Wang, H. Yasuda, A. Ichimaru, and K. Yamamoto, "Preparation and in vitro release behaviour of 5-fluorouracil-loaded microspheres based on poly (L-lactide) and its carbonate copolymers", *J. Microencapsul.*, vol. 20, no. 6, pp. 731–743, 2003. DOI: 10.3109/02652040309178084.

[192] R. Jalil and J. R. Nixon, "Microencapsulation using poly(DL-lactic acid) I: Effect of preparative variables on the microcapsule characteristics and release kinetics", *J. Microencapsul.*, vol. 7, no. 2, pp. 229–244, 1990. DOI: 10.3109/02652049009021836.

[193] D. S. Vikram, R. Ahmad, R. P. Pandian, S. Petryakov, and P. Kuppusamy, "Evaluation of oxygen-response times of phthalocyanine-based crystalline paramagnetic spin probes for EPR oximetry", *J. Magn. Reson.*, vol. 193, no. 1, pp. 127–132, 2008. DOI: 10.1016/j.jmr.2008.04.034.

[194] W. J. Rogers, "The effects of sterilization on medical materials and welded devices", in *Join. Assem. Med. Mater. Devices*, 2013, p. 115. DOI: \linebreak10.1533/9780857096425.1.79.

[195] D. Plester, "Effects of radiation sterilization on plastics", in *Steriliz. Technol.* Durham, USA: Duke Univ Press., 1973, p. 151.

[196] L. K. Massey, *The effect of sterilization methods on plastics and elastomers: : The definitive user's guide and databook*, 2nd ed. Norwich, N.Y.: William Andrew Pub., 2005, p. 7.

[197] International Atomic Energy Agency, *Controlling of degradation effects in radiation processing of polymers*, IAEA TECDO. Vienna, 2009, p. 184.

[198] R. Surana, A. Pyne, M. Rani, and R. Suryanarayanan, "Measurement of enthalpic relaxation by differential scanning calorimetry - Effect of experimental conditions", *Thermochim. Acta*, vol. 433, no. 1-2, pp. 173–182, 2005. DOI: 10.1016/j.tca.2005.02.014.

[199] L. C. E. Struik, *Physical aging in plastics and other glassy materials*, 1977. DOI: 10.1002/pen.760170305.

[200] A. Matsumoto, S. Matsumoto, A. L. Sowers, J. W. Koscielniak, N. J. Trigg, P. Kuppusamy, J. B. Mitchell, S. Subramanian, M. C. Krishna, and K.-i. Matsumoto, "Absolute oxygen tension (pO2) in murine fatty and muscle tissue as determined by EPR", *Magn. Reson. Med.*, vol. 54, pp. 1530–1535, 2005. DOI: 10.1002/mrm.20714.

[201] G. Helmlinger, F. Yuan, M. Dellian, and R. K. Jain, "Interstitial pH and pO2 gradients in solid tumors in vivo: High-resolution measurements reveal a lack of correlation", *Nat. Med.*, vol. 3, no. 2, pp. 177–182, 1997. DOI: 10.1038/nm0297-177.

[202] P. DiEgidio, H. I. Friedman, R. G. Gourdie, A. E. Riley, M. J. Yost, and R. L. Goodwin, "Biomedical implant capsule formation: Lessons learned and the road ahead", *Ann. Plast. Surg.*, vol. 73, no. 4, pp. 451–460, 2014. DOI: 10.1097/SAP.0000000000000287.

[203] J. M. Anderson, "Biological responses to materials", *Annu. Rev. Mater. Res.*, vol. 31, pp. 81–110, 2001. DOI: 10.1146/annurev.matsci.31.1.81.

[204] H. K. Eltzschig and P. Carmeliet, "Hypoxia and inflammation", *N. Engl. J. Med.*, vol. 364, no. 7, pp. 656–665, 2011. DOI: 10.1056/NEJMra0910283.

[205] J. Biddlestone, D. Bandarra, and S. Rocha, "The role of hypoxia in inflammatory disease", *Int. J. Mol. Med.*, vol. 35, no. 4, pp. 859–869, 2015. DOI: 10.3892/ijmm.2015.2079.

[206] S. Halin, S. H. Rudolfsson, N. Van Rooijen, and A. Bergh, "Extratumoral macrophages promote tumor and vascular growth in an orthotopic rat prostate tumor model", *Neoplasia*, vol. 11, no. 2, pp. 177–186, 2009. DOI: 10.1593/neo.81338.

[207] O. Thews and P. Vaupel, "Spatial oxygenation profiles in tumors during normo- and hyperbaric hyperoxia", *Strahlentherapie und Onkol.*, pp. 1–8, 2015. DOI: 10.1007/s00066-015-0867-6.

[208] S. S. Eaton and G. R. Eaton, "Chapter 5: The world as viewed by and with unpaired electrons", *J. Magn. Reson.*, vol. 223, pp. 151–163, 2012. DOI: 10.1016/j.jmr.2012.07.025.

[209] P. Svendsen and A. M. Carter, "Influence of injectable anaesthetic combinations on blood gas tensions and acid - base status in laboratory rats", *Acta pharmacol. toxicol.*, vol. 57, no. 1, pp. 1–7, 1985.

[210] M. Brun-Pascaud, C. Gaudebout, M. C. Blayo, and J. J. Pocidalo, "Arterial blood gases and acid-base status in awake rats", _Respir. Physiol._, vol. 48, no. 1, pp. 45–57, 1982.

[211] D. S. Vikram, A. Bratasz, R. Ahmad, and P. Kuppusamy, "A comparative evaluation of EPR and Oxylite oximetry using a random sampling of pO2 in a murine tumor", _Radiat. Res._, vol. 168, no. 3, pp. 308–315, 2007. DOI: `10.1667/RR0854.1`.

[212] J. A. O'Hara, H. Hou, E. Demidenko, R. J. Springett, N. Khan, and H. M. Swartz, "Simultaneous measurement of rat brain cortex PtO2 using EPR oximetry and a fluorescence fiber-optic sensor during normoxia and hyperoxia", _Physiol. Meas._, vol. 26, pp. 203–213, 2005. DOI: `10.1088/0967-3334/26/3/006`.

[213] O. Thews, M. Nowak, C. Sauvant, and M. Gekle, "Hypoxia-induced extracellular acidosis increases p-glycoprotein activity and chemoresistance in tumors in vivo via p38 signaling pathway", _Adv Exp Med Biol._, vol. 701, pp. 115–122, 2011. DOI: `10.1007/978-1-4419-7756-4_16`.

[214] Z. Wang, M.-Y. Su, and O. Nalcioglu, "Applications of dynamic contrast enhanced MRI in oncology: Measurement of tumor oxygen tension", _Technol. Cancer Res. Treat._, vol. 1, no. 1, pp. 29–38, 2002.

[215] A. J. Varghese, S. Gulyas, and J. K. Mohindra, "Hypoxia-dependent reduction of 1-(2-nitro-1-imidazolyl)-3-methoxy-2-propanol by Chinese hamster ovary cells and KHT tumor cells in vitro and in vivo", _Cancer Res._, vol. 36, no. 10, pp. 3761–3765, 1976.

[216] P. L. Olive, R. E. Durand, J. A. Raleigh, C. Luo, and C. Aquino-Parsons, "Comparison between the comet assay and pimonidazole binding for measuring tumour hypoxia", _Br. J. Cancer_, vol. 83, no. 11, pp. 1525–1531, 2000. DOI: `10.1054/bjoc.2000.1489`.

[217] P. Mahy, M. De Bast, B. Gallez, J. Gueulette, C. J. Koch, P. Scalliet, and V. Grégoire, "In vivo colocalization of 2-nitroimidazole EF5 fluorescence intensity and electron paramagnetic resonance oximetry in mouse tumors", _Radiother. Oncol._, vol. 67, pp. 53–61, 2003. DOI: `10.1016/S0167-8140(03)00028-8`.

[218] M. Sandor, J. Harris, and E. Mathiowitz, "A novel polyethylene depot device for the study of PLGA and P(FASA) microspheres in vitro and in vivo", _Biomaterials_, vol. 23, pp. 4413–4423, 2002. DOI: `10.1016/S0142-9612(02)00183-7`.

Appendices

A Supporting information

^{1}H NMR spetrum of PVAc isolated from Kollicoat$^{®}$ SR 30 D
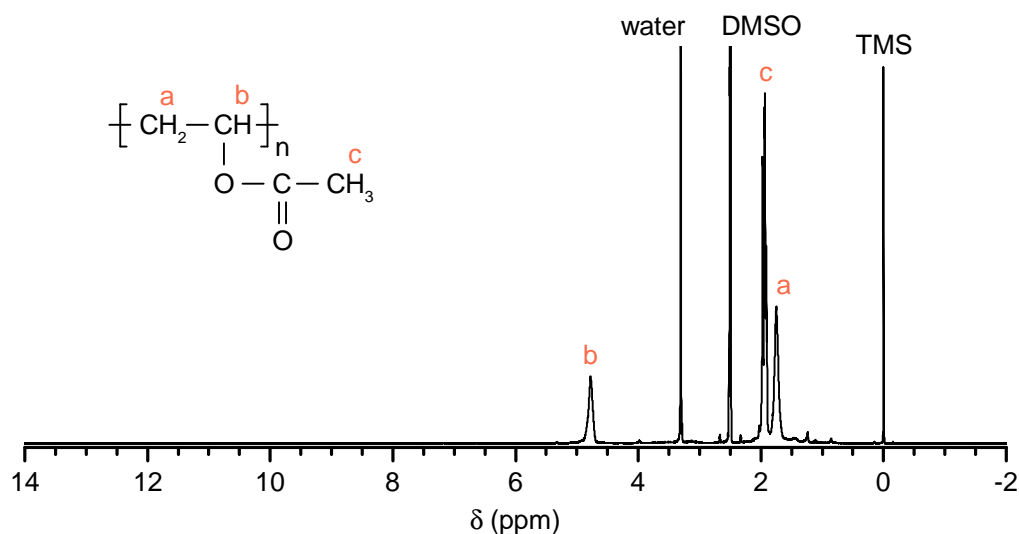
Figure A.1: ^{1}H NMR spectrum of isolated PVAc as measured in deuterated DMSO. Chemical shifts δ are reported in ppm relative to the peak position of TMS. Note that the DMSO peak was assigned to protons in residual partly undeuterated DMSO, the water peak was due to absorption of moisture during sample preparation. PVAc peaks were assigned to the corresponding protons as follows: (a) β protons in methylene group, (b) α protons in methine group (c) protons in acetyl group (see chemical formula of PVAc above).

Concentration calibration curves of LiNc-BuO

(a) EPR spectroscopy.

(b) UV/Vis spectroscopy.
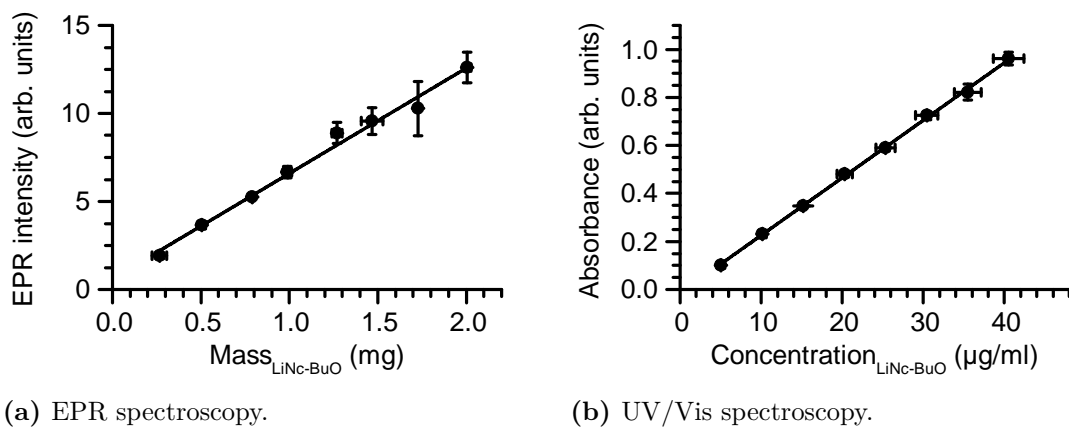
Figure A.2: Calibration curves for quantification of LiNc-BuO, batch 1 ($n = 4$, lines: linear regressions).

Temperature dependence of the oxygen sensitivity of LiNc-BuO
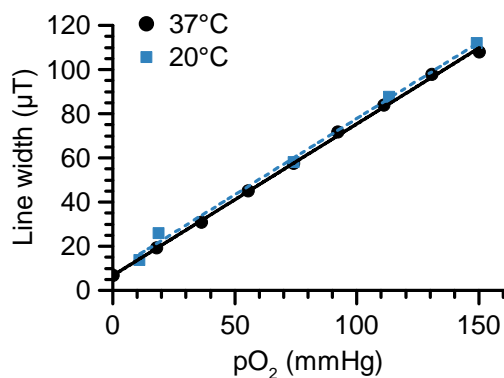
Figure A.3: Oxygen calibration curves of dry LiNc-BuO (batch 1) crystals at 20 °C and 37 °C (lines: linear regression).

Mass spectra of LiNc-BuO and Nc-BuO
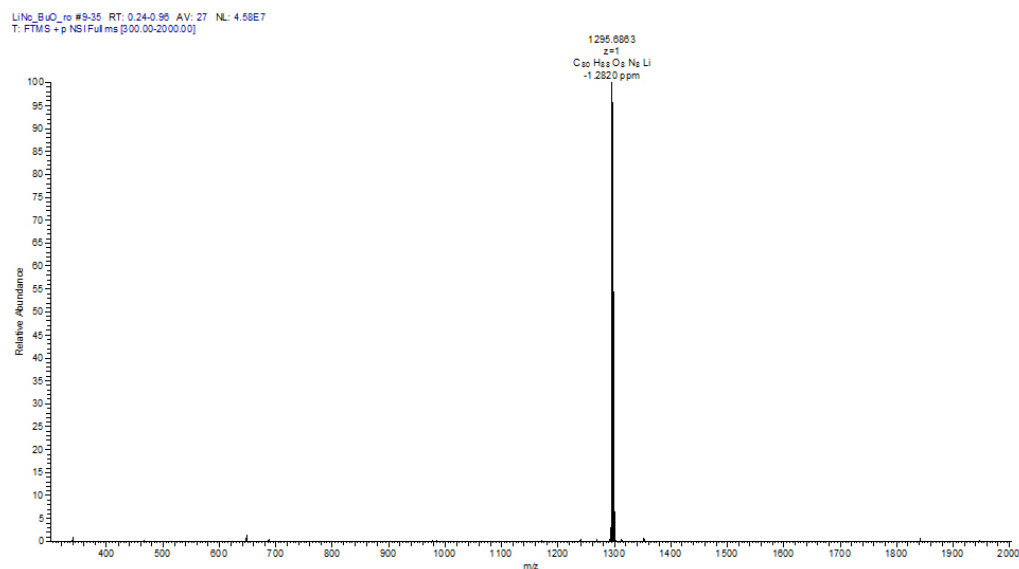
Figure A.4: Mass spectrum of LiNc-BuO, batch 1.
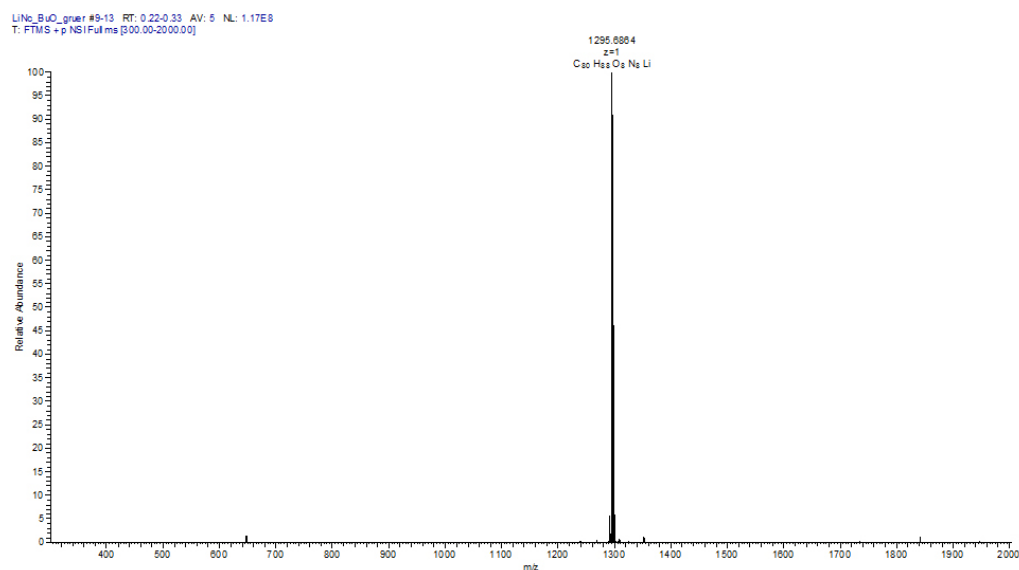
Figure A.5: Mass spectrum of LiNc-BuO, batch 2.
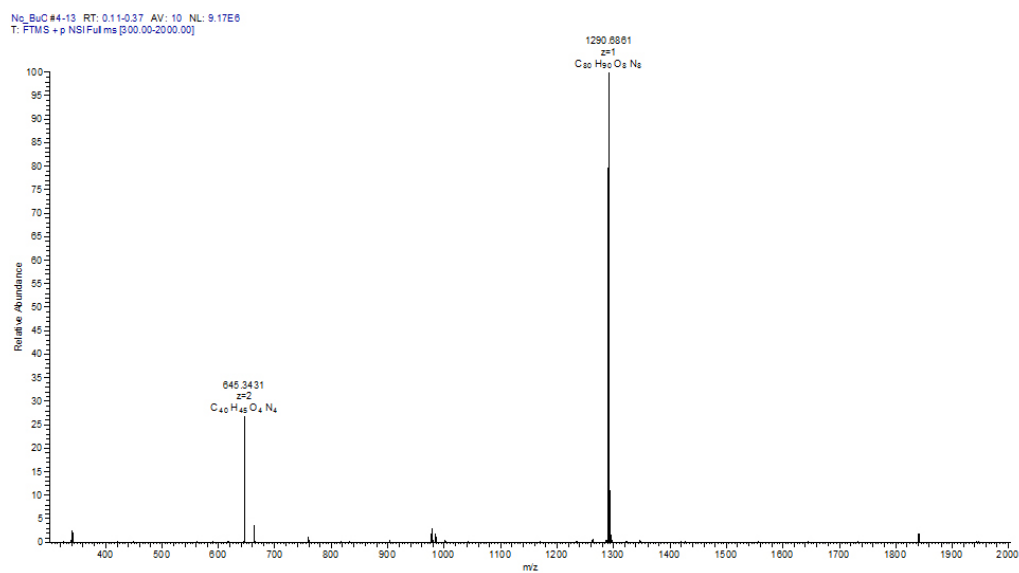
Figure A.6: Mass spectrum of Nc-BuO.

DSC thermogram of LiNc-BuO NPs prepared by nanomilling
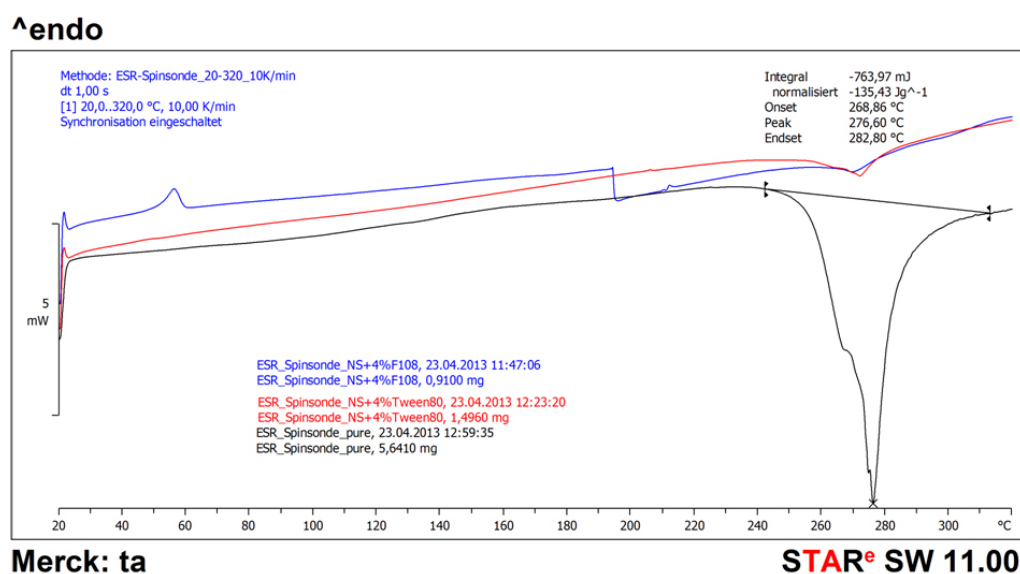
Figure A.7: DSC thermogram of LiNc-BuO NPs prepared by nanomilling. Heating curves were obtained at 10 K/min. Pure LiNc-BuO crystals (black curve) showed exothermic decomposition peak, which almost disappeared after grinding (red and blue curves).

Stability of the linear oxygen response of pure LiNc-BuO crystals and MPs on storage

(a) Unencapsulated LiNc-BuO crystals (batch 1).

(b) MPs with entrapped spin probe.
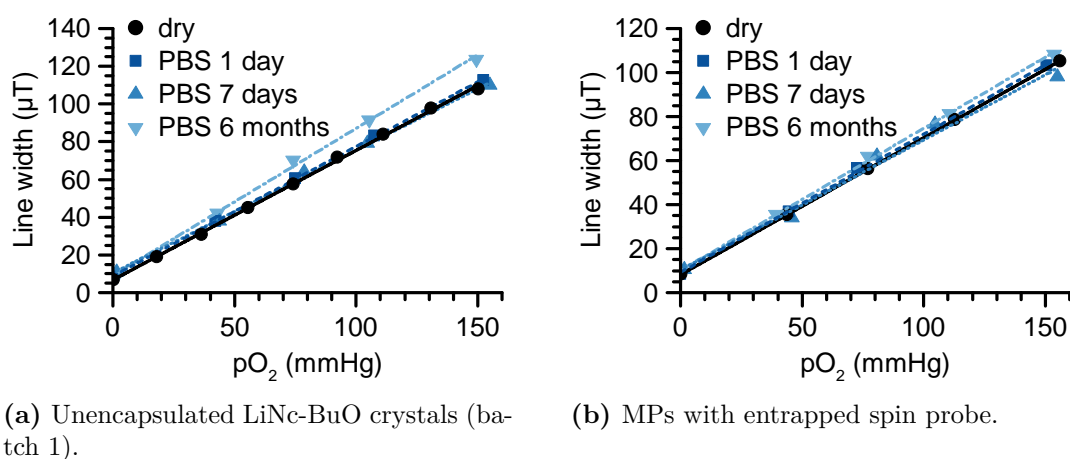
Figure A.8: Stability testing: Oxygen calibration curves were measured up to six months of storage in PBS 7.4 in the fridge (lines: linear regressions).

B Zusammenfassung

Sauerstoff ist im Körper an einer Vielzahl physiologischer und pathologischer Vorgänge beteiligt. Um die zugrundeliegenden Mechanismen zu verstehen, ist eine zuverlässige Bestimmung des Sauerstoffgehaltes in Geweben von außerordentlicher Bedeutung. Trotz großer Bemühungen konnte noch keine Sauerstoffmesstechnik entwickelt werden, die alle Bedürfnisse zufriedenstellend erfüllt. Die Paramagnetische Elektronenresonanz (EPR) Spektrometrie ist zu einer unverzichtbaren Methode geworden, da sie nichtinvasive und genaue Messungen von absoluten Sauerstoffgehalten in Echtzeit ermöglicht. Sauerstoff ist zwar ein Diradikal, kann aber nicht direkt, sondern nur durch Interaktion mit sauerstoffsensitiven Spinsonden nachgewiesen und quantifiziert werden. Dabei werden die EPR Linien dieser Radikale verbreitert. Die unvermeidbare Notwendigkeit des Einsatzes dieser stabilen Radikale ist verbunden mit der Sorge um deren ausreichende Biokompatibilität und Stabilität in Geweben. Außerdem ist die Synthese der Spinsonden oft sehr anspruchsvoll. Eine hohe Qualität ihrer physikochemischen und sauerstoffsensitiven Eigenschaften ist jedoch entscheidend für verlässliche Sauerstoffmessungen. Ziel dieser Arbeit war die nichtinvasive Sauerstoffmessung in Geweben anhand zweier präklinischer Tumormodelle. Dafür wurden zwei grundverschiedene Radikaltypen umfassend charakterisiert, um deren Anwendbarkeit als *in vivo* Sauerstoffsensoren zu evaluieren. Für die aussichtsreichsten Kandidaten wurden Formulierungen entwickelt, die die Biokompatibilität der Radikale verbesserten und gleichzeitig deren sauerstoffsensitives Verhalten bewahrten.

Im ersten Teil dieser Arbeit wurden lösliche Triarylmethyl- (Trityl-) Radikale untersucht, die von Kooperationspartnern hergestellt und bereits analytisch charakterisiert worden waren. Um deren Anwendbarkeit als Sauerstoffsensoren beurteilen zu können, wurden die Sensitivität, Linearität und die Spezifität der Sauerstoffmessungen untersucht. Die EPR Eigenschaften der hydrophilen Trityl-Radikale wurden in wässrigen Lösungen untersucht. Dabei zeigten die EPR Spektren dieser Radikale eine herausragend schmale Linie. Da diese Radikale ohne weitere Formulierung direkt in wässriger Lösung verwendet werden können, war eine hohe Spezifität der Linienbreitenänderungen für Sauerstoff essentiell. Es konnte innerhalb der physiologischen Bereiche der Osmolarität, Viskosität und des pH Wertes kein bedeutsamer Einfluss auf die Linienbreite festgestellt werden. Die Linenbreite nahm linear mit dem Sauerstoffgehalt zu. Es konnte also gezeigt werden,

dass hydrophile Tritylradikale nützliche EPR Sauerstoffsensoren sind. Allerdings steigt die Menge an gelöstem Sauerstoff in wässrigen Lösungen nur geringfügig mit dem Sauerstoffpartialdruck. Die Genauigkeit und Erfassbarkeit kleiner Differenzen im Sauerstoffgehalt war damit als gering zu bewerten.

Da die Sauerstofflöslichkeit in Ölen größer ist, wurden desweiteren Lösungen verschiedener lipophiler Trityl-Triester in Mittelkettigen Triglyceriden (MCT) und Isopropylmyristat (IPM) untersucht. Die Spektren nicht-deuterierter Triethylester waren durch eine Hyperfeinaufspaltung in deoxygenierten Lösungen gekennzeichnet. Andere Triester zeigten nur eine Linie, deren Breite direkt proportional zum Sauerstoffgehalt war, was für Sauerstoffmessungen gegenüber den hyperfeinaufgespalteten Spektren zu bevorzugen ist. Der volldeuterierte Triethylester dTAM-dEE war dabei nicht nur synthetisch gut zugänglich, sondern zeigte auch erfolgversprechende EPR Eigenschaften. Die EPR Linie in deoxygenierten Lösungen war schmal und die Sauerstoffsensitivität sehr hoch, besonders in IPM. Diese war deutlich höher als mit hydrophilen Spinsonden jemals erreicht werden kann. Ein vielversprechender Ansatz war daher die Verkapselung von dTAM-dEE in Nanokapseln (NK) mit MCT/IPM-Kern und Polyvinylacetat- (PVAc-) Hülle. Die NK-Herstellmethode, die in dieser Arbeit entwickelt wurde, erlaubte eine reproduzierbare Herstellung von NK mit geeigneten Partikel- und EPR-Eigenschaften. Die Sauerstoffempfindlichkeit des verkapselten Radikals blieb dabei erhalten. Mit IPM konnten NK mit sehr hoher Sauerstoffsensitivität erzielt werden, die sich besonders für die Erfassung kleiner Sauerstoffgehalte eignen. Stabile NK für Langzeitmessungen konnten mit MCT hergestellt werden. Durch die Verkapselung können sowohl die mögliche Toxizität der Radikale maskiert, als auch deren Anfälligkeit gegenüber biologischen Oxidoreduktasen verringert werden. Dies wurde exemplarisch anhand eines Ascorbinsäure-Reduktionsassays gezeigt: dTAM-dEE war vermutlich lipophil genug um in der NK zu verbleiben, wo die Polymerhülle nachweislich Schutz vor reduktiven Angriffen bot. Die Nanoverkapselung lipophiler Tritylradikale eignete sich also hervorragend, um stabile Nanosensoren mit hoher Sauerstoffsensitivität und Spezifität zu erhalten, die sich besonders für die Anwendung in komplexen biologischen Systemen eignen. Leider war durch die schwache EPR Signalintensität, die durch die geringe Menge an verkapselter Spinsonde gegeben ist, deren Anwendbarkeit *in vivo* nur eingeschränkt möglich.

Als Alternative dazu wurde im zweiten Teil dieser Arbeit die partikuläre Spinsonde Lithium-octa-*n*-butoxynaphthalocyanin (LiNc-BuO) gestet. Die Synthese von LiNc-BuO ist sehr komplex und reproduzierbare Eigenschaften der Partikel bzw. Kristalle sind nur schwer zu erreichen. Zunächst war folglich eine umfassende analytische Charakterisierung vonnöten, um sich von der Identität und Reinheit des bezogenen Radikals zu überzeugen. Verschiedene analytische Methoden zeigten, dass das Material zwar nicht frei von

Verunreinigungen war, sich aber dennoch sehr gut für Sauerstoffmessungen eignete. Die Verunreinigungen waren nur in gerningen Mengen enthalten und hatten keinen negativen Einfluss auf das EPR Spektrum oder die Sauerstoffempfindlichkeit. Durch Nanopräzipitation der reinen Spinsonde konnten nur polydisperse Nanopartikel (NP) hergestellt werden, was durch gleichzeitige Präzipitation und Coating mit PVAc erfolgreich verbessert werden konnte: Die erhaltenen Partikel waren monodispers und die Partikeleigenschaften sehr gut reproduzierbar. Die Signalstärke war höher als bei den Tritylradikal-haltigen NK. Es war allerdings fraglich, ob diese für *in vivo* Messungen genügen würde. Außerdem zeigte das EPR Spektrum meist eine Überlagerung zweier Spezies, was eine Auswertung der Daten erschwert hätte. Wahrscheinlich wurde dies verursacht durch eine Instabilität von LiNc-BuO in wässrigen Medien oder durch eine Störung des (Re-) Kristallisationsvorganges bzw. der Zugänglichkeit der Oberflächen und Kanäle für Sauerstoff und andere Gase.

Um den komplexen Kristallisationsschritt zu umgehen und wässrige Medien zu meiden, wurde eine nicht-wässrige Methode zur Herstellung LiNc-BuO-haltiger PVAc-Mikropartikel (MP) entwickelt. Durch die Nicht-Abbaubarkeit des Polymers und die Herstellmethode, die sicherstellte, dass keine unverkapselte Spinsonde mehr vorlag, konnte ein Kontakt des Radikals mit dem Gewebe ausgeschlossen werden. Die Stabilität der verkapselten Spinsonde in wässriger Dispersion konnte verbessert werden. Diese mikropartikulären Sensoren zeigten eine hervorragende Sauerstoffempfindlichkeit, die zwar etwas verringert war gegenüber des reinen Materials, aber immernoch sehr hoch, linear und reproduzierbar. Das Ansprechen auf eine Änderung des Sauerstoffgehaltes war ausreichend schnell und reversibel, wodurch gezeigt werden konnte, dass die Sauerstoffempfindlichkeit durch das Einbetten nicht negativ beeinflusst wurde, z.B. durch eine Anreicherung von Sauerstoff im Polymer. LiNc-BuO hat eine hohe Spindichte und es gibt keinen Linienverbreiterungseffekt bei hohen Konzentrationen, wodurch mit den MP auch *in vivo* eine ausreichende Signalstärke erreicht werden konnte. Auch sechs Monate nach Implantation war die Sauerstoffsensitivität *in vivo* noch unverändert gegeben, was durch eine *ex vivo* Kalibrierung gezeigt werden konnte. Die MPs verblieben an der Injektionsstelle ohne zu migrieren, was nicht nur lokalisierte, sondern auch wiederholte Messungen an derselben Stelle ermöglichte. Durch gleichzeitige Injektion mit einer Tumorzellsuspension wurden die MPs nichtinvasiv appliziert, sodass eine zusätzliche Verletzung des Gewebes verhindert werden konnte. Die Sauerstoffgehalte zweier Tumormodelle unter Normoxie, Hypoxie und Hyperoxie konnten reproduzierbar erfasst werden. Ein Vergleich mit fluorometrischen Messungen bzw. der Anreicherung des Hypoxiemarkers Pimonidazol bestätigte, dass die EPR Messungen zuverlässige und genaue Ergebnisse lieferten. Die MP waren im Gegensatz zur reinen Spinsonde sehr gut redispergier- und injizierbar. Hierdurch wurde erreicht, dass die MP als individuelle Partikel über den gesamten Tumor verteilt waren. Dies war sehr wichtig,

da der Sauerstoffgehalt besonders in Tumoren sehr heterogen verteilt ist. Es konnte weder eine Toxizität der MP noch ein Einfluss auf die Tumorphysiologie festgestellt werden. Falls erforderlich, können die MP mit Elektronenstrahlen sterilisiert werden. Es konnte kein bedeutender Einfluss auf die Partikeleigenschaften oder die Sauerstoffsensitivität der MP festgestellt werden.

Drei Formulierungen, die in in dieser Arbeit untersucht wurden (hydrophile Trityl-Radikale in wässriger Lösung, lipophile Trityl-Triester gelöst im Ölkern von NK, LiNc-BuO-haltige MP), waren sehr gut geeignet für *in vitro* Anwendungen als Sauerstoffsensoren und können je nach Anwendungsgebiet ausgewählt werden. Für die präklinische Forschung eignen sich besonders die leicht injizierbaren MP. Diese ermöglichen *in vivo* Messungen in Echtzeit sowie wiederholte Messungen in Langzeitstudien und könnten sogar nützlich sein für räumliche EPR Bildgebungsverfahren. Durch die MPs kann die nichtinvasive Erfassung von Sauerstoffgehalten in Geweben *in vivo* vorangebracht werden, sodass letztlich die Behandlung zahlreicher Erkrankungen angepasst werden und der Weg hin zu einer individualisierten Therapie geebnet werden kann.

C Acknowledgements

Working on this research project has been a great time for me. I really learned a lot – not only on the scientific, but also on a personal level. It is my pleasure to express my appreciation for the numerous people who supported me.

First of all, I would like to thank my supervisor Prof. Dr. Karsten Mäder for letting me join his group. Working on my project was, most of the time, according to the saying "*Find something you love to do and you'll never have to work a day in your life.*" Thank you for your trust and allowing this research to be my own work, while always having an open door for providing encouragement, guidance, and support.

I would like to thank my academic colleagues for their support. Particularly, Dr. Hendrik Metz is acknowledged for his invaluable advices. His different way to think about things often opened my eyes. Advice and personal support given by Dr. Sabine Kempe has been a great help getting my work started. I would like to thank Dr. Henrike Lucas for her pertinent support with all issues concerning animals and cells.

My grateful thanks are also extended to many collaboration partners for their fruitful participation and input, making our cooperation successful as it was. A warm thank goes to Prof. Dr. Peter Imming for all the stimulating discussions and his insightful comments. I am also deeply grateful to Dr. Simon Drescher. Thank you for your continuous support and obliging helpfulness, in particular, with the oxygen calibration measurements, and for diligently proofreading my Thesis and our research papers. You have been a great guy to work with. I am indebted to Dr. Marwa Elewa for providing several well characterized TAM radicals and for realizing our derivatization requests. I would also like to express my gratitude to Prof. Dr. Oliver Thews for giving me the opportunity to apply my MPs *in vivo* in two rat tumor models, which had been well established in his group, for letting me use his facilities, and for his valuable comments. I wish to thank Daniel Gündel for the inenarrable time with him and the rats, ranging from unlimited happiness to severe tenseness. I remember the sleepless nights we were working together, always in search for coffee and food. We had a great time.

I further acknowledge the contribution of Dr. Annette Meister and Dr. Gerd Hause in the TEM measurements, Prof. Dr. Stefan Ebbinghaus and Dr. Manfred Dubiel for letting me use their x-ray diffractometer and UV/Vis/NIR spectrometer, respectively, and their

helpful instructions, as well as Dr. Christian Ihling for MS measurements, the group of Dr. Dieter Ströhl for NMR analysis, and Heike Rudolf for IR measurements. I wish to thank Dr. Frank Erdmann for his willing help with cytotoxicity tests, Dr. Simon Geißler for nanomilling, Anne-Kathrin Heinrich for the beautiful fluorescence microscopy images, and Christin Zlomke for her obliging help and support with sterilization of the MPs and the GPC measurements.

Thanks are also due to Kerstin Schwarz and Ute Mentzel for their technical assistance and help organizing practical courses, and to Dieter Reese and his team for always carrying out my manufacturing and repairing orders immediately, so I could continue my experiments. I would like to acknowledge Dr. Bernhard Hiebl, Martina Hennicke, and their colleagues for their help ensuring welfare of my laboratory animals, and Claudia Bertram for her administrative support. The Deutsche Forschungsgemeinschaft is acknowledged for financial support (MA 1648/8).

Special thanks are due to my students Sebastian Beck (Diploma), Romanie Declerck (Master) from Belgium, as well as Luana Margotto and Mariana Albanez Campos (Practical trainees) from Brazil. Thank you for your passionate contribution and for the terrific time we had together during and especially after work.

I am also grateful to all my fellow doctoral students in Pharmaceutical technology. Thank you for welcoming me so friendly and giving me a good start in Halle, and for the nice time we had during lunchtime, after work, and at our class trips. I want to thank Dr. Stefan Hoffmann for helping me arrive in the group and get started, especially with teaching students, as well as for the great team work in the practical courses. I am thankful to Christin Zlomke und Martha Heider for the fun times and cozy get-togethers. Speaking of which, I particularly wish to thank Frederike Tenambergen and Anne-Kathrin Heinrich for the marvelous time we had as officemates, for their enduring helpfulness, their scientific input, and for becoming my very good friends. Freddy, thank you for giving me such a warm welcome in Halle. Anne, I am particularly thankful for the innumerable talks we had, ensuring my emotional well-being, but also for understanding me without words, for making the practical courses more bearable, and for teaching me how to handle mice as if they were my own babies.

No words can express how much I thank my amazing friends for their patience with me and my beloved family. Most of all, I want to thank my parents Simone and Uwe and my sister Anni, for their love and endless belief in me, and for their emotional support, as well as my husband for his love and enduring encouragement. Christian, thank you for standing by me – I owe it all to you.

D About the author

Curriculum vitae

Personal details

Name	Juliane Neidel geb. Frank
Date of birth	01/23/1987
Place of birth	Berlin, Germany

Education

05/2012-10/2017	**Research and teaching assistant (Doctoral student)**
	Martin-Luther-Universität Halle-Wittenberg
	Halle (Saale), Germany
	Group: Prof. Dr. Karsten Mäder (Pharmaceutical technology)
02/2012	Licensure as a pharmacist (Approbation)
10/2006-10/2010	**Pharmacy student**
	Freie Universität, Berlin, Germany
	01/2012 Third State Examination
	10/2010 Second State Examination
	08/2008 First State Examination
06/2006	**German Abitur**
	Barnim-Oberschule (Gymnasium), Berlin, Germany

Work experience

02/2012 - 05/2015	**Pharmacist**
	Rheinstein-Apotheke, Berlin, Germany
05/2011 - 10/2011	**Pharmacist in training**
	Rheinstein-Apotheke, Berlin, Germany
11/2010 - 04/2011	**Pharmacist in training**
	Berlin-Chemie AG, Berlin, Germany
	Group: Quality control, Galenical development, Research and development
08/2009 - 09/2009	**Practical training**
	Leibniz-Forschungsinstitut für Molekulare Pharmakologie/FMP Berlin-Buch, Germany
	Group: Mass spectrometry, Chemical Biology
01/2008 - 01/2012	**Student assistant**
	Reichenberger Apotheke, Berlin, Germany
08/2007 - 10/2010	**Student assistant**
	Konrad-Adenauer-Stiftung e.V., Berlin, Germany
08/2007	**Practical training (Famulatur)**
	Hospital pharmacy, HELIOS Klinikum, Berlin-Buch, Germany
03/2007	**Practical training (Famulatur)**
	Reichenberger Apotheke, Berlin, Germany

Awards

2013	Young Scientist Scholarship
	41st Annual ISOTT Meeting/EPR Conference, Hanover, USA

Hildesheim,

Juliane Neidel

Publications

Research articles

[1] M. Elewa, N. Maltar-Strmecki, M. M. Said, H. A. El Shihawy, M. El-Sadek, J. Frank, S. Drescher, M. Drescher, K. Mäder, D. Hinderberger, and P. Imming, "Synthesis and EPR-spectroscopic characterization of the perchlorotriarylmethyl tricarboxylic acid radical (PTMTC) and its 13C labelled analogue (13C-PTMTC)", *Phys. Chem. Chem. Phys.*, vol. 19, no. 9, pp. 6688–6697, 2017. DOI: `10.1039/C6CP07200C`.

[2] J. Frank, M. Elewa, M. M. Said, H. A. El Shihawy, M. El-Sadek, D. Müller, A. Meister, G. Hause, S. Drescher, H. Metz, P. Imming, and K. Mäder, "Synthesis, characterization, and nanoencapsulation of tetrathiatriarylmethyl and tetrachlorotriarylmethyl (trityl) radical derivatives - A study to advance their applicability as in vivo EPR oxygen sensors", *J. Org. Chem.*, vol. 80, no. 13, pp. 6754–6766, 2015. DOI: `10.1021/acs.joc.5b00918`.

[3] J. Frank, D. Gündel, S. Drescher, O. Thews, and K. Mäder, "Injectable LiNc-BuO loaded microspheres as in vivo EPR oxygen sensors after co-implantation with tumor cells", *Free Radic. Biol. Med.*, vol. 89, pp. 741–749, 2015. DOI: `10.1016/j.freeradbiomed.2015.10.401`.

Talks

[4] M. von Gröning, J. Frank, D. Gündel, S. Drescher, O. Thews, and K. Mäder, "Injectable LiNc-BuO Microparticles for in Vivo EPR Oximetry", in *Int. Conf. Electron Paramagn. Reson. Spectrosc. Imaging Biol. Syst.*, Morgantown, USA, 2017.

Posters and abstracts

[5] J. Frank, D. Gündel, O. Thews, and K. Mäder, "Injectable microspheres for non-invasive in vivo oximetry using electron paramagnetic resonance (EPR)", in *42nd Annu. Meet. Expo. Control. Release Soc.*, Edinburgh, Scotland, 2015.

[6] M. Elewa, J. Frank, K. Mäder, S. Drescher, and P. Imming, "Triarylmethyl radicals: Synthesis, EPR characterization and pharmaceutical applications", in *DPhG Jahrestagung*, Frankfurt, Germany, 2014.

[7] J. Frank, M. Elewa, S. Drescher, M. Albanez Campos, P. Imming, and K. Mäder, "Poly(vinyl acetate) nanocapsules as a carrier for lipophilic oxygen-sensitive EPR spin probes", in *9th World Meet. Pharm. Biopharm. Pharm. Technol.*, Lissabon, Portugal, 2014.

[8] M. Elewa, J. Frank, S. Drescher, H. Metz, K. Mäder, and P. Imming, "Synthesis and EPR measurements of the perchlorotriphenylmethyltricarboxylic acid radical (PTMTC) and its 13C labelled analogue (13C-PTMTC)", in *DPhG Jahrestagung*, Freiburg, Germany, 2013.

[9] J. Frank, S. Kempe, and K. Mäder, "Microacidity and release studies on thermally-induced chitosan-based gelling systems by EPR spectroscopy", in *41st Annu. ISOTT Meet. EPR 2013 Conf.*, Hanover, USA, 2013.

[10] M. Elewa, D. Müller, J. Frank, S. Kempe, S. Drescher, M. El-Sadek, M. Mokhtar, H. E. A. Elhamed, K. Mäder, and P. Imming, "Synthesis and EPR measurement of perchlorotriphenylmethyl radicals and their conjugates with biopolymers", in *3rd Int. Conf. Fac. Pharm. 15th Sci. Congr. Assoc. Pharm. Coll. Arab world*, Amman, Jordan, 2012.

E Declaration under Oath

Eidesstattliche Erklärung

(gemäß § 5 der Promotionsordnung der Naturwissenschaftlichen Fakultäten I, II, III
und des Zentrums für Ingenieurwissenschaften
der Martin-Luther-Universität Halle-Wittenberg)

Ich erkläre an Eides statt, dass ich die Arbeit selbstständig und ohne fremde Hilfe verfasst, keine anderen als die von mir angegebenen Quellen und Hilfsmittel benutzt und die den benutzten Werken wörtlich oder inhaltlich entnommenen Stellen als solche kenntlich gemacht habe.

Ich versichere außerdem, dass ich noch keine vergeblichen Promotionsversuche unternommen habe und dass die vorliegende Dissertation bisher weder in der gegenwärtigen noch in einer anderen Fassung einer anderen Fakultät vorgelegen hat.

Hildesheim,

Juliane Neidel